Universitat
de les Illes Balears

WWU
MÜNSTER

DOCTORAL THESIS
2022

DYNAMICS AND BIFURCATION ANALYSIS OF MODE-LOCKING IN COUPLED OPTICAL MICRO-CAVITIES

Denis Hessel

WWU
MÜNSTER

Universitat
de les Illes Balears

DOCTORAL THESIS
2022

Doctoral Programme in Physics

DYNAMICS AND BIFURCATION ANALYSIS OF MODE-LOCKING IN COUPLED OPTICAL MICRO-CAVITIES

Denis Hessel

Thesis Supervisor: Julien J. P. Javaloyes
Thesis Supervisor: Svetlana V. Gurevich
Thesis tutor: María R. L. Gonzalo

Doctor by the Universitat de les Illes Balears

Theoretische Physik

Dynamics and Bifurcation Analysis of Mode-Locking in Coupled Optical Micro-Cavities

Inaugural-Dissertation
zur Erlangung des Doktorgrades
der Naturwissenschaften im Fachbereich Physik
der Mathematisch-Naturwissenschaftlichen Fakultät
der Westfälischen Wilhelms-Universität Münster

angefertigt im Rahmen eines Cotutelle-Verfahrens
zwischen der Westfälischen Wilhelms-Universität Münster
und der Universitat de les Illes Balears

vorgelegt von
Denis Hessel
aus Mönchengladbach

2022

Be like the tortoise;
walk your path slow and steady.

ABSTRACT

The aim of this thesis is to understand passive mode-locking in coupled optical micro-cavities.

Delayed algebraic differential equations (DADEs) are derived from first principles for the dynamics of a mode-locked integrated external-cavity surface-emitting laser (MIXSEL) and a vertical cavity surface-emitting laser coupled to a saturable absorber mirror (VCSEL-RSAM).

By the example of the MIXSEL it is shown that third order dispersion induces a train of decaying satellites on the leading edge of a pulse. As a consequence of the nonlinear interaction with the carriers, these satellites may get amplified and destabilize the mode-locked state.

Depending on the parameters this instability stems either from a global bifurcation of the saddle-node infinite-period type or locally from an Andronov-Hopf bifurcation.

Multi-scale analysis and functional mapping are used to derive a master equation for both the MIXSEL and the VCSEL-RSAM, where for both equations third order dispersion is an essential ingredient.

The analysis of the MIXSEL is concluded by comparing the bifurcation diagrams for the master equation and the DADE yielding a good agreement.

For the VCSEL-RSAM the emergence of wiggling temporal localized states is investigated. The analysis shows that the wiggling instability is due to an interplay between the third order dispersion induced by the micro-cavities and their frequency mismatch. The frequency mismatch defines the range of existence of stable emission.

The bifurcation scenario underlying the wiggling phenomenon is revealed as stemming from a Bogdanov-Takens bifurcation. The existence of a homoclinic bifurcation allows controlling the period of the oscillation.

Further, a mechanism for the stabilization of a super mode-locked state was discovered that is due to second order dispersion induced by the frequency mismatch of the micro-cavities. The master equation successfully predicts the existence of all involved dynamical regimes, including a regime of bistable chaos.

In conclusion, this thesis discovered and explained three mechanism related to the stability of mode-locked states. It is the first time that master equations were derived and a bifurcation analysis was performed for DADE laser systems.

ZUSAMMENFASSUNG

Das Ziel dieser Arbeit ist es, die passive Modenkopplung in gekoppelten optischen Mikrokavitäten zu verstehen. Aus ersten Prinzipien werden verzögerte algebraische Differentialgleichungen (DADEs) abgeleitet für die Dynamik eines modengekoppelten integrierten oberflächenemittierenden Lasers mit externem Resonator (MIXSEL) und eines oberflächenemittierenden Lasers mit vertikalem Resonator gekoppelt an einen sättigbaren Absorberspiegel (VCSEL-RSAM).

Am Beispiel des MIXSEL wird gezeigt, dass die Dispersion dritter Ordnung einen Zug von abklingenden Satelliten an der Vorderflanke eines Pulses induziert. Als Folge der nichtlinearen Wechselwirkung mit den Ladungsträgern können diese Satelliten verstärkt werden und den modengekoppelten Zustand destabilisieren.

Abhängig von den Parametern entstammt diese Instabilität entweder von einer globalen Bifurkation des Saddle-Node-Typs mit unendlicher Periode oder lokal von einer Andronov-Hopf-Bifurkation.

Mit Hilfe der Multiskalenanalyse und der funktionalen Abbildung wird eine Master-Gleichung sowohl für den MIXSEL als auch für den VCSEL-RSAM abgeleitet, wobei für beide Gleichungen die Dispersion dritter Ordnung ein wesentlicher Bestandteil ist.

Die Analyse des MIXSEL wird durch den Vergleich der Bifurkationsdiagramme für die Master-Gleichung und die DADE abgeschlossen, wobei eine gute Übereinstimmung festgestellt wird.

Für den VCSEL-RSAM wird das Auftreten von wackelnden zeitlich lokalisierten Zuständen untersucht. Die Analyse zeigt, dass die Wackel-Instabilität auf ein Zusammenspiel zwischen der durch die Mikrokavitäten induzierten Dispersion dritter Ordnung und deren Frequenzabweichung zurückzuführen ist. Es zeigt sich, dass die Frequenzabweichung den Bereich der stabilen Emission festlegt.

Das Wackelphänomen ist auf eine Bogdanov-Takens-Bifurkation zurückzuführen. Eine existierende homoklinen Bifurkation ermöglicht es, die Periode der Oszillation zu kontrollieren.

Darüber hinaus wurde ein Mechanismus zur Stabilisierung eines super modengekoppelten Zustands entdeckt, der auf die Dispersion zweiter Ordnung zurückzuführen ist, die durch die Frequenzabweichung der Mikrokavitäten entsteht. Die Master-Gleichung sagt erfolgreich die Existenz aller beteiligten dynamischen Regime voraus, einschließlich eines Regimes von bistabilem Chaos.

Zusammenfassend wurden in dieser Arbeit drei Mechanismen im Zusammenhang mit der Stabilität von modengekoppelten Zuständen entdeckt und erklärt. Zum ersten Mal wurden für DADE Lasersysteme Master-Gleichungen hergeleitet und eine Bifurkationsanalyse durchgeführt.

RESUMEN

El objetivo de esta tesis es comprender el bloqueo de modo pasivo en microcavidades ópticas acopladas. Por eso, se derivan ecuaciones diferenciales algebraicas retardadas (DADE) a partir de los primeros principios para la dinámica de un láser emisor de superficie de cavidad externa integrado con bloqueo de modo (MIXSEL) y un láser emisor de superficie de cavidad vertical acoplado a un espejo absorbente saturable (VCSEL-RSAM).

Con el ejemplo del MIXSEL se demuestra que la dispersión de tercer orden induce un tren de satélites que decaen en el borde de ataque de los pulsos. Como consecuencia de la interacción no lineal con los portadores, estos satélites pueden amplificarse y desestabilizar el estado de bloqueo de modo.

Dependiendo de los parámetros, esta inestabilidad proviene de una bifurcación global del tipo nodo de silla con período infinito o también de una bifurcación local de Andronov-Hopf.

El análisis multiescala y el metodo del mapeo funcional se utilizan para derivar una ecuación maestra tanto para el MIXSEL como para el VCSEL-RSAM, donde para ambas ecuaciones la dispersión de tercer orden revela ser un ingrediente esencial.

El análisis del sistema MIXSEL se concluye comparando los diagramas de bifurcación de la ecuación maestra y del modelo DADE, destacando el buen acuerdo.

En el caso del VCSEL-RSAM se investiga la aparición de estados localizados temporales ondulantes. El análisis muestra que la inestabilidad del movimiento de los pulsos se debe a una interacción entre la dispersión de tercer orden inducida por las microcavidades y su desajuste de frecuencia. El desajuste de frecuencia define el rango de existencia de la emisión estable.

El escenario de bifurcación que subyace al fenómeno de ondulación se revela como derivado de una bifurcación de Bogdanov-Takens. La existencia de una bifurcación homoclínica permite controlar el período de oscilación.

Además, se identificó un mecanismo para la estabilización de un estado de súper bloqueado de modos que se debe a la dispersión de segundo orden inducida por el desajuste de frecuencia entre las microcavidades. La ecuación maestra predice con éxito la existencia de todos los regímenes dinámicos involucrados, incluido un régimen de caos biestable.

En conclusión, esta tesis descubrió y explicó tres mecanismos relacionados con la estabilidad de los estados de bloqueo de modo. Es la primera vez que se derivan ecuaciones maestras y se realiza un análisis de bifurcación para sistemas láser DADE.

RESUM

L'objectiu d'aquesta tesi és comprendre el bloqueig de modo passivo en microcavitats òptiques acoblades.

Per això, es deriven equacions diferencials algebraiques retardades (DADE) a partir dels primers principis per a la dinàmica d'un làser emissor de superfície de cavitat externa integrat amb bloqueig de mode (MIXSEL) i un làser emissor de superfície de cavitat vertical acoblat a un mirall absorbent saturable (VCSEL-RSAM).

Amb l'exemple del MIXSEL es demostra que la dispersió de tercer ordre indueix un tren de satèl·lits que decauen a la vora d'atac dels polsos. Com a conseqüència de la interacció no lineal amb els portadors, aquests satèl·lits es poden amplificar i desestabilitzar l'estat de bloqueig de manera.

Depenent dels paràmetres, aquesta inestabilitat prové duna bifurcació global del tipus node de cadira amb període infinit o també duna bifurcació local d'Andronov-Hopf.

L'anàlisi multiescala i el mètode de mapatge funcional s'utilitzen per derivar una equació mestra tant per al MIXSEL com per al VCSEL-RSAM, on per a totes dues equacions la dispersió de tercer ordre revela ser un ingredient essencial.

L'anàlisi del sistema MIXSEL es conclou comparant els diagrames de bifurcació de l'equació mestra i del model DADE, destacant el bon acord.

En el cas del VCSEL-RSAM, s'investiga l'aparició d'estats localitzats temporals ondulants. L'anàlisi mostra que la inestabilitat del moviment dels polsos es deu a una interacció entre la dispersió de tercer ordre induïda per les microcavitats i el desajust de freqüència. El desajust de freqüència defineix el rang d'existència de l'emissió estable.

L'escenari de bifurcació subjacent al fenomen d'ondulació es revela com a derivat d'una bifurcació de Bogdanov-Takens. L'existència d'una bifurcació homoclínica permet controlar el període d'oscil·lació.

A més, es va identificar un mecanisme per a l'estabilització d'un estat de súper bloquejat de modos que es deu a la dispersió de segon ordre induïda pel desajust de freqüència entre les microcavitats. L'equació mestra prediu amb èxit l'existència de tots els règims dinàmics involucrats, inclòs un règim de caos biestable.

En conclusió, aquesta tesi va descobrir i explicar tres mecanismes relacionats amb l'estabilitat dels estats de bloqueig de manera. És la primera vegada que es deriven equacions mestres i es fa una anàlisi de bifurcació per a sistemes làser DADE.

PUBLICATIONS

During the course of this PhD the following manuscripts and software contributions have been published or are currently in preparation:

[1] D. A. W. Barton, S. Terrien, D. Hessel, S. V. Gurevich and J. Javaloyes. *DDE-BIFTOOL – Methods and parts of implementation for neutral DDEs and demo*. URL: `https://sourceforge.net/projects/ddebiftool/`. 2019.

[2] C. Schelte, D. Hessel, J. Javaloyes and S. V. Gurevich. "Dispersive Instabilities in Passively Mode-Locked Integrated External-Cavity Surface-Emitting Lasers." In: *Physical Review Applied* 13 (2020), p. 054050.

[3] D. Hessel, S. V. Gurevich and J. Javaloyes. "Wiggling instabilities of temporal localized states in passively mode-locked vertical external-cavity surface-emitting lasers." In: *Optics Letters* 46 (2021), pp. 2557–2560.

[4] D. Hessel, S. V. Gurevich and J. Javaloyes. "Super mode-locking in passively mode-locked vertical external-cavity surface-emitting lasers." *(in preparation)*.

Parts of the text in the introduction and the summary have been published in [2–4]. All other citations are indicated in the sections in which they appear.

ACKNOWLEDGMENTS

My thanks go out to all who supported me and believed in me.

I express my deepest gratitude to my supervisors, Svetlana Gurevich and Julien Javaloyes, for their invaluable advice and guidance throughout my PhD studies. Your never-ending passion for advancing the edge of human knowledge inspires me, and your actions show that you care about your students. It was only possible to complete this PhD because of you.

I am further grateful to the members of the working group self-organization and complexity in Münster, as well as the working group nonlinear photonics in Palma, for many stimulating conversations and helpful suggestions.

Thanks to Christian Schelte for patiently answering all my questions, especially after moving to a different continent.

I appreciate the help of everyone who proofread this thesis: Svetlana Gurevich, Julien Javaloyes, Oliver Mai, Thomas Seidel and Moritz Stieneker.

Thank you to Laura Berkemeyer, Simon Hartmann, Oliver Mai and Thomas Seidel for working so many Pomodoro sessions with me and keeping me company.

I am grateful to Annika Boje and Thorge Breer for being kind enough to welcome me into their home for a retreat, where I wrote a part of this thesis.

Special thanks to Oliver Mai and Moritz Stieneker for their lasting friendship since the beginning of my undergraduate studies.

Finally, I thank Anna Hessel for her support, patience, and love.
My life would not be the same without you.

CONTENTS

LIST OF FIGURES

LIST OF TABLES

LISTINGS

LIST OF ABBREVIATIONS

CW	Continuous wave
DADE	Delayed algebraic differential equation
DAE	Delay algebraic equation
DBR	Distributed Bragg reflector
DDE	Delayed differential equation
DDS	Delayed dynamical system
DNS	Direct numerical simulation
FML	Fundamental mode-locked
GTI	Gires-Tournois interferometer
LASER	Light amplification by stimulated emission of radiation
LSA	Linear stability analysis
MIXSEL	Mode-locked integrated external surface-emitting laser
NDDE	Neutral delayed differential equation
ODE	Ordinary differential equation
PDE	Partial differential equation
PML	Passive mode-locking
QW	Quantum well
RSAM	Resonant saturable absorber mirror
SML	Super mode-locked
TLS	Temporal localized state
VCSEL	Vertical cavity surface-emitting laser

1

INTRODUCTION

The study of light and optical phenomena has a long and illustrious history, dating back to the time of the ancient Greeks [1]. At first, optics was the theory of vision. It was in the 17th century that light became the central entity of optics due to Kepler [2]. None of the theories of light that existed until the 20th century could satisfactory explain all the phenoma observed nowadays. Two theories about light were the most widespread: One theory considered light as a particle and was most notably advocated by Newton [3], while the other is a wave description of light, advocated by Huygens and Fresnel, among others [1]. The discovery of quantum mechanics revolutionized the understanding of optics and resolved the ambiguity about the dual nature of light [4–6].

In modern times, the study of light has taken on new importance with the advent of lasers in the second half of the 20th century [7, 8]. Long before that, in 1899, the foundation for these devices was laid by Fabry and Pérot, who came up with the idea of an interference apparatus consisting of two parallel reflecting mirrors, i. e., an optical cavity [9].

In 1917, Einstein postulated stimulated emission, which explained the observed spectrum of black-body radiation [4]. Before, classical electromagnetism could only explain the processes of absorption and spontaneous emission. Twenty years after Einsteins prediction, Fabrikant came up with the idea to apply the effect of stimulated emission to amplify radiation [10]. However, his efforts were delayed by the Second World War and it was only until 1954 that a laser was finally realized in an experiment by Townes [7].

It is difficult to overstate the relevance of laser applications, like optical fibre communications [11, 12], cutting materials [13], data processing [14], or in medicine [15–18] that are essential to many aspects of contemporary life. Applications of lasers further include mass-market consumer products like laser pointers, compact discs or laser printers.

Even if a laser's pumping is constant, its output might be irregular [19]. While the irregular output was initially explained to stem from noise and imperfections, it was later proposed that it may result from nonlinear interactions in the equations that govern the laser dynamics [20]. An intense and still ongoing study of dynamical systems ensued after Lorenz demonstrated in 1963 that deterministic chaos, i. e., complex dynamical behavior, exists in systems with merely three degrees of

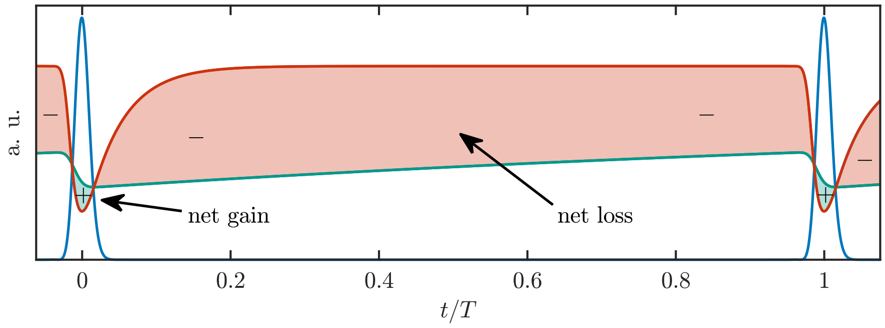

Figure 1.1: Illustration of passively mode-locked dynamics in a laser with a saturable absorber. Blue, green and red lines indicate the electrical field intensity, the gain and the absorber population inversion, respectively. The absorber evolves on a faster time scale than the gain, which leads to the opening of a net gain window (+) around the pulse and to net losses (−) elsewhere.

freedom [21]. In 1975, Haken demonstrated that the system studied by Lorenz to explain fluid dynamics is identical to a single mode laser [20].

In regular laser emission, the different modes, i. e., standing waves in the laser cavity, oscillate independently with no fixed phase relation. In this case, the output is roughly constant in intensity since the ever changing modal superposition does not create high amplitude fluctuations.

If the phase between the modes is fixed so that the modes interfere constructively, the laser's output is instead a train of intense and short (on the order of femtoseconds) pulses, which is called mode-locking [22–24]. The discovery of mode-locking [25] led to further important technological applications, e. g., an optical clock or in medical surgeries [26–29].

The shortest and most intense pulses have been achieved with passive mode-locking (PML). This approach combines a gain medium amplifying the light and a saturable absorber absorbing the light and shortening the pulse duration. Both the absorption and amplification of light decreases with increasing light intensity. Because the absorber evolves on a faster time scale than the gain medium, a net gain window opens around the pulse, while net losses prevail elsewhere [30, 31]. Figure 1.1 illustrates this principle.

Coupled optical micro-cavities, which confine light in small volumes and thereby increase the interaction with the medium, can emit PML light with high output power and good beam quality. Two such laser sources are investigated in this thesis: One is a mode-locked integrated external-cavity surface-emitting laser (MIXSEL) [36, 37] and the other one is a vertical-cavity surface-emitting laser coupled to a resonant saturable absorber mirror (VCSEL-RSAM) [38–46].

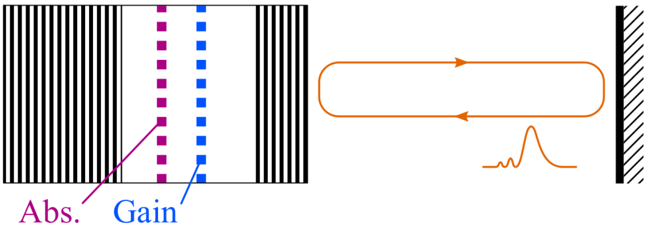

(a) MIXSEL

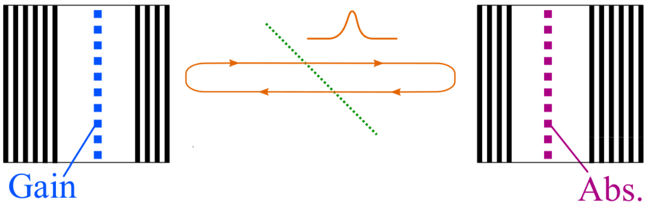

(b) VCSEL-RSAM

Figure 1.2: Schematics of the coupled micro-cavity setups investigated in this thesis. (a) A mode-locked integrated external-cavity surface-emitting laser (MIXSEL) where both a gain (blue) and a saturable absorber medium (purple) are enclosed in a micro-cavity coupled to an external feedback mirror. (b) A vertical cavity surface-emitting laser coupled to a resonant saturable absorber mirror (VCSEL-RSAM). The gain (blue) and saturable absorber medium (purple) are enclosed in two different micro-cavities with a beam splitter (green dotted line) in the middle. For both setups, the output of a micro-cavity is injected into a micro-cavity after passing some distance. Adapted with permission from [32–35].

Figure 1.2 (a,b) depicts the setups of both the MIXSEL and the VCSEL-RSAM, respectively. In a MIXSEL both the gain and the saturable absorber share the same micro-cavity coupled to an external feedback mirror. The VCSEL-RSAM consists of two micro-cavities, one containing the gain and the other containing the saturable absorber.

Despite intensive research efforts toward the general understanding of PML, its stability mechanisms are not fully understood yet due to the complexity involved in the analysis of high dimensional, nonlinear equations leading to many kinds of dynamical regimes. In this thesis, the theory of dynamical systems sheds light on three of these stability mechanisms.

A particular class of dynamical system is known as delayed dynamical system. Delay arises naturally in the modeling process in many different fields whenever information takes a finite amount of time to propagate [47–51]. Combining so-called delayed differential equations with algebraic constraints [52–55], the resulting equations are called delayed algebraic differential equations (DADEs) [56–64]. Delayed dynamical systems have strong links with spatially extended systems such as the Ginzburg-Landau equation [65, 66] and, as mentioned, can lead to a variety of dynamical behaviors [67–72].

When coupled micro-cavities are modeled from first principles, the governing equation is a DADE as the electrical field injected into one micro-cavity equals the output of a micro-cavity at a past time. While modeling coupled micro-cavities as DADEs is elegant and intuitive, it complicates the analysis. Although DADE models for coupled micro-cavities were proposed as early as 2005 [73], they have not been widely used since due to the complexity of dealing with the algebraic conditions and time delay. However, this thesis presents instabilities of PML, which cannot be observed in models based on the more commonly used delayed differential equations because their dispersive effects are negligible [35]. One contribution of this thesis is the implementation of numerical methods which enable the bifurcation analysis of DADEs [74], which is a method revealing how a dynamical system behaves in the control parameter space.

Direct numerical simulation and bifurcation analysis only sometimes allow for an intuitive interpretation of the dynamics. Further, the physical interpretation of the dynamics might stay hidden in the structure of the time-delayed equations. Therefore, it is insightful to derive a partial differential equation (PDE) as a so-called normal form for the field amplitude that approximates the dynamics of the full DADE model. In the PDE representation, the field depends on a slow and a fast time. The slow time represents the evolution of the field profile from one round-trip to the next, while the fast time describes the evolution of the pulse within the round-trip. While this approach has been used in several time-delayed systems [71, 72], such PDE models are usually termed Haus master equations in the framework of mode-locking as the Haus equation, at first a semiphenomenological model, was originally derived to study active mode-locking [23].

The analysis of the MIXSEL and VCSEL-RSAM systems with direct numerical simulations, bifurcation analyses and normal forms reveals and explains three mechanisms related to the stability of PML pulses: the satellite instability, wiggling and super mode-locking.

The satellite instability was experimentally observed recently in the long cavity regime in a mode-locked VCSEL-RSAM [35]. At its core, this unstable pulsating regime results from the face-to-face coupling of the micro-cavities containing the gain and the saturable absorber media. Operated in reflection, the gain and absorber micro-cavities behave as dispersive Gires-Tournois interferometers (GTI) [75]. After several round-trips, the third order dispersion induced by the dispersive micro-cavities gives rise to serrated waveforms that consist of a decaying sequence of satellites accumulating in front of the leading edge of the pulse. It is shown that these satellites may become unstable, leading to low-frequency modulation of the pulse envelope on a slow time scale, typically on the order of hundreds of round-trips.

A wiggling mode-locked state is characterized by an amplitude and position oscillating in time. Wiggling behavior was observed in a wide range of setups including photovoltaic photorefractive crystals, wide-aperture lasers with a saturable absorber, chemical systems, and as a secondary instability of the cubic-quintic complex Ginzburg-Landau equation [76–88]. The analysis shows that the wiggling instability is due to an interplay between the third order dispersion induced by the micro-cavities and their frequency mismatch. Furthermore, the frequency mismatch defines the range of existence of stable emission.

In addition to the fundamental mode-locked (FML) solution depicted in figure 1.1 a super mode-locked (SML) solution is discovered in the VCSEL-RSAM. For low gain, the SML solution has satellites on the leading edge. For higher gain, the SML solution is similar to the fundamental mode-locked solution, although the power spectrum is broader than the FML solution and asymmetrical. The analysis reveals that the second order dispersion induced by the frequency mismatch of the micro-cavities may stabilize the SML state. The corresponding master equation successfully predicts the existence of all involved dynamical regimes, including a regime of bistable chaos.

OUTLINE Chapter 1 introduces the topic of this thesis. Chapter 2 details the theory necessary to understand the results in the main part. In particular, the models for the MIXSEL and the VCSEL-RSAM systems are derived from first principles. The main part of this thesis starts with chapter 3, which investigates the MIXSEL system. It is shown how the delay algebraic modeling leads to third order dispersion. This in turn might induce a satellite instability. The underlying principle is explained with the master equation derived from the system's equations. Chapter 4 explores the VCSEL-RSAM system. It is revealed how an interplay of the frequency mismatch between the two micro-cavities and third order dispersion results in a wiggling instability. Further, the master equation for the VCSEL-RSAM is derived, and it is shown how second order dispersion stabilizes a super mode-locked state. Chapter 5 concludes this thesis with a summary and an outlook on further research directions.

2

THEORY

2.1 DYNAMICAL SYSTEMS

A dynamical system describes how a given state evolves in time. Using a formal general definition [89, 90] a dynamical system is a tuple $(\mathbb{T}, X, \Phi)$ where $\mathbb{T}$ is the time domain, X is the state space and $\Phi : U \subseteq (\mathbb{T} \times X) \to X$ with $proj_2(U) = X$ is the evolution function ($proj_2$ denotes the second projection map [91]). Further, ϕ satisfies

$$\Phi(0, x) = x, \tag{2.1}$$

$$\Phi(t_1, \Phi(t_2, x)) = \Phi(t_1 + t_2, x). \tag{2.2}$$

Then the evolution of an initial state x is given by

$$\Phi_x(t) = \Phi(t, x), \tag{2.3}$$

where $\Phi_x(t)$ is called the flow through x. Often instead of $\Phi_x(t)$, the convention is to write $x(t)$.

The trajectory through x is defined as

$$\mathcal{P}_x = \{\Phi_x(t) | t \in T\} \tag{2.4}$$

and it is one of the goals of the theory of dynamical systems to make statements about the trajectories of a given dynamical system [90].

In general, the evolution of a dynamical system is either given by an iterative map with discrete time values $T = \mathbb{Z}$ relating the state at the next time value with the state at the current time value as

$$x_{i+1} = f(x_i) \tag{2.5}$$

with $x_i \in \mathbb{R}^d$, $f : \mathbb{R}^d \to \mathbb{R}^d$. The system (2.5) is then called a discrete dynamical system. Alternatively, the evolution is given as a differential equation with continuous time $T = \mathbb{R}$, where the derivative of the state at the current time is in some particular way related to the value of the state. In this case, the system is called a continuous dynamical system. The simplest form is given by an ordinary differential equation (ODE) that can be written as

$$\dot{x}(t) = f(x(t)) \tag{2.6}$$

with $x(t) \in \mathbb{R}^d$, $f : \mathbb{R}^d \to \mathbb{R}^d$. f is commonly called the right-hand side of the dynamical system.

Although f is not explicitly time-dependent, it might be implicitly by introducing another component $z = t$ with $\dot{z} = 1$ to the state vector x.

As many of the prevalent phenomena appearing in dynamical systems can already be explained using ODEs, the following two subsections are explained with ODEs summarizing from [89, 92]. Based on this, delayed dynamical systems are introduced, and their properties are discussed. Further, spatially extended systems given by partial differential equations are presented as they are closely linked to delayed dynamical systems in the long delay limit.

2.1.1 *Bifurcation Theory*

Normally, one would like to obtain an analytical expression for the time evolution of x, i. e., one would like to solve the map (2.5) or differential equation (2.6) analytically.

If f is linear, a complete theory for this case exists [93, 94] and it is possible to obtain an analytical solution. However, usually no such solution even exists when f is given by seemingly simple nonlinear expression. Therefore, a slightly weaker approach is used that aims to make statements about the structure of the solution space. The goal is to identify state space subsets that attract or repel close-by trajectories under the flow. Although repelling subsets cannot be observed directly in numerical simulations, they can still strongly influence the behavior of the dynamical system.

Simple and often studied examples are steady states, closed trajectory periodic orbits, and non-integer dimensional subsets that lead to chaos. Bifurcation theory then examines how these sets' existence and stability change as control parameters vary.

2.1.2 *Steady States*

Steady states are states that do not change in time. They can be determined from the ODE by solving

$$\dot{x}^* = f(x^*) = 0, \tag{2.7}$$

where x^* is the steady state. As the next section shows, steady states give insight into a dynamical system because they determine the behavior of close-by states.

2.1.3 *Linear Stability Analysis*

Close to a steady state, trajectories are usually either attracted towards the steady state or are repelled by it. If all trajectories in the vicinity of the steady state converge to it, the steady state is called stable. On the other hand, if there is at least one direction from which nearby trajectories diverge, the steady state is called unstable.

The stability of a steady state x^* can be determined by investigating the linear dynamics of the state

$$x = x^* + \delta x, \tag{2.8}$$

i. e., a state that is slightly perturbed from the steady state. If the perturbation δx decays to zero, the steady state is stable. The steady state is unstable if it grows exponentially in the linearized system. Between exponential decay and exponential growth, the perturbation can also stay constant in magnitude in a direction. If the steady state is not unstable and the magnitude of the perturbation stays constant in at least one direction, the steady state is called neutrally stable.

Inserting equation (2.8) into the ODE yields

$$\dot{x} = \dot{x^*} + \dot{\delta x} = f(x^* + \delta x). \tag{2.9}$$

Equation (2.9) is potentially still nonlinear. Linearizing the right-hand side around x^* gives

$$f(x^* + \delta x) \approx f(x^*) + J(x^*)\delta x, \tag{2.10}$$

where $J(x^*) = \left(\frac{df_i}{dx_j}(x^*)\right)_{ij}$ is the Jacobian matrix of f, i. e., the matrix of derivatives of f with regard to all components of x. Combining equations (2.9) and (2.10) together with $\dot{x}^* = 0$ and $f(x^*) = 0$ gives the equation for the linear dynamics of δx as

$$\dot{\delta x} = J(x^*)\delta x. \tag{2.11}$$

Such a linearized ODE can be solved analytically with the ansatz

$$\delta x(t) = ve^{\lambda t}. \tag{2.12}$$

Inserting equation (2.12) into equation (2.11) results in a linear eigenvalue problem

$$\lambda v = J(x^*)v \tag{2.13}$$

with eigenvalue λ and eigenvector v. According to elementary linear algebra [95] a nontrivial solution $v \neq 0$ exists, if and only if

$$\chi(\lambda) = |J(x^*) - \mathbb{1}\lambda| = 0. \tag{2.14}$$

Equation (2.14) is called the characteristic equation of the dynamical system with characteristic function χ. In a dynamical system where all the components of x are real-valued, eigenvalues come in complex conjugated pairs. Equation (2.14) has n (potentially degenerate) solutions for λ, i. e., one for each dimension of the dynamical system.

The stability of a steady state is determined by the eigenvalues of the Jacobi matrix of the dynamical system:

- If there is at least one λ with $\mathrm{Re}[\lambda] > 0$, a perturbation in the direction of the respective eigenvector diverges exponentially from the steady state. In this case, the steady state is unstable.
- If all eigenvalues λ have negative real part $\mathrm{Re}[\lambda] < 0$, all perturbations decay exponentially. Nearby trajectories converge to the steady state. In this case, the steady state is stable.
- If the largest real part of the eigenvalues is zero, the steady state is neutrally stable. In linear systems, the state does not move along the axes of eigenvectors belonging to eigenvalues with $\mathrm{Re}[\lambda] = 0$. In nonlinear systems, higher-order terms decide if the perturbation diverges from or converges to the steady state.

2.1.4 *Periodic Orbits*

Periodic orbits are trajectories of a dynamical system (2.5) that are closed, i. e., where the state at a certain time t repeats itself after the period T of the periodic orbit [96]. A state that is part of a periodic orbit fulfills the relationship

$$x(t) = x(t+T). \tag{2.15}$$

Let $\chi^n \in \mathcal{C}$ be a profile of length T defined by

$$\chi^n(t) = x(nT+t), \tag{2.16}$$

where $\mathcal{C} = C([0,T], \mathbb{R}^d)$ is the space of continuous real d-dimensional vector functions on the interval $[0,T]$.

From there, an iterative map can be defined for the dynamics of χ as

$$\chi^{n+1} = \mathcal{M}_T[\chi^n], \tag{2.17}$$

where $\mathcal{M}_T$ is called the monodromy operator defined by the integral over the right-hand side

$$\mathcal{M}_T[\chi^n](t) = x(nT+t) + \int\limits_0^T f(x(nT+t+t'))\,\mathrm{d}t'. \tag{2.18}$$

Periodic orbits χ^* are steady states of equation (2.17), i. e., they fulfill

$$\chi^* = \mathcal{M}_T[\chi^*]. \tag{2.19}$$

This formulation allows determining the stability of a periodic orbit in the same way as for any other iterative map: Linearizing the dynamics, making an exponential ansatz and determining the eigenvalues. For iterative maps, these eigenvalues are called Floquet multipliers.

Following section 2.1.3, the linear dynamics of the state

$$\chi^n = \chi^* + \delta\chi^n \tag{2.20}$$

close to a periodic orbit are determined, where $\delta\chi^n$ is the perturbation. Inserting equation (2.20) into equation (2.17) leads to

$$\chi^{n+1} = \chi^* + \delta\chi^{n+1} = \mathcal{M}_T[\chi^* + \delta\chi^n] \approx \mathcal{M}_T\chi^* + \mathcal{J}_T\delta\chi^n. \tag{2.21}$$

As $\mathcal{M}_T\chi^* = \chi^*$ the dynamics of the perturbation are given by

$$\delta\chi^{n+1} = \mathcal{J}_T\delta\chi^n, \tag{2.22}$$

where $\mathcal{J}_T$ is the Jacobian of $\mathcal{M}_T$.

The stability of the periodic orbit is determined by the Floquet multipliers μ of $\mathcal{J}_T$:

- If there exists at least one Flowuet multiplier with $|\mu| > 1$, then the perturbation grows exponentially in magnitude with every iteration. As a result, the periodic orbit is unstable.
- If for all Floquet multipliers $|\mu| < 1$ holds, then the perturbation decays exponentially in magnitude with every iteration. The periodic orbit is stable.
- If for the Floquet multiplier with the largest modulus $|\mu| = 1$ holds, then the perturbation stays constant in magnitude in the direction of the respective eigenprofile with every iteration in the linearized system. The periodic orbit is neutrally stable, and the nonlinearities determine whether perturbations grow or decay.

2.1.5 *Chaos*

Chaos is a special kind of dynamic that is deterministic, aperiodic and highly sensitive to initial conditions.

Deterministic means that the dynamics are not random but always result in the same output from a given initial condition. Two states that are identical to each other evolve the same over time. Although being sensitive to initial conditions implies that it is difficult to make predictions far into the future if the measurement of the current state has uncertainty, the deterministic nature of the dynamics makes it possible to make short-term predictions and to infer causality [97–99].

Further, chaotic dynamics are aperiodic, i. e., the state neither repeats itself nor converges to a steady state. However, quasi-periodic motion is not highly sensitive to initial conditions in contrast to chaos.

Finally, chaos is highly sensitive to initial conditions. Nearby initial conditions diverge exponentially, as measured by the Lyapunuov-exponent Λ [92]. In particular, two infinitesimal close initial conditions with separation $\delta x(t)$ diverge from each other with a rate given by

$$|\delta x(t)| \approx e^{\Lambda t}|\delta x(0)|. \tag{2.23}$$

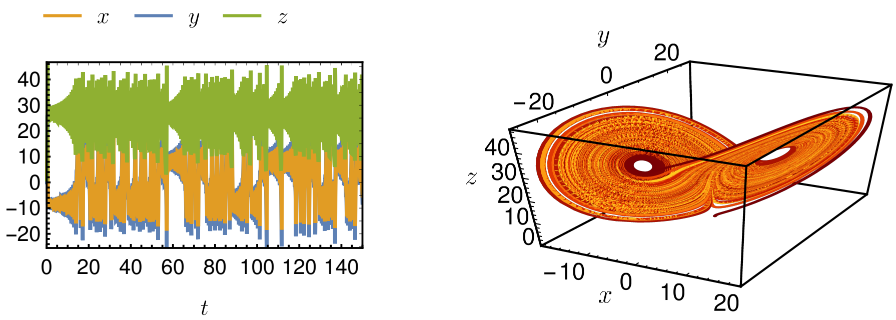

(a) Time traces

(b) State space representation

Figure 2.1: Evolution of the Lorenz system (2.24)-(2.26). The dynamics at the parameter values $(\rho, \beta, \sigma) = (28, 8/3, 10)$ are an example of chaotic behaviour. While the time traces (a) seem unpredictable, the state space representation (b) shows the dynamics' inherent structure.

One famous example of a dynamical system exhibiting chaos is the Lorenz system [21] that is given by

$$\dot{x} = \sigma(y - x), \tag{2.24}$$

$$\dot{y} = x(\rho - z) - y, \tag{2.25}$$

$$\dot{z} = xy - \beta z. \tag{2.26}$$

For the parameter values $(\rho, \beta, \sigma) = (28, 8/3, 10)$ a chaotic attractor is globally stable. A time trace for this parameter set can be seen in figure 2.1 (a). Although the time trace seems unpredictable, the dynamics' inherent structure can be seen in the state space representation depicted in figure 2.1 (b).

Four different routes lead to chaos in dynamical systems: period-doubling, intermittency, the Ruelle-Takens route and the crisis route [21, 96, 100–102]. The two relevant routes for this thesis are period-doubling and intermittency. The bifurcations involved are explained in more detail in the next section.

As a system undergoes the period-doubling route to chaos, an infinite cascade of period-doubling bifurcations (see section 2.1.6.9) occurs that accumulates at some finite parameter value, after which a chaotic attractor emerges.

As a system undergoes the intermittency route to chaos, a stable periodic orbit disappears and is replaced by a chaotic attractor. The chaotic attractor appears by either a fold of periodic orbits (see section 2.1.6.1), a subcritical Andronov-Hopf bifurcation (see section 2.1.6.3) or an inverse period-doubling bifurcation (see section 2.1.6.9) [102]. Almost periodic dynamics interrupted by bursts characterize the intermittent behavior.

2.1.6 *List of Bifurcations*

Usually, when a control parameter of a dynamical system is changed, the vector field defined by the right-hand side changes continuously and remains topologically equivalent to the system with unchanged parameters.

However, a slight change in a control parameter can also lead to a sudden change in the phase portrait. Then, the system with the changed control parameter is no longer topologically equivalent to that with unchanged parameters. In this case, it is said that the dynamical system experiences a bifurcation.

Bifurcations can be classified according to the following criteria:

- *local vs. global:* If the bifurcation type can be detected by a linear stability analysis of a steady state, it is called local. Otherwise, it is called global. Local bifurcations can be detected as one or more eigenvalues cross the imaginary axis. An important concept for local bifurcations is the normal form [103]. For a given local bifurcation, the normal form is a simplified dynamical system that is topologically equivalent to all dynamical systems close around a steady state that undergoes the same type of bifurcation. Global bifurcations differ from each other by the scaling of the amplitude and period of the involved subsets.
- *super- vs. subcritical:* If the solution that emerges from a bifurcation is stable, the bifurcation is called supercritical.
- *structurally stable vs. unstable:* A bifurcation is called structurally stable if it persists when the dynamical system itself is slightly perturbed. Otherwise, it is called structurally unstable. One example of a structurally unstable bifurcation is the pitchfork bifurcation (see section 2.1.6.2), as it possesses the symmetry $f(x) = -f(-x)$ that is broken when f is perturbed.
- *codimension:* The number of control parameters that must be varied for the bifurcation to occur. Most of the bifurcations presented in this subsection are of codimension-one. However, the Bogdanov-Takens bifurcation (see section 2.1.6.6), for instance, needs two parameters to unfold fully and is, therefore, codimension-two.

The rest of this subsection presents the bifurcations that appear in the main part of this thesis.

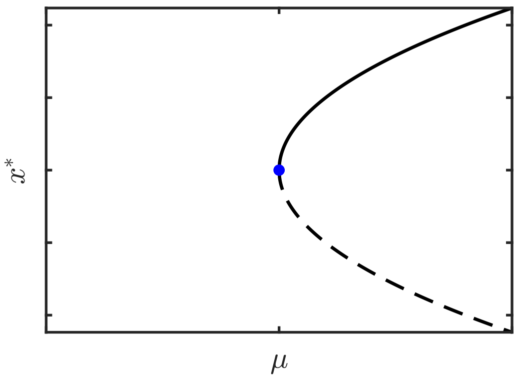

Figure 2.2: Steady states x^* against the bifurcation parameter μ for the fold normal form (2.27). Black solid line: Stable steady state. Black dashed line: Unstable steady state. Blue point: Fold bifurcation.

2.1.6.1 *Fold Bifurcation*

In a fold bifurcation, two steady states collide and annihilate. Close to a fold bifurcation, the dynamical system (2.6) is equivalent to the normal form

$$\dot{x} = \mu - x^2. \tag{2.27}$$

The steady states of equation (2.27) are given by $x^* = \pm\sqrt{\mu}$ and the bifurcation occurs at $\mu = 0$. Going from a negative to a positive value of μ, a stable and an unstable steady state starts to exist. Reversing the direction, a stable and an unstable steady state collide and annihilate.

The bifurcation is called fold bifurcation because the steady state curve folds back, as depicted in figure 2.2. It is also known as saddle-node bifurcation as a saddle (unstable steady state) collides with a node (stable steady state).

The fold bifurcation is a local bifurcation that can be detected as an eigenvalue of the Jacobi matrix crosses the origin.

It is one of two structurally stable codimension-one bifurcations, the other being the Andronov-Hopf bifurcation (see section 2.1.6.3).

2.1.6.2 *Pitchfork Bifurcation*

In a pitchfork bifurcation, a steady state changes its stability as two other steady states emerge. Close to a pitchfork bifurcation, the dynamical system (2.6) is equivalent to the normal form

$$\dot{x} = \mu x \pm x^3, \tag{2.28}$$

where the bifurcation is supercritical if a negative sign is chosen and subcritical otherwise. The steady states of equation (2.28) are

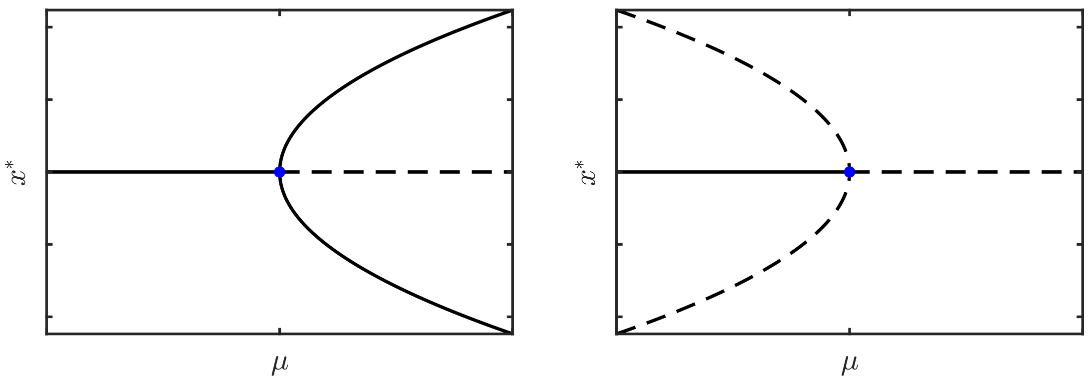

(a) Supercritical pitchfork (b) Subcritical pitchfork

Figure 2.3: Steady states x^* against the bifurcation parameter μ for the pitchfork normal form (2.28). Black solid line: Stable steady state. Black dashed line: Unstable steady state. Blue point: Pitchfork bifurcation.

given by $x^* = 0$ and $x^* = \pm\sqrt{\pm\mu}$, where the ± inside the square root has the same sign as in equation (2.28). At $\mu = 0$ the steady state at the origin loses its stability, and two steady states emerge. In the supercritical case, both emerging steady states are stable, see figure 2.3 (a). In the subcritical case, the emerging steady states are unstable (cf. figure 2.3 (b)).

The pitchfork bifurcation is not structurally stable, as it possesses the symmetry $f(x) = -f(-x)$. If a constant or quadratic term is introduced into equation (2.28), the pitchfork bifurcation ceases to exist. Figure 2.4 illustrates the consequences of a symmetry breaking with a bifurcation diagram of a structural perturbed pitchfork normal form given by

$$\dot{x} = -3/2 + \mu x + 1/4x^2 - x^3. \tag{2.29}$$

Instead of a single branch undergoing a pitchfork bifurcation, for equation (2.29) two seperate branches exist, one of which folds.

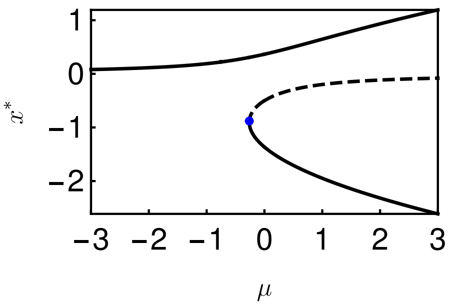

Figure 2.4: Steady states x^* against the bifurcation parameter μ for the structurally perturbed pitchfork normal form (2.29). Black solid line: Stable steady state. Black dashed line: Unstable steady state. Blue point: Fold bifurcation.

2.1.6.3 *Andronov-Hopf Bifurcation*

At an Andronov-Hopf bifurcation, a periodic orbit emerges from a steady state as the steady state changes its stability. The behaviour of the dynamical system (2.6) close to the bifurcation is given by the normal form

$$\dot{r} = \mu r \pm r^3, \tag{2.30}$$

$$\dot{\theta} = 1. \tag{2.31}$$

Note that the system (2.30)-(2.31) is represented in polar coordinates r and θ, which relate to cartesian coordinates x and y as

$$x = r\cos(\theta), \tag{2.32}$$

$$y = r\sin(\theta). \tag{2.33}$$

Consequently, $r = 0$, $\dot{\theta} = 1$ is considered a steady state because it is steady in the cartesian coordinates, i. e., $\dot{x} = \dot{y} = 0$ holds.

While for $\mu < 0$ the steady state at $r = 0$ at the origin is stable, it loses its stability for $\mu > 0$ as a periodic orbit emerges at $\mu = 0$. Figure 2.5 depicts the bifurcation diagram of a supercritical Andronov-Hopf bifurcation.

An Andronov-Hopf bifurcation can be detected from linear stability analysis as a complex conjugated pair of eigenvalues crosses the imaginary axis.

In the subcritical case without higher order terms, the system would diverge to $\pm\infty$ for certain initial conditions. Including higher-order terms, the unstable branch folds back and becomes stable resulting in all trajectories staying bounded. The normal form of a subcritical Andronov-Hopf bifurcation with the addition of a stabilizing fifth-order term reads

$$\dot{r} = \mu r + r^3 - r^5, \tag{2.34}$$

$$\dot{\theta} = 1. \tag{2.35}$$

At $\mu = 0$ the steady state at the origin loses its stability in an Andronov-Hopf bifurcation as an unstable periodic orbit emerges. This periodic orbit folds back at $\mu = -1/4$, where it becomes and remains stable. The bifurcation diagram of the normal form with the addition of a fifth-order term is depicted in figure 2.6.

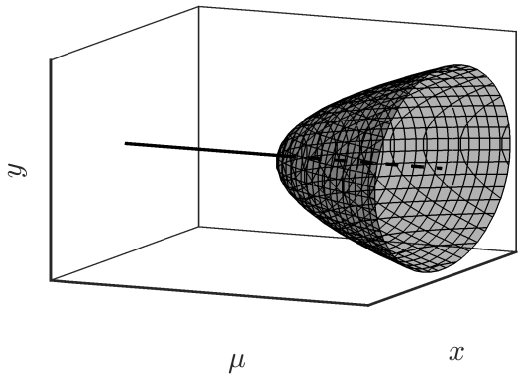

Figure 2.5: Bifurcation diagram of a supercritical Andronov-Hopf bifurcation (2.30)-(2.31). As the bifurcation parameter μ passes zero, the previously stable steady state in the origin loses its stability as a stable periodic orbit emerges.

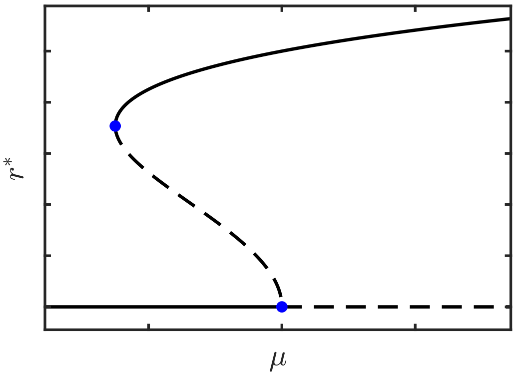

Figure 2.6: Bifurcation diagram of a subcritical Andronov-Hopf bifurcation (2.34)-(2.35). As the bifurcation parameter μ passes zero, the previously stable steady state in the origin loses its stability as an unstable periodic orbit emerges. The unstable periodic orbit regains its stability in a fold of periodic orbits. Stability is indicated with a solid line, dashed otherwise. Blue dots mark the bifurcation points.

2.1.6.4 *Homoclinic Bifurcation*

In a homoclinic bifurcation, a periodic orbit collides with an unstable steady state, after which the periodic orbit ceases to exist.

At the bifurcation point, a periodic orbit with an infinite period exists that connects the steady state with itself. This orbit that connects an unstable steady state with itself is called a homoclinic orbit.

As the homoclinic bifurcation is global, it cannot be detected by linear stability analysis, and no normal form exists. An example system that exhibits a homoclinic bifurcation is [92]

$$\dot{x} = y, \tag{2.36}$$

$$\dot{y} = x + \mu y - x^2 + xy, \tag{2.37}$$

where the homoclinic bifurcation occurs at $\mu = \mu_c \approx -0.86$. For $\mu < \mu_c$ a periodic orbit, a stable and an unstable steady state exist. At $\mu = \mu_c$ the periodic orbit collides with the unstable steady state forming a homoclinic orbit. For $\mu > \mu_c$ the periodic orbit ceases to exist, and only the two steady states remain.

It can be shown that the period of the periodic orbit close to the homoclinic bifurcation scales as $\mathcal{O}(\log(\mu - \mu_c))$ [92].

2.1.6.5 *SNIPER Bifurcation*

At a SNIPER bifurcation (short for saddle-node infinite period bifurcation), a stable steady state collides with an unstable steady state as a periodic orbit with infinite period and finite amplitude emerges.

An example system that exhibits the SNIPER bifurcation reads [92]

$$\dot{r} = r(1 - r^2), \tag{2.38}$$

$$\dot{\phi} = \mu - \sin(\phi). \tag{2.39}$$

The SNIPER bifurcation occurs at $\mu = \mu_c = 1$. For $\mu < 1$ a stable and an unstable steady state exist that collide at $\mu = 1$, at which point a periodic orbit of finite amplitude starts to exist. For $\mu > 1$ the steady states disappear, and only the periodic orbit remains.

It can be shown that the period of the periodic orbit close to the sniper bifurcation scales as $\mathcal{O}((\mu - \mu_c)^{-\frac{1}{2}})$ [92].

Table 2.1 summarizes the periodic orbit's scaling of the amplitude and period close to an Andronov-Hopf, a homoclinic and a SNIPER bifurcation.

Table 2.1: Scalings of a periodic orbit's amplitude and period close to different bifurcations [92]. μ is the control parameter of the bifurcation that occurs at $\mu = 0$.

Bifurcation	Amplitude	Period
Andronov-Hopf	$\mathcal{O}(\sqrt{\mu})$	$\mathcal{O}(1)$
Homoclinic	$\mathcal{O}(1)$	$\mathcal{O}(\log \mu)$
Sniper	$\mathcal{O}(1)$	$\mathcal{O}(\mu^{-\frac{1}{2}})$

2.1.6.6 *Bogdanov-Takens Bifurcation*

The Bogdanov-Takens bifurcation is a codimension-two bifurcation from which two branches of fold bifurcations, an Andronov-Hopf bifurcation and a homoclinic bifurcation originate.

At the Bogdanov-Takens bifurcation, a steady state exists with an eigenvalue $\lambda = 0$ with a multiplicity of two.

Close to the bifurcation and under certain non-degeneracy conditions, the dynamical system (2.6) behaves as [104]

$$\dot{x} = y, \tag{2.40}$$

$$\dot{y} = \mu_1 + \mu_2 x + y^2 \pm xy, \tag{2.41}$$

where the bifurcation occurs at $(\mu_1, \mu_2) = (0, 0)$. Choosing a negative sign for ± results in a supercritical Andronov-Hopf bifurcation, whereas a positive sign results in a subcritical Andronov-Hopf bifurcation.

The two fold curves are given by $\mu_1 = \frac{1}{4}\beta_2^2$, $\beta_2 > 0$ and $\beta_2 < 0$. The Andronov-Hopf curve is parameterized by the half line $\beta_1 = 0$, $\beta_2 < 0$. The approximation of the homoclinic curve reads $\mu_1 = -\frac{6}{25}\mu_2^2 + \mathcal{O}(|\mu_2|^3)$, $\mu_2 < 0$ [104].

2.1.6.7 *Fold of Periodic Orbits*

In a fold of periodic orbits, two periodic orbits collide and annihilate each other. As the dynamics for profiles of a specific length can be written as an iterative map (see section 2.1.4), the bifurcation is considered a local bifurcation of the amended dynamical system acting on periodic profiles.

As the system undergoes a fold of periodic orbits, one Floquet multiplier crosses through the unit circle at $\mu = 1$.

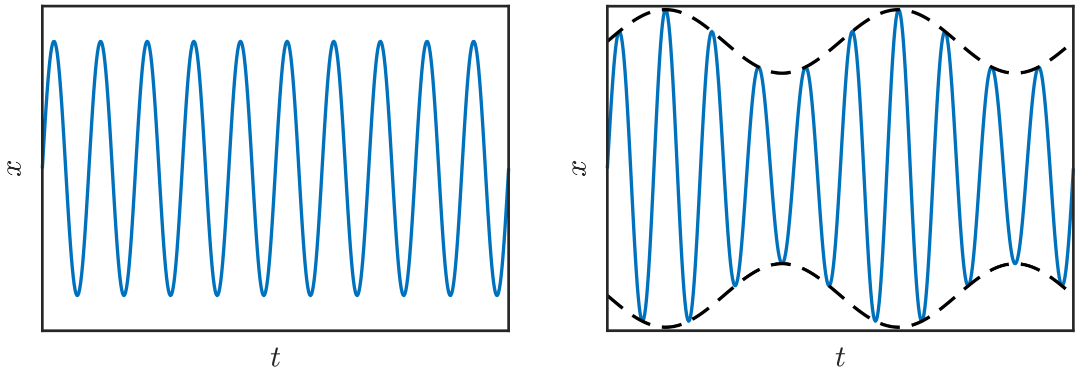

(a) $\mu < \mu_c$

(b) $\mu > \mu_c$

Figure 2.7: Example time trace of a periodic orbit before $\mu < \mu_c$ (a) and after $\mu > \mu_c$ (b) a torus bifurcation occurred. The dashed line indicates the slowly varying envelope.

2.1.6.8 *Torus Bifurcation*

In a torus bifurcation, a periodic orbit changes its stability as a solution with an additional frequency emerges. If the frequency ω_T introduced by the bifurcation is commensurate with the frequency of the original periodic orbit ω_P, i. e., $\omega_T / \omega_P \in \mathbb{Q}$, the emerging solution is another periodic orbit. Otherwise, the solution that emerges is quasi-periodic.

Figure 2.7 shows a simple example of a periodically repeating time trace undergoing a torus bifurcation.

As the system undergoes a torus bifurcation, a pair of Floquet multipliers crosses the unit circle at $\mu = e^{\pm i\phi}$.

2.1.6.9 *Period-Doubling Bifurcation*

At a period-doubling bifurcation, a periodic orbit changes its stability as a periodic orbit with twice the original period emerges.

An example of a period-doubling bifurcation is depicted in figure 2.8.

As the system undergoes a period-doubling bifurcation, a Floquet multiplier crosses the unit circle at $\mu = -1$.

2.1.7 *Delayed Dynamical Systems*

So far, for the introduction of dynamical systems ODEs have been sufficient. They allow linking the rate of change to the state at the current time.

However, as information takes a finite time to propagate, in some cases it is necessary to incorporate the resulting delay into the modeling

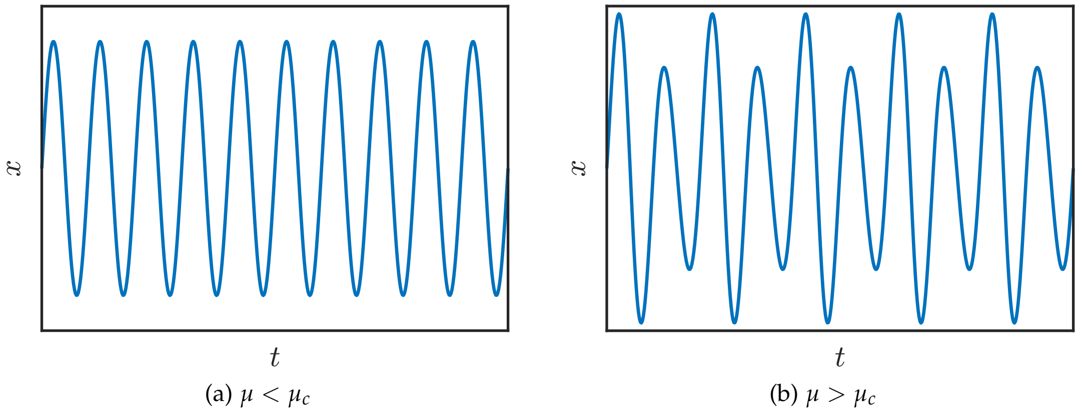

(a) $\mu < \mu_c$

(b) $\mu > \mu_c$

Figure 2.8: Example time trace of a periodic orbit before $\mu < \mu_c$ (a) and after $\mu > \mu_c$ (b) a period-doubling bifurcation occurred.

to obtain accurate results. Systems that link the rate of change to the state at previous times are called delayed dynamical systems (DDS).

This section introduces the different delayed dynamical systems important for this thesis and highlights the differences to ordinary dynamical systems.

2.1.7.1 *Delayed Differential Equations*

A delayed differential equation (DDE) with a single constant delay $\tau > 0$ can be written as

$$\dot{x}(t) = f(x(t), x(t-\tau)). \tag{2.42}$$

While for ODEs (2.6) the state is conventionally written as a vector of real numbers in $\mathbb{R}^d$, for DDEs the state x at time t is a vector of continuous real functions $\mathcal{C} = C([t-\tau, t], \mathbb{R}^d)$ on the interval $[t-\tau, t]$. Therefore, the history of x from $t-\tau$ to t needs to be known to determine the time evolution of x.

The method of steps [105, 106] illustrates why solutions of (2.42) become smoother over time. The idea is to integrate one step of length τ after the other. First, define $x^n(t) = x(n\tau + t)$, $n \in \mathbb{Z}$, $t \in [0, \tau]$ as the solution of the nth step. The solution of the following step x^{n+1} can then be computed as

$$x^{n+1}(t) = x^n(\tau) + \int_0^t f(x^{n+1}(t'), x^n(t'))\,\mathrm{d}t'. \tag{2.43}$$

Hence, if x^n is k times differentiable, x^{n+1} is at least $k+1$ times differentiable because of the integration that takes place in equation (2.43).

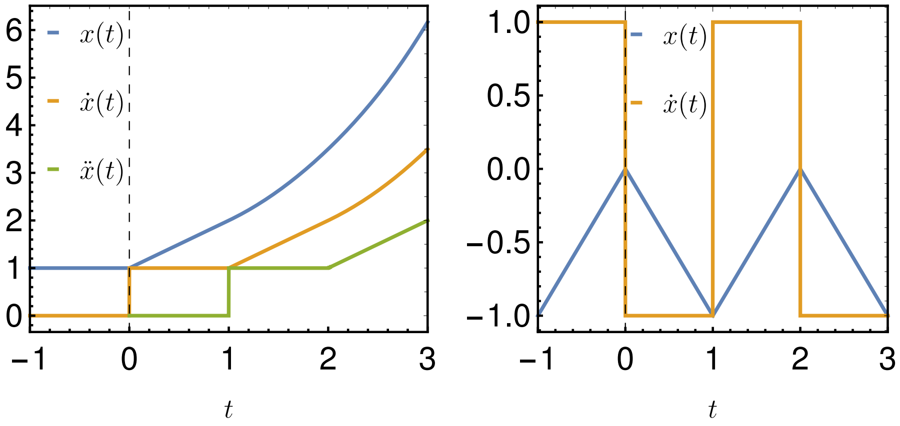

(a) DDE

(b) NDDE

Figure 2.9: Differences in the smoothing of discontinuities for DDEs and NDDEs. (a) The DDE system $\dot{x} = x(t - \tau)$ with initial function $x(t) = 1$, $t < 0$ has a jump discontinuity in the nth derivative at $t = (n-1)\tau$, i. e., the solution becomes smoother over time. (b) The NDDE system $\dot{x} = \dot{x}(t - \tau)$ with initial function $x(t) = t$, $t < 0$ has a discontinuity for $\dot{x}$ at $t = n\tau$, $n \in \mathbb{N}$, i. e., the solution retains its smoothness.

One example system for the smoothing property of DDEs is

$$\dot{x}(t) = x(t - \tau). \tag{2.44}$$

The initial condition $x(t) = 1$ for $t < 0$ results in the nth derivative having a jump discontinuity at $t = (n-1)\tau$. A time trace of this system is depicted in figure 2.9 (a).

DDEs cannot be integrated back in time uniquely. The system

$$\dot{x}(t) = x(t - \tau)(x(t) - 1) \tag{2.45}$$

has the solution $x(t) = 1$ for $t > 0$ as long as $x(0) = 1$ holds independent of the initial function. Figure 2.10 depicts three different time-traces of equation (2.45) with the initial function fulfilling $x(0) = 1$.

Although the state space of DDEs is infinite-dimensional even for infinitesimal delays, an attractor's dimension is always finite, and only a finite number of eigenvalues are involved in a local bifurcation.

2.1.7.2 *Neutral Delayed Differential Equations*

Neutral delayed differential equations (NDDEs) allow a delayed state and a delayed derivative to appear in the right-hand side of the system. NDDEs can be written as

$$\dot{x}(t) = f(x(t), x(t - \tau), \dot{x}(t - \tau)). \tag{2.46}$$

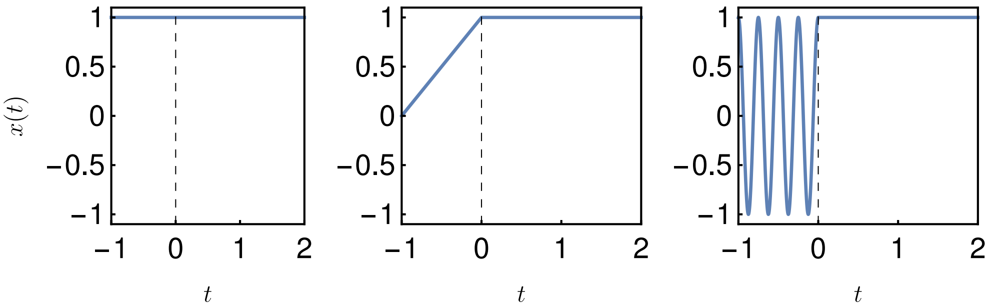

(a) $x_0(t) = 1$ (b) $x_0(t) = t + 1$ (c) $x_0(t) = \cos(8\pi t)$

Figure 2.10: Demonstration that DDEs cannot be uniquely integrated backward in time. The system $\dot{x}(t) = x(t-\tau)(x(t)-1)$ with initial function $x(t) = x_0(t)$, $t < 0$ has the solution $x(t) = 1$, $t > 0$ as long as $x(0) = 1$ holds independent of the initial function.

In general, NDDEs do not have the same smoothing property as discussed for DDEs but retain their smoothness. The smoothness does not change because the integral in the method of steps (2.43) additionally contains the derivative of x. The example system

$$\dot{x}(t) = \dot{x}(t-\tau) \tag{2.47}$$

with initial function $x(t) = t$ for $t < 0$ has a jump discontinuity for $\dot{x}(t)$ at $t = n\tau$, $n \in \mathbb{N}$. Figure 2.9 (b) shows the time-trace of equation (2.47).

In contrast to DDEs, NDDEs with neutral terms can uniquely be integrated back in time because the the smoothness of the solution is retained.

While for DDEs only a finite number of eigenvalues can be involved in a local bifurcation, infinitely many eigenvalues may cross the imaginary axis simultaneously for NDDEs [107, 108].

In the context of this thesis, NDDEs appear in the derivations of normal forms (see section 3.3) where the delayed algebraic differential equations (see section 2.1.7.3) are rewritten as NDDEs to make the calculations more compact.

2.1.7.3 *Delayed Algebraic Differential Equations*

The most general delayed equation considered in this thesis is called a delay algebraic differential equation (DADE). Its characteristic is that it combines time delay with algebraic conditions, which do not need to contain a time derivative. A DADE can be written as

$$M\dot{x}(t) = f(x(t), x(t-\tau)) \tag{2.48}$$

with the mass matrix $M \in \mathbb{R}^{n\times n}$, which is allowed to be singular.

When modeling coupled optical micro-cavities, DADEs appear naturally because the output of one cavity is injected into another cavity. Because the electrical field takes time to propagate from one cavity to another, the injected field of each cavity is given as a delayed algebraic condition. In contrast, the dynamics for the electrical field inside the cavity and the carriers are given by ordinary differential equations.

The right-hand side of a DADE (2.48) does not allow for delayed derivates, as is the case for NDDEs (2.46). However, every NDDE can still be written as a DADE, implying that DADEs are a superset of NDDEs. To demonstrate this, the new variable $y = f(x, x_\tau, y_\tau)$ is introduced, which allows to write equation (2.46) as

$$\dot{x} = f(x, x_\tau, y_\tau) \tag{2.49}$$

$$0 = y - f(x, x_\tau, y_\tau). \tag{2.50}$$

Therefore, every NDDE can be written as a DADE with, at maximum, twice as many variables as the original NDDE system. Not every DADE can be written as a NDDE as the next example shows.

Delay algebraic differential equations can be acausal, i. e., depend on future times, although all delays point to past times. An example is the system defined by

$$\dot{x}(t) = y(t) \tag{2.51}$$

$$0 = y(t - \tau) + x(t). \tag{2.52}$$

Shifting equation (2.52) by τ, solving for $y(t)$ and inserting it into equation (2.51) reveals

$$\dot{x}(t) = x(t + \tau), \tag{2.53}$$

i. e., that the derivative of x depends on future times. DADEs with this property are said to be of advanced type [109, 110].

2.1.7.4 *Spectral Properties*

Linearizing a DADE (2.48) around a steady state following the approach presented in section 2.1.3 results in the characteristic equation

$$|J_x(x^*) + e^{\lambda\tau} J_{x_\tau}(x^*) - M\lambda| = 0, \tag{2.54}$$

where J_x and J_{x_τ} are the Jacobi-matrices with respect to the non-delayed variables $x(t)$ and delayed variables $x(t - \tau)$, respectively.

In the limit of long delays $\tau \to \infty$, the spectrum becomes quasi-continuous, which makes the analytical treatment of the characteristic equation easier. As stated in [72, 111], making the ansatz

$$\lambda = -\frac{\ln|Y(\omega)|}{\tau} + i\omega \tag{2.55}$$

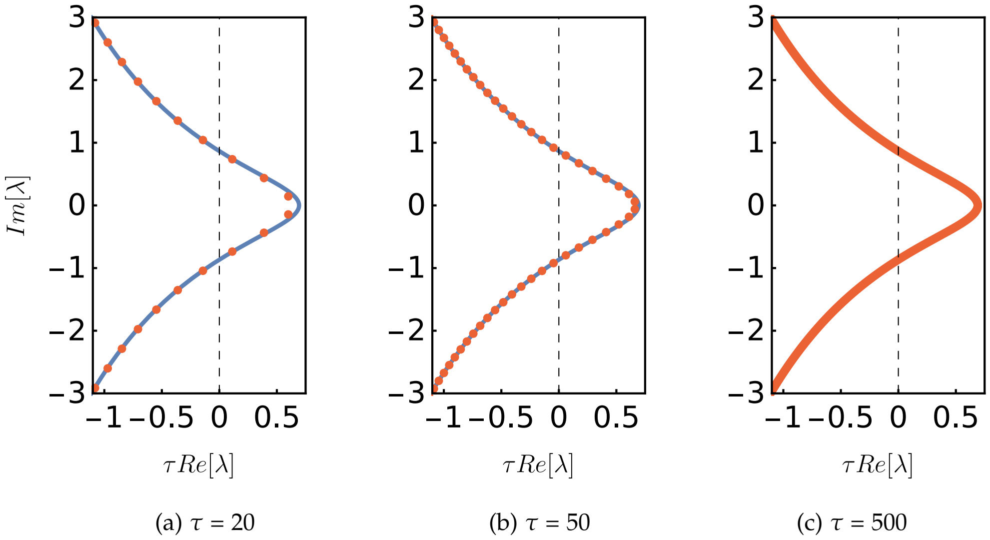

(a) $\tau = 20$ (b) $\tau = 50$ (c) $\tau = 500$

Figure 2.11: Delayed-type spectrum of the characteristic function $\chi(\lambda) = \lambda + 1/2 + e^{-\lambda\tau}$ as it approaches the long delay limit. As $\tau \to \infty$, the spectrum becomes quasi-continuous. Red dots: Eigenvalues. Blue line: Quasi-continuous spectrum (2.55).

and inserting it into (2.54) as well as neglecting all terms of order $\mathcal{O}\left(\tau^{-1}\right)$ results in

$$|-i\omega M + J_x(x^*) + J_{x_\tau}(x^*)Y(\omega)| = 0. \tag{2.56}$$

The eigenvalues in the long delay limit are given by equation (2.55), where $Y(\omega)$ are solutions of equation (2.56). The transition of the spectrum to the long delay limit is depicted in figure 2.11.

In contrast to ODEs, the characteristic function of a delayed dynamical system is not a polynomial in the eigenvalue λ but an exponential polynomial. Exponential polynomials can be written as

$$\chi(\lambda) = P(\lambda) + Q(\lambda)e^{-\lambda\tau}, \tag{2.57}$$

where $P(\lambda)$ and $Q(\lambda)$ are polynomials in λ. Assuming $Q(\lambda) \not\equiv 0$, there are three cases for the zeros of $\chi(\lambda)$ depending on the degree of P and Q [107, 108]:

1. *Delayed case:* If $\deg P > \deg Q$, then $\chi(\lambda)$ has only a finite amount of zeros with a positive real part and an infinite amount of zeros with an arbitrarily large negative real part.
2. *Neutral case:* If $\deg P = \deg Q$, then $\chi(\lambda)$ has an infinite amount of zeros given by

$$\lambda = \frac{1}{\tau}\left(\ln(|K|) + i(Arg(K) + (2k-1)\pi)\right) + \mathcal{O}(1), \quad k \in \mathbb{Z} \tag{2.58}$$

where $K = -q/p$ and q and p are the highest order coefficients of Q and P, respectively. There are only a finite number of other zeros.

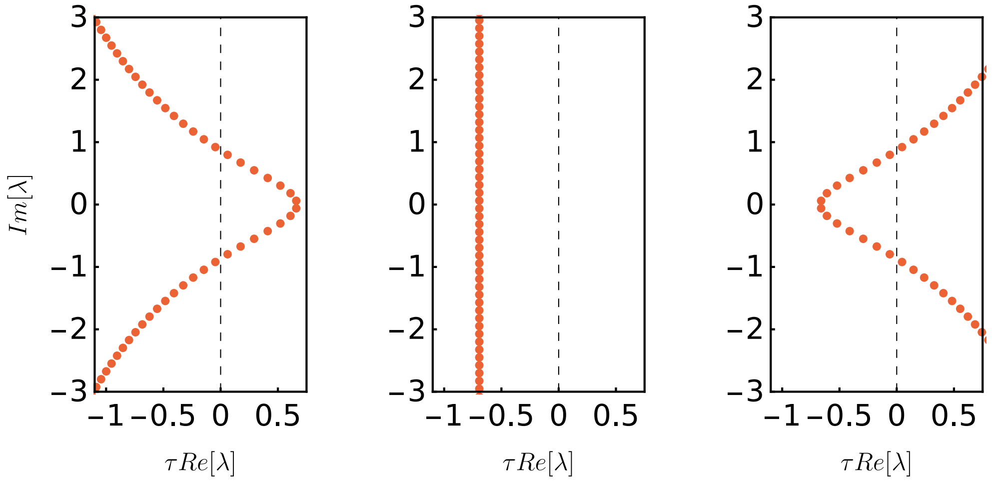

(a) Delayed case (b) Neutral case (c) Advanced case

Figure 2.12: Example spectra of delayed dynamical systems. All spectra have an infinite amount of eigenvalues. The characteristic functions are $\chi(\lambda) = \lambda + 1/2 + e^{-\lambda\tau}$ (a), $\chi(\lambda) = e^{-\lambda\tau} + 2$ (b) and $\chi(\lambda) = \lambda e^{-\lambda\tau} - e^{-\lambda\tau}/2 - 1$ (c).

3. *Advanced case:* If $\deg P < \deg Q$, then $\chi(\lambda)$ has only a finite amount of zeros with a negative real part and an infinite amount of zeros with an arbitrarily large positive real part.

Figure 2.12 shows exemplary spectra for each of the three cases.

2.1.8 *Spatially Extended Systems*

Dynamical systems that depend on time and space are called spatially extended systems. The time evolution is given by a partial differential equation (PDE) that can be written as

$$\partial_t \psi(x,t) = f(\psi, \nabla, \nabla^2, \ldots), \tag{2.59}$$

i. e., the right-hand side of the system is allowed to depend on partial derivatives of the space variables of ψ, which are indicated with the nabla operator $\nabla = \left(\frac{\partial}{\partial x_1}, \ldots, \frac{\partial}{\partial x_n}\right)$.

PDEs are relevant in the context of this thesis as they appear as the master equations [23] that are derived from the DADEs using multiscale analysis (see section 3.3) and the functional mapping method (see section 3.1.3).

DDSs can be seen as spatially extended systems with unusual boundary conditions. For this, one can define a space-like variable $z \in [0, \tau]$ and a discrete time-like variable $\sigma \in \mathbb{N}$ for the DDS (2.48) as

$$x(\sigma, z) = x(\sigma\tau + z). \tag{2.60}$$

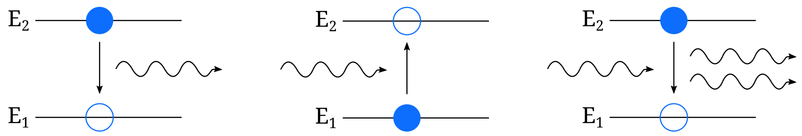

(a) Spontaneous emission (b) Absorption (c) Stimulated Emission

Figure 2.13: Light interacting with matter. An electron may transition between two energy levels spontaneously emitting a photon (a), absorbing a photon (b) or stimulated by a photon emitting a second photon (c).

Then the original DDS turns into a PDE with discrete time and the boundary condition

$$x(\sigma+1,0)=x(\sigma,\tau). \tag{2.61}$$

If the delay is large, σ and z decouple to some extent because they act on different time scales. This decoupling, in turn, might allow for additional insights into the properties of the dynamical system [72].

For a more thorough review of the similarities between DDSs and PDEs in the long delay limit, see [72].

2.2 LASER MODELING

A laser (short for light amplification by stimulated emission of radiation) is a device that emits light by stimulated emission that is optically amplified [112, 113].

Three processes involving electrons and photons are relevant for this thesis: spontaneous emission, absorption and stimulated emission [4]. A schematic of these processes is depicted in figure 2.13.

Spontaneous emission (cf. figure 2.13 (a)) occurs when an electron spontaneously transitions from an excited energy state to a lower energy state. In the process, a photon is emitted with the energy of the difference between the two states.

The reverse process is called absorption (see figure 2.13 (b)) . In this process, a photon excites an electron from a lower energy state to an excited state, after which the photon is annihilated. For this to occur, the photon's energy needs to be equal to the energy difference between the two states of the electron.

Instead of occurring spontaneously, the transition of an electron from a high to low energy state can be induced by a photon. This process is called stimulated emission and results in a perfect copy of the photon that initiated the process, see figure 2.13 (c).

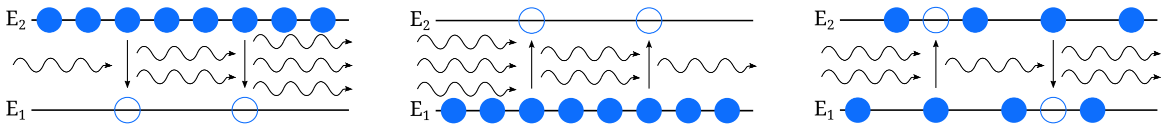

(a) Gain

(b) Absorber

(c) Transparency

Figure 2.14: Different electron distributions in optical media. (a) If most electrons are in an excited state, passing photons are amplified by stimulated emission. (b) If most electrons are in the lower energy state, passing photons are absorbed. (c) If the likelihood for an electron to be in the excited state is the same as in the low energy state, the number of photons stays the same after passing the medium.

Light is amplified, damped, or unchanged when passing a medium depending on the electron state distribution inside a medium. These three cases are depicted in figure 2.14.

The first case corresponds to a gain medium, see panel (a). The electrons are mainly in a high-energy state called population inversion. Therefore, an appropriate photon that passes is amplified by the process of stimulated emission.

In an absorber, the scenario is reversed, see figure 2.14 (b). Most of the electrons are in a lower energy state. As a result, passing photons are absorbed, which leads to the electron transitioning to the excited state.

If the likelihood of an electron being in the excited state is the same as in the low energy state, the number of photons stays the same after passing the medium, cf. figure 2.14 (c). In this case, the medium is transparent. In both an absorber and a gain medium the process saturates for large intensities resulting in a transparent medium.

In general, a laser typically consists of three components: a gain medium, an external energy source that inverses the population in the gain medium and a cavity. The first two ensure that a photon is amplified by the process of stimulated emission, while the latter ensures that a photon passes the gain medium multiple times.

The most general way to model the dynamics of a laser system includes differential equations for electrical fields, carrier inversions and polarizations induced by the active media. Depending on the laser system, the polarizations and carrier inversions can be eliminated adiabatically. Based on this, laser models are classified as either type A, B or C [114]. Class A laser models contain only the electrical field, class B laser models contain the electrical field and carrier inversions, and class C laser models contain all three components.

All investigated systems in this thesis are modeled as class B lasers and can be derived from first principles starting at Maxwell's equations.

2.2.1 *Model Derivation*

In this thesis, a mode-locked integrated external-cavity surface-emitting laser (MIXSEL) as well as a vertical cavity surface-emitting laser coupled to a resonant saturable absorber mirror (VCSEL-RSAM) are investigated. A model for both setups can be derived from first principles starting at Maxwell's equations. What follows is a short a derivation sketch of the equations that govern both systems' behavior. This subsection follows [32], where further derivation are detailed.

2.2.1.1 *Maxwell's Equations*

Maxwell's equations for a non-magnetizable material without free charges or currents for the electrical field $E(r,t)$ and magnetic flux density $B(r,t)$ read

$$\nabla \cdot D = 0, \tag{2.62}$$

$$\nabla \cdot B = 0, \tag{2.63}$$

$$\nabla \times E = -\dot{B}, \tag{2.64}$$

$$\nabla \times H = \dot{D}. \tag{2.65}$$

The electric displacement D and the magnetic field H are given by

$$D = \epsilon_0 E + P = \epsilon_0 (1+\chi) E, \tag{2.66}$$

$$H = \frac{B}{\mu_0}. \tag{2.67}$$

Here, χ is the electric susceptibility, $P = \epsilon_0 \chi E$ is the material induced polarization, ϵ_0 is the permittivity and μ_0 is the permeability of the vacuum [115].

The polarization can be separated into a linear P_b and nonlinear P_{nl} contribution, which read

$$P = P_b + P_{nl} = \epsilon_0 \chi_b E + \epsilon_0 \chi_{nl} E, \tag{2.68}$$

where χ_b and χ_{nl} are the background electric susceptibility and the nonlinear electric susceptibility, respectively. The electric displacement can then be written as

$$D = \epsilon_0 (1+\chi_b) E + \epsilon_0 \chi_{nl} E = \epsilon_0 \epsilon_r E + P_{nl}, \tag{2.69}$$

where ϵ_r is the relative permittivity.

2.2.1.2 *Wave Equation*

The derivation's first step is obtaining a wave equation for the electrical field in the transverse direction.

Rotating equation (2.64) yields

$$\nabla \times (\nabla \times E) = \nabla \times (-\dot{B}) = -\mu_0 \nabla \times \dot{H}. \tag{2.70}$$

Making use of the vector identity

$$\nabla \times (\nabla \times E) = \nabla(\nabla \cdot E) - \nabla^2 E, \tag{2.71}$$

equation (2.70) transforms into

$$\nabla(\nabla \cdot E) - \nabla^2 E = -\mu_0 \ddot{D}, \tag{2.72}$$

where equation (2.65) was used to replace $\nabla \times \dot{H}$.

Assuming the divergence of the nonlinear polarization is small, i. e., $\nabla \cdot P_{nl} \ll 1$, it follows from equations (2.62) and (2.69) that $\nabla \cdot E = 0$. Equation (2.72) then simplifies to

$$\nabla^2 E - \frac{n_b^2}{c^2} \ddot{E} = \mu_0 \ddot{P}_{nl}, \tag{2.73}$$

where equation (2.69) has been used to replace D. In equation (2.73) $n_b = \sqrt{\epsilon_r}$ is the background reflective index and $c = 1/\sqrt{\epsilon_0 \mu_0}$ is the speed of light in vacuum.

Writing equation (2.73) equation in Fourier space $\partial_t \to -i\omega$ gives

$$\left(\nabla^2 + \omega^2 \frac{n_b^2}{c^2} \right) \hat{E} = -\omega^2 \mu_0 \hat{P}_{nl} = -\frac{\omega^2}{c^2} \chi_{nl} \hat{E} \tag{2.74}$$

as the nonlinear wave equation for the electrical field in three dimensions.

From here, assume that the transverse mode $\Phi(r_\perp)$ is constant so that the separation ansatz

$$\hat{E}(r, \omega) = \Phi(r_\perp, \omega) \hat{E}_\perp(z, \omega) e_\perp \tag{2.75}$$

is valid. The transverse mode $\Phi(r_\perp, \omega)$ solves the Helmholtz equation with proper boundary conditions [116]

$$\left(\nabla_\perp^2 + \frac{\omega^2}{c^2} n_\perp^2(r_\perp, \omega) \right) \Phi(r_\perp, \omega) = \frac{\omega^2}{c^2} n_e^2 \Phi(r_\perp, \omega). \tag{2.76}$$

Inserting the ansatz for $\hat{E}$ into equation (2.74) and projecting on the transverse mode by multiplying with the conjugate of the mode Φ^* and integrating over the transverse dimensions leads to

$$\left(\frac{\partial^2}{\partial z^2} + \omega^2 \frac{n_e^2}{c^2} \right) \hat{E}_\perp e_\perp = -\frac{\omega^2}{c^2} \Gamma_\perp \chi_{nl}(0, z) \hat{E}_\perp(z) e_\perp. \tag{2.77}$$

In equation (2.77) the transverse confinement factor $\Gamma_\perp$ is defined as

$$\Gamma_\perp = \frac{\iint\limits_{AR} |\Phi(r_\perp)|^2 d^2 r_\perp}{\iint\limits_{-\infty}^{+\infty} |\Phi(r_\perp)|^2 d^2 r_\perp}, \tag{2.78}$$

where AR is the active region. AR is assumed to be centered around $r_\perp = 0$, while χ_{nl} is assumed to be constant inside AR and zero otherwise.

Further, defining the transverse polarization $\hat{P}_\perp$ as

$$\hat{P}_\perp(z) = \epsilon_0 \chi_{nl}(0, z) \hat{E}_\perp(z) \tag{2.79}$$

simplifies equation (2.77) to

$$\left(\frac{\partial^2}{\partial z^2} + \omega^2 \frac{n_e^2}{c^2} \right) \hat{E}_\perp = -\omega^2 \mu_0 \Gamma_\perp \hat{P}_\perp \tag{2.80}$$

as the final version of the wave equation for the transverse field.

2.2.1.3 *Electric Susceptibility Model*

For the electric susceptibility, the quantum wells are assumed to have a parabolic band structure following a Fermi distribution [117].

The susceptibility is assumed to be constant in frequency $\chi(\omega) \approx \chi(\omega_0)$, i. e., a mono-mode response of the micro-cavity is assumed, because the gain spectrum is broad compared to the micro-cavity mode. Hence, the susceptibility is linearized around the transparency level $\mathcal{N}^{(tr)}$ as

$$\chi_{nl} \approx \frac{\partial \chi_{nl}}{\partial \mathcal{N}} \left(\mathcal{N} - \mathcal{N}^{(tr)} \right). \tag{2.81}$$

The convention is to write equation (2.81) defining the differential gain coefficient $g_0 = -\partial_{\mathcal{N}} \operatorname{Im}[\chi_{nl}]$ and the linewidth enhancement factor (or Henry factor) $\alpha = (\partial_{\mathcal{N}} \operatorname{Re}[\chi_{nl}])/(\partial_{\mathcal{N}} \operatorname{Im}[\chi_{nl}])$, which quantifies the amplitude–phase coupling and accounts for the additional line broadening in semiconductor lasers [118, 119]. Then χ_{nl} reads

$$\chi_{nl} = -g_0(\alpha + i)(\mathcal{N} - \mathcal{N}^{(tr)}). \tag{2.82}$$

The time evolution of the carriers is given by a standard rate equation that only considers linear terms in $\mathcal{N}$ that can be written as

$$\frac{\partial \mathcal{N}}{\partial t} = \mathcal{J} - \gamma \mathcal{N} + \frac{\epsilon_b}{2\hbar} \operatorname{Im}[\chi_{nl}] |E|^2. \tag{2.83}$$

Here, $\mathcal{J}$ defines the population inversion, γ is the rate of spontaneous emission and the last term models the stimulated emission proportional to the electrical field intensity.

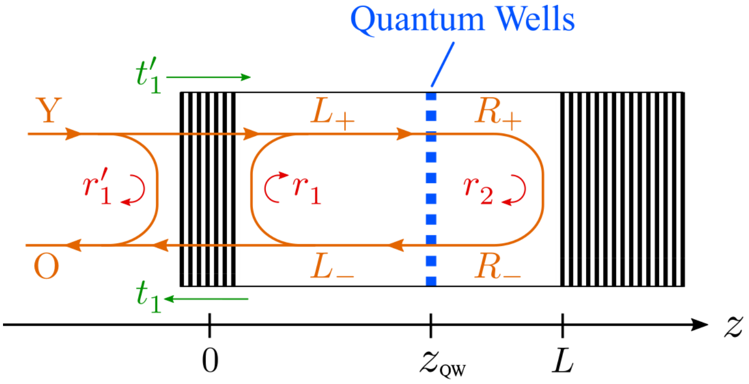

Figure 2.15: A schematic of a micro-cavity of length L with a quantum well layer at $z = z_{QW}$. The micro-cavity is closed by two distributed Bragg reflectors. R and L denote the intra-cavity field to the right and left of the quantum well, respectively, where $-$ and $+$ indicate a left and right moving wave, respectively. Y is the injection field, and O is the output field of the micro-cavity. t_i and r_i denote transmission and reflection coefficients inside the micro-cavity, respectively, with $i = 1$ indicating the top and $i = 2$ the bottom mirror. Coefficients from outside the micro-cavity are marked with primes. Adapted with permission from [32].

Inserting the susceptibility model (2.82) into the rate equation (2.83) yields the final model for the carriers

$$\frac{\partial \mathcal{N}}{\partial t} = \mathcal{J} - \gamma \mathcal{N} - \frac{\epsilon_b}{2\hbar} g_0 (\mathcal{N} - \mathcal{N}^{(tr)}) |E|^2. \tag{2.84}$$

2.2.1.4 *Micro-Cavity with Quantum Well*

This section derives a model for an injected micro-cavity setup with a thin quantum well (QW) region following [73]. The setup is depicted in figure 2.15.

Starting point is the wave equation (2.80) derived in section 2.2.1.2 that can be written as

$$\frac{\partial^2 \mathcal{E}}{\partial z^2} + \omega^2 \frac{n^2}{c^2} \mathcal{E}(\omega, z) = -\omega^2 \mu_0 \Gamma_\perp \mathcal{P}(\omega, z), \tag{2.85}$$

where $\mathcal{E}$ is the transverse electromagnetic field in Fourier space, $\mathcal{P}$ is the polarization of the QW region, $\Gamma_\perp$ is the confinement factor of the transverse mode, and n is the effective index of refraction of the transverse mode.

It is assumed that the quantum well region is thin compared to the wavelength $W \ll \lambda$ and positioned at $z = z_{QW}$ in a cavity of length L. The polarization is therefore written with the Kronecker delta δ as

$$\mathcal{P}(\omega, z) = W P'(\omega) \delta(z - z_{QW}). \tag{2.86}$$

The boundary conditions for the electrical field are obtained as follows. Inserting equation (2.86) into equation (2.85) and integrating around $z = z_{QW}$ leads to

$$\frac{\partial}{\partial z}\mathcal{E}(z_{QW}+\epsilon) - \frac{\partial}{\partial z}\mathcal{E}(z_{QW}-\epsilon) + \omega^2\frac{n^2}{c^2}\int\limits_{z_{QW}-\epsilon}^{z_{QW}+\epsilon}\mathcal{E}(z)dz = -\omega^2\mu_0 P \quad (2.87)$$

with $P = W\Gamma_\perp P'$ defined for notational convenience.

Outside of the QW region, the electrical field can be written as left and right propagating waves

$$\mathcal{E}(\omega, z) = \begin{cases} L(\omega, z) = L_+ e^{iqz} + L_- e^{-iqz} & \text{for } 0 < z < z_{QW} \\ R(\omega, z) = R_+ e^{iqz} + R_- e^{-iqz} & \text{for } z_{QW} < z < L \end{cases}. \quad (2.88)$$

Inserting equation (2.88) into equation (2.87) and taking the limit $\epsilon \to 0$ gives boundary conditions at the quantum well

$$L(\omega, l) = R(\omega, z_{QW}) = \mathcal{E}(\omega, z_{QW}) \quad (2.89)$$

$$\frac{\partial}{\partial z}R(\omega, z_{QW}) - \frac{\partial}{\partial z}L(\omega, z_{QW}) = -\omega^2\mu_0 P(\omega). \quad (2.90)$$

The boundary conditions at the mirrors read

$$r_1 L_+ t_1^{'} Y = L_+ \quad (2.91)$$

$$r_2 R_+ e^{iqL} = R_- e^{-iqL}. \quad (2.92)$$

Combining equation (2.89) with the boundary conditions at the mirror (2.91)-(2.92) results in

$$R_+ = \frac{e^{-iqz_{QW}}\mathcal{E}}{1 + r_2 e^{2iq(L-z_{QW})}}, \qquad R_- = \frac{r_2 e^{iqz_{QW}}\mathcal{E}}{r_2 + e^{2iq(z_{QW}-L)}}, \quad (2.93)$$

$$L_+ = \frac{r_1 e^{iqz_{QW}}\mathcal{E} + t_1^{'} Y}{1 + r_1 e^{2iqz_{QW}}}, \qquad L_- = \frac{e^{-iqz_{QW}}\mathcal{E} - t_1^{'} Y}{r_1 + e^{-2iqz_{QW}}}. \quad (2.94)$$

Inserting this back into equation (2.90) yields after some algebra

$$F_1(q)\mathcal{E} = i\omega\frac{\mu_0 c}{2n}\Gamma(q)P + F_2(q)Y \quad (2.95)$$

with

$$F_1(q) = 1 - r_1 r_2 e^{2iqL}, \quad (2.96)$$

$$F_2(q) = t_1^{'} e^{iqz_{QW}}\left(1 + r_2 e^{2iq(L-z_{QW})}\right), \quad (2.97)$$

$$\Gamma(q) = \left(1 + r_1 e^{2iqz_{QW}}\right)\left(1 + r_2 e^{2iq(L-z_{QW})}\right). \quad (2.98)$$

Here, Γ is the confinement factor, while F_1 and F_2 are introduced for notational convenience. Further, it is assumed that the modulus of the reflection coefficients does not depend on the frequency

$$r_i(\omega) = \rho_i e^{i\phi_i(\omega)}, \quad \rho_i \in \mathbb{R}. \quad (2.99)$$

To obtain a temporal description, F_1 is expanded around the cavity mode ω_0 that fulfills

$$\begin{aligned} 2q_0L + \phi_1(\omega_0) + \phi_2(\omega_0) &= 2\pi c_0, \quad c_0 \in \mathbb{Z}, && (2.100)\\ 2q_0 z_{QW} + \phi_1(\omega_0) &= 2\pi c_1, \quad c_1 \in \mathbb{Z}, && (2.101)\\ 2q_0(L - z_{QW}) + \phi_2(\omega_0) &= 2\pi c_2, \quad c_2 \in \mathbb{Z}. && (2.102) \end{aligned}$$

The first equation minimizes F_1, and the latter two equations maximize the confinement factor Γ.

The frequency is assumed to be close to the carrier frequency, i. e., $\omega = \omega_0 + \delta\omega$, $\delta\omega \ll 1$. The linearization of F_1 around ω_0 reads

$$F_1(\omega + \delta\omega) \approx F_1(\omega_0) + \left.\frac{\partial F_1}{\partial \omega}\right|_{\omega=\omega_0} \delta\omega. \tag{2.103}$$

Inserting (2.103) into equation (2.95) that was obtained from the boundary conditions yields

$$\left[F_1(\omega_0) + \left.\frac{\partial F_1}{\partial \omega}\right|_{\omega=\omega_0} \delta\omega \right] \mathcal{E} = i\omega_0 \frac{\mu_0 c}{2n} \Gamma(\omega_0) P + F_2(\omega_0) Y. \tag{2.104}$$

Finally, inserting F_1, $\frac{\partial F_1}{\partial \omega}$, F_2 and Γ from equations (2.96)-(2.98) into (2.104) results in the temporal description of the electrical field $\mathcal{E}$

$$\begin{aligned} \tau_c \rho_1 \rho_2 \left(\frac{\partial \mathcal{E}}{\partial t} - i\Delta \right) &= i\omega_0 \frac{\mu_0 c}{2n} (1 + \rho_1)(1 + \rho_2) P - (1 - \rho_1\rho_2)\mathcal{E} \\ &\quad + t_1^{'} e^{iq_0 z_{QW}} (1 + \rho_2) Y, \end{aligned} \tag{2.105}$$

where τ_c is the cavity round-trip time defined as

$$\tau_c = 2\frac{n}{c} L + \frac{\partial}{\partial \omega} \left(\phi_1(\omega_0) + \phi_2(\omega_0) \right). \tag{2.106}$$

The model can be scaled to simplify the notation. For that the photon lifetime κ, scaled detuning δ, polarization prefactor b and injection coupling factor $\tilde{h}$ are defined as

$$\begin{aligned} \kappa &= \frac{1 - \rho_1\rho_2}{\rho_1\rho_2} \tau_c^{-1}, && (2.107)\\ \delta &= \frac{\Delta}{\kappa}, && (2.108)\\ b &= \frac{\omega_0}{2nc} \frac{(1 + \rho_1)(1 + \rho_2)}{1 - \rho_1\rho_2}, && (2.109)\\ \tilde{h} &= t_1^{'} e^{i(\pi n_1 - \phi_1(\omega_0)/2)} \frac{1 + \rho_2}{1 - \rho_1\rho_2}. && (2.110) \end{aligned}$$

Equation (2.105) for the electrical field then becomes

$$\kappa^{-1} \frac{\partial \mathcal{E}}{\partial t} = i\frac{b}{\epsilon_0} P - \mathcal{E} + i\delta\mathcal{E} + \tilde{h} Y. \tag{2.111}$$

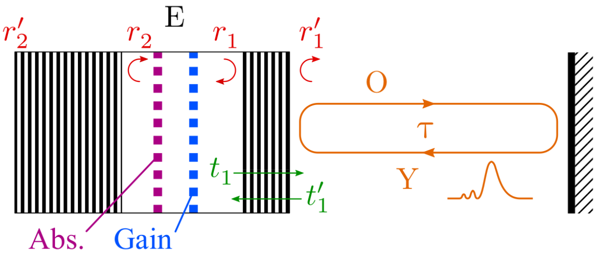

Figure 2.16: A schematic of a mode-locked integrated external-cavity surface-emitting laser (MIXSEL) that contains both a gain (blue) and a saturable absorber medium (purple) coupled to a distant external feedback mirror. E, Y and O denote the intra-cavity field, the injection field and the output field, respectively. Reflection and transmission coefficients are denoted the same as in figure 2.15. Adapted with permission from [32, 33].

Further, $\mathcal{E}$ can be rescaled to be of the same order of magnitude as Y, assuming a lossless distributed Bragg reflector (DBR) at resonance. The input-output relation can be written as

$$O = \xi\mathcal{E} + \beta Y \tag{2.112}$$

with the prefactors

$$\xi = \frac{(-1)^{c_2} t_1 e^{-i\frac{\phi_1}{2}}}{1+\rho_1}, \tag{2.113}$$

$$\beta = r_1' - \frac{t_1 t_1' e^{-i\phi_1}}{1+\rho_1}. \tag{2.114}$$

Using the resonance conditions from equations (2.100)-(2.102) as well as Stokes relations $t't = 1 + r'r$ and $r = -r'$ that hold due to the DBR being assumed to be lossless, the prefactors simplify to

$$\xi = \frac{(-1)^{c_2} t_1}{1+\rho_1}, \tag{2.115}$$

$$\beta = -1. \tag{2.116}$$

Rescaling $E = \xi\mathcal{E}$, $h = \xi\tilde{h}$ and $\chi = \frac{b}{\epsilon}P$, the final model of the injected micro-cavity response with a thin quantum well region is

$$\kappa^{-1}\dot{E} = [i\chi - 1 + i\delta]E + hY, \tag{2.117}$$

$$O = E - Y. \tag{2.118}$$

2.2.1.5 *MIXSEL*

The first setup considered in this thesis is a mode-locked integrated external-cavity surface-emitting laser (MIXSEL) depicted in figure 2.16. It consists of a micro-cavity that contains a gain and saturable absorber medium coupled to a highly reflective feedback mirror.

Taking equation (2.118) for the electrical field E, equation (2.118) for the injection field Y, equation (2.84) for the gain and absorber carriers N_1 and N_2, respectively, and equation (2.82) for the nonlinear susceptibility χ_{nl} gives the model for the MIXSEL as

$$\kappa^{-1}\dot{E} = [i\chi - 1]E + hY, \tag{2.119}$$

$$\chi = -bg_1(\alpha_1 + i)\left(N_1 - N_1^{(tr)}\right) - bg_2(\alpha_2 + i)\left(N_2 - N_2^{(tr)}\right), \tag{2.120}$$

$$Y = O(t - \tau) = \eta[E_\tau - Y_\tau], \tag{2.121}$$

$$\dot{N}_1 = J_1 - \gamma_1 N_1 - \frac{\epsilon_b}{2\hbar} g_1 \left(N_1 - N_1^{(tr)}\right) |E|^2, \tag{2.122}$$

$$\dot{N}_2 = J_2 - \gamma_2 N_2 - \frac{\epsilon_b}{2\hbar} g_2 \left(N_2 - N_2^{(tr)}\right) |E|^2, \tag{2.123}$$

where the coupling efficiency into the micro-cavity is given by $h = (1 + |r_2|)(1 - |r_1|)/(1 + |r_1 r_2|)$.

The notation can further be simplified as follows:

- The carrier densities are shifted by their transparency levels $\tilde{N}_i = bg_i\left(N_i - N_i^{(tr)}\right)$.
- The scaled current $\tilde{J}_i = bg_i\left(\frac{J_i}{\gamma_i} - N_i^{(tr)}\right)$ and the saturation factors $s_i = \frac{\epsilon_b}{2\hbar} g_i$ are introduced.
- Time is rescaled as $\tilde{t} = \kappa t$, $\tilde{\tau} = \kappa\tau$.
- The electrical fields are rescaled as $\tilde{E} = \sqrt{s_1}E$, $\tilde{Y} = \sqrt{s_1}Y$.
- Further, $\tilde{\gamma}_i = \kappa^{-1}\gamma_i$ and $s = \frac{s_2}{s_1} = \frac{g_2}{g_1}$ are introduced.

After these transformations and dropping the tildes for the sake of clarity, the dimensionless scaled form of the MIXSEL reads

$$E = [(1 - i\alpha_1)N_1 + (1 - i\alpha_2)N_2 - 1]E + hY, \tag{2.124}$$

$$N_1 = \gamma_1(J_1 - N_1) - |E|^2 N_1, \tag{2.125}$$

$$N_2 = \gamma_2(J_2 - N_2) - s|E|^2 N_2, \tag{2.126}$$

$$Y(t) = \eta\left[E(t - \tau) - Y(t - \tau)\right]. \tag{2.127}$$

The delay algebraic condition from equation (2.127) incorporates all infinitely many reflections at the external mirror. This can be seen by iteratively reinserting equation (2.127) into itself

$$\begin{aligned}
Y(t) &= \eta\left[E(t - \tau) - Y(t - \tau)\right], \\
Y(t) &= \eta\left[E(t - \tau) - \eta\left[E(t - 2\tau) - Y(t - 2\tau)\right]\right], \\
Y(t) &= \eta\left[E(t - \tau) - \eta\left[E(t - 2\tau) - \eta\left[E(t - 3\tau) - Y(t - 3\tau)\right]\right]\right], \\
&\vdots \\
Y(t) &= \sum_{n=1}^{\infty}(-1)^{n+1}\eta^n E(t - n\tau). \qquad (2.128)
\end{aligned}$$

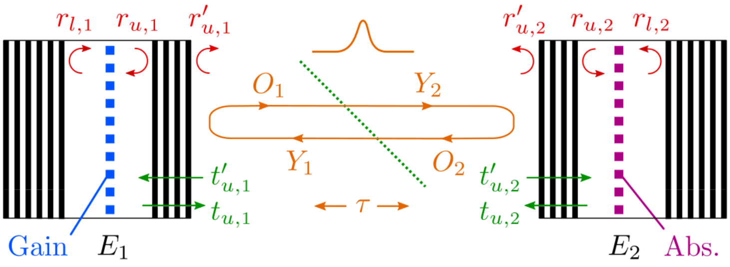

Figure 2.17: A schematic of a vertical cavity surface-emitting laser coupled to a resonant saturable absorber mirror (VCSEL-RSAM). E_i, Y_i and O_i denote the intra-cavity fields, the injection fields and the output fields, respectively, where $i = 1$ indicates the gain mirror and $i = 2$ the absorber mirror. After passing the beam splitter (green dotted line), the output field of one cavity turns into the injection field of the other cavity. Reflection and transmission coefficients are denoted the same as in figure 2.15. Adapted with permission from [32, 34, 35].

For weak feedback $\eta \ll 1$, the series can be truncated after the first order of η considering only single round-trip feedback. The model that results is similar to the Lang-Kobayashi model [120].

All reflections must be considered for strong feedback $\eta \to 1$ because their contributions are of the same order of magnitude. Therefore, the delay algebraic approach without the truncation is more appropriate for laser systems with strong feedback.

2.2.1.6 *VCSEL-RSAM*

The second setup considered in this thesis is a vertical cavity surface-emitting laser coupled to a resonant saturable absorber mirror (VCSEL-RSAM) depicted in figure 2.17.

The response of each cavity is given by equations (2.82), (2.84) and (2.117)

$$\kappa_i^{-1}\dot{E}_i = [i\chi_i - 1 + i\delta_i]E_i + h_i Y_i, \tag{2.129}$$

$$\chi_i = -b_i g_i(\alpha_i + i)\left(N_i - N_i^{(tr)}\right), \tag{2.130}$$

$$\dot{N}_i = J_i - \gamma_i N_i - \frac{\epsilon_b}{2\hbar}\left(N_i - N_i^{(tr)}\right)|E_i|^2, \tag{2.131}$$

where $i = 1$ for the gain cavity and $i = 2$ for the absorption cavity and $\delta_1 = 0$. The injection fields Y_i are the delayed outputs of the respective other cavities after passing the beam splitter

$$Y_1 = \eta O_2(t-\tau) = \eta[E_2(t-\tau) - Y_2(t-\tau)], \tag{2.132}$$

$$Y_2 = \eta O_1(t-\tau) = \eta[E_1(t-\tau) - Y_1(t-\tau)]. \tag{2.133}$$

The notation can be further simplified as follows:

- The carrier densities are shifted by their transparency levels $\tilde{N}_i = bg_i\left(N_i - N_i^{(tr)}\right)$.
- The scaled current $\tilde{J}_i = bg_i\left(\frac{J_i}{\gamma_i} - N_i^{(tr)}\right)$ and the saturation factors $s_i = \frac{\epsilon_b}{2\hbar}g_i$ are introduced.
- Time is rescaled as $\tilde{t} = \kappa t$, $\tilde{\tau} = \kappa\tau$.
- The electrical fields are rescaled as $\tilde{E} = \sqrt{s_1}E$, $\tilde{Y} = \sqrt{s_1}Y$.
- Further, $\tilde{\gamma}_i = \kappa^{-1}\gamma_i$, $s = \frac{s_2}{s_1} = \frac{g_2}{g_1}$ and $\delta = \delta_2$ are introduced.

After these transformations and dropping the tildes for the sake of clarity, the dimensionless scaled form of the VCSEL-RSAM reads

$$\kappa_1^{-1}\dot{E}_1 = \left[(1 - i\alpha_1)N_1 - 1\right]E_1 + h_1Y_1, \tag{2.134}$$

$$\kappa_2^{-1}\dot{E}_2 = \left[(1 - i\alpha_2)N_2 - 1 + i\delta\right]E_2 + h_2Y_2, \tag{2.135}$$

$$\dot{N}_1 = \gamma_1(J_1 - N_1) - |E_1|^2N_1, \tag{2.136}$$

$$\dot{N}_2 = \gamma_2(J_2 - N_2) - s|E_2|^2N_2, \tag{2.137}$$

$$Y_1(t) = \eta\left[E_2(t-\tau) - Y_2(t-\tau)\right], \tag{2.138}$$

$$Y_2(t) = \eta\left[E_1(t-\tau) - Y_1(t-\tau)\right]. \tag{2.139}$$

2.2.2 *Laser States*

2.2.2.1 *Off State*

If a laser is in its off state, no emission takes place, and any electrical field $E_i = Y_i = 0$ equals zero. As a result, the carrier densities converge to their biases, i. e., $N_i = J_i$, respectively.

Usually, the off state is stable until the gain bias J_1 crosses the threshold value J_1^{th} for continuous wave emission.

2.2.2.2 *Continuous Wave*

For continuous wave (CW) solutions, the amplitude and frequency of the electrical field is constant. That means that the electrical field can be written as a single plane wave mode

$$E_i = E_{i,0}e^{-i\omega t + i\phi_{i,0}}, \quad E_{i,0}, \omega, \phi_{i,0} \in \mathbb{R}. \tag{2.140}$$

As the the intensity is constant, and the carriers converge to a value of

$$N_i = \frac{\gamma_i J_i}{\gamma_i + s_i|E_{i,0}|^2} \tag{2.141}$$

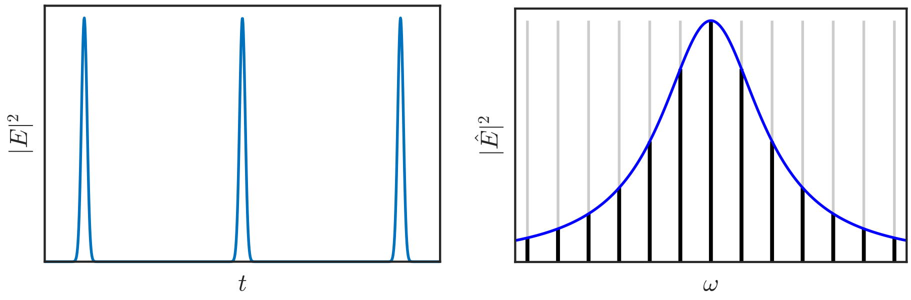

Figure 2.18: Example of mode-locked dynamics in time domain (a) and Fourier space (b). Gray vertical lines, black vertical lines and blue line in panel (b) indicate the frequencies of the different CW modes, their power $|\hat{E}|^2$ and the Fourier transform of a single pulse, respectively.

2.2.2.3 *Mode-Locking*

Mode-locking describes a technique that allows the emission of ultrashort pulses [22–24].

In regular laser emission, the different CW modes oscillate independently with no fixed phase relation. Hence, the output is roughly constant in intensity since the ever changing modal superposition does not create high amplitude fluctuations. If the phase between the modes is fixed so that the modes interfere constructively, the laser's output is instead a train of short and intense pulses.

Mathematically, mode-locking is a superposition of CW modes with appropriate frequencies ω_n and relative phases ϕ_n

$$E = \sum_n E_n e^{-i\omega_n t + i\phi_n}, \quad E_n, \omega_n, \phi_n \in \mathbb{R}. \tag{2.142}$$

The superposition yields a mode-locked solution for appropriate relations between E_n, ω_n and ϕ_n.

In one specific case, the frequencies of the modes are approximately equidistant and can be written as

$$\omega_n = \omega_0 + n\delta\omega, \quad \delta\omega = \frac{2\pi}{T}, \tag{2.143}$$

where T is the round-trip time of the laser. The electrical field amplitudes E_n are assumed to follow a monomodal distribution with bandwidth γ. If $\phi_n = 0$, then all modes interfere constructively. This combination of E_n, ω_n and ϕ_n yields a train of pulses of duration $1/\gamma$, which are T apart (see figure 2.18). The phases ϕ_n can also depend linearly or quadratically on n, resulting in a modified pulse repetition rate T or chirped pulses, respectively [121].

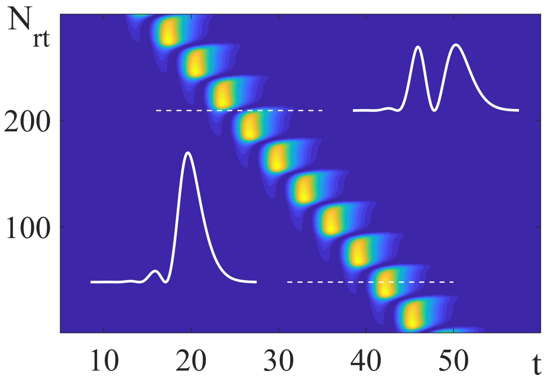

Figure 2.19: Example of the satellite instablility as observed in the MIXSEL (2.124)-(2.127). Adapted with permission from [33].

Experimentally, a distinction is made between active and passive mode-locking [23, 122, 123]. Active modulation of the losses by external forcing, e. g., with an electric optic modulator, is called active mode-locking. On the other hand, if the modulation of the losses is self-induced by the laser system and realized with passive components, like a saturable absorber, one speaks of passive mode-locking.

2.2.2.4 *Temporal Localized States*

If the cavity round-trip time is small, passive mode-locking occurs above the CW threshold. In this case, mode-locked solutions emerge in a supercritical Andronov-Hopf bifurcation from a CW branch [124, 125]. Because the off state is unstable, small perturbations fill the cavity with as many pulses as necessary in order for the average gain level in between pulses to be low enough that the zero field solution is (locally) stable. As the carriers do not have enough time to relax to their biases, the carrier inversion population at the moment a pulse enters the cavity contains information about the previous pulse. Hence, the perturbation of one pulse impacts the consecutive pulse through the interaction with the carriers.

If the cavity round-trip time is large enough the carriers have enough time to relax to their bias. Then mode-locked states can exist below the CW threshold and are bistable with the off solution [125, 126]. Further, consecutive pulses do not interact with each other in this regime because the information about the previous pulse is lost when the carrier reach their bias. Hence, pulses can be moved independently from each other and are individually addressable. In this case, the mode-locked solution becomes a temporal localized state (TLS).

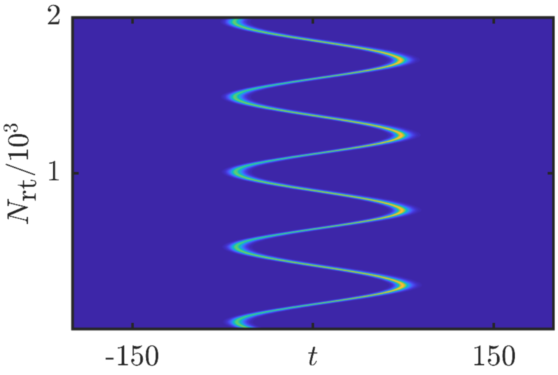

Figure 2.20: Example of a wiggling pulse train as observed in the VCSEL-RSAM (2.134)-(2.139). An oscillating amplitude and position characterize the wiggling motion. Adapted with permission from [34].

2.2.2.5 *Satellite Instability*

The satellite instability is an instability in laser systems which are governed by third order dispersion, where the gain bias is close to the CW threshold. It exists in both the MIXSEL [33] and the VCSEL-RSAM [35].

Informally, a system is governed by third order dispersion when losses and linewidth enhancement factors are small. In this case, a gaussian pulse develops satellites in front of it over time.

As the satellites lead in front of the pulse train, they are amplified before the main pulse. If the amplification is sufficiently high, the satellites can bleach the gain medium. When the gain medium is depleted, the main pulse is not amplified anymore and dies out. Then the biggest satellite becomes the new main pulse and the process repeats (cf. figure 2.19).

Section 4.2 investigates the satellite instability as it appears in the MIXSEL in more detail.

2.2.2.6 *Wiggling*

A wiggling mode-locked state is characterized by an amplitude and position oscillating in time. An example of such a motion is depicted in figure 2.20. In the VCSEL-RSAM system operated in the long delay limit, the wiggling originates from an interplay between third order dispersion and the detuning between the two micro-cavities.

Section 5.3 explains the wiggling instability as it appears in the VCSEL-RSAM in more detail.

2.2.3 *Modal Structure*

The modal structure of a laser system is composed of an ensemble of CW solutions that can be written as

$$E = E_0 e^{-i\omega t}, \tag{2.144}$$

$$Y = Y_0 e^{-i\omega t}, \tag{2.145}$$

where $E_0, Y_0 \in \mathbb{C}$ are complex field amplitudes and $\omega \in \mathbb{R}$ is the CW frequency. For a Fabry–Pérot cavity without coupling, the CW frequencies can easily be determined as $\omega = 2n\pi/T$, $n \in \mathbb{Z}$ with T the round-trip time. However, coupling to an external mirror or cavity considerably complicates the analysis, as we show now.

Inserting the CW ansatz (2.144)-(2.145) into the equation for the general micro-cavity response (2.117) leads to

$$-i\omega E_0 = [i\chi - 1 + i\delta]E_0 + hY_0. \tag{2.146}$$

This means that in the CW case E_0 and Y_0 are linked as

$$E_0 = \frac{h}{1 - i(\chi + \omega + \delta)} Y_0. \tag{2.147}$$

Inserting the constant intensity solution (2.144) into the rate equation for the carriers N, e. g., equation (2.137) with dropped indices, shows that the carriers converge to

$$N = N_0 = \frac{\gamma J}{\gamma + s|E_0|^2}. \tag{2.148}$$

E_0 and Y_0 are fixed by the input-output relation

$$Y = \eta O(t - \tau). \tag{2.149}$$

For a micro-cavity coupled to an external feedback mirror $O = E - Y$ holds and equation (2.149) turns into

$$Y = \eta[E(t - \tau) - Y(t - \tau)]. \tag{2.150}$$

Inserting the CW ansatz (2.144)-(2.145) and the relationship (2.147) between E_0 and Y_0 into the input-output relation (2.150) yields the characteristic equation

$$1 = \eta e^{i\omega\tau} \left[\frac{h}{1 - i(\chi + \omega + \delta)} - 1 \right]. \tag{2.151}$$

The equation (2.151) is transcendental because of the term $e^{i\omega\tau}$ that appears due to the time delay, and cannot be analytically solved. The CW threshold is obtained taking the limit $|E_0| \to 0$, $|Y_0| \to 0$ (χ implicitly depends on E_0 and Y_0). In the long delay limit $\tau \to \infty$, an infinitesimal change in ω results in an arbitrary phase change of $e^{i\omega\tau}$. Therefore, the condition for the phase can be assumed to be fulfilled. Then, only the modulus of equation (2.151) is relevant.

3

METHODS

3.1 DIRECT NUMERICAL SIMULATION

3.1.1 *Leapfrog Integration*

For the direct numerical simulation (DNS) of the DADE systems (2.124)-(2.127) and (2.134)-(2.139) investigated in this thesis, a semi-implicit leapfrog method is used [32, 127]. It gets its name from the fact that the electrical field and the carriers are updated at interleaved time points, and thus the time points from the electrical field leapfrog over the time points from the carriers and vice versa. To derive an updating formula, recall that the laser models discussed in this thesis are of the form

$$\kappa^{-1}\dot{E} = C(N)E + hY, \tag{3.1}$$

$$\dot{N} = \gamma J - U(|E|^2)N, \tag{3.2}$$

$$Y = O(t-\tau). \tag{3.3}$$

Notice that equations (3.1) and (3.2) are linear with the exception of the prefactors $C(N)$ and $U(|E|^2)$. Therefore, an implicit step is solvable if the carriers in $C(N)$ and the electrical field in $U(|E|^2)$ are replaced with their average value. The updating formula for the electrical field (3.1) for a time step of length δt reads

$$\kappa^{-1}\frac{E^{(n+1)} - E^{(n)}}{\delta t} = C^{(n+\frac{1}{2})}\frac{E^{(n+1)} + E^{(n)}}{2} + h\frac{Y^{(n)} + Y^{(n+1)}}{2}. \tag{3.4}$$

Here and in the following, the superscripts indicate the number of the time step and $C^{(n)} = C(N^{(n)})$, $U^{(n)} = U(|E^{(n)}|^2)$ are used as shorthand notations.

As $C^{(n+\frac{1}{2})}$ depends on the value of the carrier at the time step $n + \frac{1}{2}$, the same updating scheme is applied to the carriers (3.2) but shifted by a half step to obtain

$$\frac{N^{(n+\frac{3}{2})} - N^{(n+\frac{1}{2})}}{\delta t} = \gamma J + U^{(n+1)}\frac{N^{(n+\frac{1}{2})} + N^{(n+\frac{3}{2})}}{2}. \tag{3.5}$$

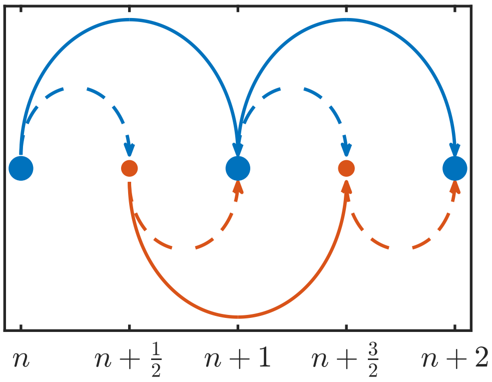

Figure 3.1: A schematic representation of the leapfrog method for direct numerical simulation. The values for the electrical field (blue points) and the carriers (red points) are computed at interleaved points in time. The updating formula for the electrical field "leapfrogs" over the values of the carries and vice versa, giving the method its name.

Solving equations (3.4) and (3.5) for $E^{(n+1)}$ and $N^{(n+\frac{3}{2})}$, respectively, one obtains the final update rule for the systems as

$$E^{(n+1)} = \frac{\left(1+\kappa C^{(n+\frac{1}{2})}\frac{\delta t}{2}\right)E^{(n)} + \kappa h\frac{Y^{(n+1)}+Y^{(n)}}{2}\delta t}{1-\kappa C^{(n+\frac{1}{2})}\frac{\delta t}{2}}, \tag{3.6}$$

$$N^{(n+\frac{3}{2})} = \delta t\gamma J + \frac{\left(1+U^{(n+1)}\frac{\delta t}{2}\right)N^{(n+\frac{1}{2})}}{1-U^{(n+1)}\frac{\delta t}{2}}, \tag{3.7}$$

where the value for $\frac{Y^{(n+1)}+Y^{(n)}}{2}$ in equation (3.6) is determined from the delay algebraic input-output relation (3.3) of the laser system at hand.

Figure 3.1 visualizes how an updating step is performed and how the updating step for the electrical field "leapfrogs" over the step of the carriers and vice versa.

Explicitly, the updating formulas for each of the investigated systems read as follows.

Applying the leapfrog method to the MIXSEL (2.124)-(2.127) yields

$$E^{(n+1)} = \frac{\left(1+C^{(n+\frac{1}{2})}\frac{\delta t}{2}\right)E^{(n)} + h\frac{Y^{(n+1)}+Y^{(n)}}{2}\delta t}{1-C^{(n+\frac{1}{2})}\frac{\delta t}{2}}, \tag{3.8}$$

$$N_1^{(n+\frac{3}{2})} = \gamma_1 J_1\delta t + \frac{\left(1+U_1^{(n+1)}\frac{\delta t}{2}\right)N_1^{(n+\frac{1}{2})}}{1-U_1^{(n+1)}\frac{\delta t}{2}}, \tag{3.9}$$

$$N_2^{(n+\frac{3}{2})} = \gamma_2 J_2\delta t + \frac{\left(1+U_2^{(n+1)}\frac{\delta t}{2}\right)N_2^{(n+\frac{1}{2})}}{1-U_2^{(n+1)}\frac{\delta t}{2}} \tag{3.10}$$

with

$$C^{(n)} = (1 - i\alpha_1)N_1^{(n)} + (1 - i\alpha_2)N_2^{(n)} - 1, \tag{3.11}$$

$$U_1^{(n)} = -(\gamma_1 + |E^{(n)}|^2), \tag{3.12}$$

$$U_2^{(n)} = -(\gamma_2 + s|E^{(n)}|^2). \tag{3.13}$$

The value of the injection field is given by

$$Y^{(n)} = \eta[E^{(n-M)} - Y^{(n-M)}], \quad M = \frac{\tau}{\delta t}. \tag{3.14}$$

The updating formula for the VECSEL-RSAM (2.134)-(2.139) reads

$$E_1^{(n+1)} = \frac{\left(1 + \kappa_1 C_1^{(n+\frac{1}{2})}\frac{\delta t}{2}\right) E_1^{(n)} + \kappa_1 h \frac{Y_1^{(n+1)} + Y_1^{(n)}}{2}\delta t}{1 - \kappa_1 C_1^{(n+\frac{1}{2})}\frac{\delta t}{2}}, \tag{3.15}$$

$$E_2^{(n+1)} = \frac{\left(1 + \kappa_2 C_2^{(n+\frac{1}{2})}\frac{\delta t}{2}\right) E_2^{(n)} + \kappa_2 h \frac{Y_2^{(n+1)} + Y_2^{(n)}}{2}\delta t}{1 - \kappa_2 C_2^{(n+\frac{1}{2})}\frac{\delta t}{2}}, \tag{3.16}$$

$$N_1^{(n+\frac{3}{2})} = \gamma_1 J_1 \delta t + \frac{\left(1 + U_1^{(n+1)}\frac{\delta t}{2}\right) N_1^{(n+\frac{1}{2})}}{1 - U_1^{(n+1)}\frac{\delta t}{2}}, \tag{3.17}$$

$$N_2^{(n+\frac{3}{2})} = \gamma_2 J_2 \delta t + \frac{\left(1 + U_2^{(n+1)}\frac{\delta t}{2}\right) N_2^{(n+\frac{1}{2})}}{1 - U_2^{(n+1)}\frac{\delta t}{2}} \tag{3.18}$$

with

$$C_1^{(n)} = (1 - i\alpha_1)N_1^{(n)} - 1, \tag{3.19}$$

$$C_2^{(n)} = (1 - i\alpha_2)N_2^{(n)} - 1 + i\delta, \tag{3.20}$$

$$U_1^{(n)} = -(\gamma_1 + |E^{(n)}|^2), \tag{3.21}$$

$$U_2^{(n)} = -(\gamma_2 + s|E^{(n)}|^2). \tag{3.22}$$

The value of the injection fields is given by

$$Y_1^{(n)} = \eta[E_2^{(n-M)} - Y_2^{(n-M)}], \tag{3.23}$$

$$Y_2^{(n)} = \eta[E_1^{(n-M)} - Y_1^{(n-M)}], \quad M = \frac{\tau}{\delta t}. \tag{3.24}$$

3.1.2 *Split-Step Method*

The split-step method is used for integrating nonlinear partial differential equations that can be written as

$$\frac{dE}{dt} = \mathcal{L}E + \mathcal{N}E, \tag{3.25}$$

where $\mathcal{L}$ and $\mathcal{N}$ are linear and nonlinear operators, respectively [128–130]. The idea of the split-step method is to solve the purely linear and purely nonlinear equation

$$\frac{dE}{dt} = \mathcal{N}E, \tag{3.26}$$

$$\frac{dE}{dt} = \mathcal{L}E \tag{3.27}$$

in a given sequential order, using the solution of one subproblem as the initial condition of the next one.

Formally, the solution of equation (3.25) is given by

$$E(t + \delta t) = e^{\delta t(\mathcal{L}+\mathcal{N})}E(t). \tag{3.28}$$

The simplest case is the first order splitting, where the linear and nonlinear operators are solved independently after another, leading to

$$E(t + \delta t) \approx e^{\delta t\mathcal{N}}e^{\delta t\mathcal{L}}E(t), \tag{3.29}$$

which is exact, if and only if $\mathcal{N}$ and $\mathcal{L}$ commute. This approach is equivalent to first exclusively solving the linear part (3.27) and using the obtained solution as an initial condition to solve the nonlinear part (3.26).

Other splits of $e^{\delta t(\mathcal{L}+\mathcal{N})}$ are possible to increase the accuracy of the solution. In this thesis, a second order split-step method is employed, which means that the solution is approximated as

$$E(t + \delta t) \approx e^{\frac{\delta t}{2}\mathcal{N}}e^{\delta t\mathcal{L}}e^{\frac{\delta t}{2}\mathcal{N}}E(t), \tag{3.30}$$

i. e., a half step of the nonlinear part (3.26) is solved, followed by a whole step of the linear part (3.27), followed again by a half step of the nonlinear part (3.26).

Concretely, the first half step of the nonlinear part is solved with an explicit Euler step [131], the whole step of the linear part is solved using the spectral method [132], and the second half step of the nonlinear part is solved using an implicit Euler step [131]. These steps leads to the updating formula

$$E^{n+\frac{1}{2}} = E^n + \frac{\delta t}{2}\mathcal{N}^n E^n, \tag{3.31}$$

$$\tilde{E}^{n+\frac{1}{2}} = \mathcal{F}^{-1}[e^{\delta t\mathcal{F}[\mathcal{L}]}\mathcal{F}[E^{n+\frac{1}{2}}]], \tag{3.32}$$

$$E^{n+1} = \frac{\tilde{E}^{n+\frac{1}{2}}}{1 - \frac{\delta t}{2}\mathcal{N}^n E^n}, \tag{3.33}$$

where $\mathcal{F}$ and $\mathcal{F}^{-1}$ denote the Fourier transform and its inverse, respectively.

3.1.3 *Functional Mapping*

One solution type in laser systems is a pulse train of temporal localized structures (see section 2.2.2.4). The pulse train is characterized by having a fast stage, where the electrical field and the carrier change rapidly, and a slow stage, where the electrical field intensity is approximately constant and the carriers recover almost exponentially.

This observation saves computational effort by only simulating the fast stage, while the slow stage is replaced with an analytical approximation. This concept is called the functional mapping method [133].

Figure 3.2 illustrates the functional mapping method, showing the integration of two fast stages in the left and right panels and the analytical approximation of the slow stage between the two fast stages in the middle panels.

The fast stage is integrated with the leapfrog method (see section 3.1.1). The system's variables in the nth fast stage are defined as

$$E^n(t) = E(T^n + t), \tag{3.34}$$

$$N^n(t) = N(T^n + t), \tag{3.35}$$

where $t \in [0, T_b]$, T_b is the time length of the fast stage, also referred to as box length, and T^n is the beginning of the nth fast stage. Hence, $(T^{n+1} - T^n)$ is the nth cavity round-trip time.

It is assumed that the electrical field intensity $|E|^2$ is a constant for the slow phase. For the MIXSEL and VCSEL-RSAM, this constant is zero. For constant electrical field intensity, the differential equation for the carriers (2.137) (with subindices dropped) has the general solution

$$N(t) = \frac{\gamma J}{\gamma + s|E|^2} + e^{-(\gamma+s|E|^2)t}c, \tag{3.36}$$

where c is a constant determined by the initial condition. The carriers and the electrical field at the end of the last round-trip can therefore be connected with the beginning of the next round-trip as

$$E^{n+1}(0) = |E^n(T_b)|e^{i(\omega(T^{n+1}-T^n-T_b)+\phi^n(T_b))}, \tag{3.37}$$

$$N^{n+1}(0) = N^n(T_b)\zeta + (1-\zeta)J, \quad \zeta = e^{-(\gamma+s|E|^2)(T^{n+1}-T^n-T_b)}, \tag{3.38}$$

where $\phi^n(T_b)$ is the phase of E^n at the end of the nth fast stage, ω is the CW frequency of E^n, and ζ is the memory time effect for carriers.

Like this, the system's variables at the next round-trip can be written as an iterative map

$$E^{n+1} = f(E^n, N^n), \tag{3.39}$$

$$N^{n+1} = f(E^n, N^n) \tag{3.40}$$

giving the method its name.

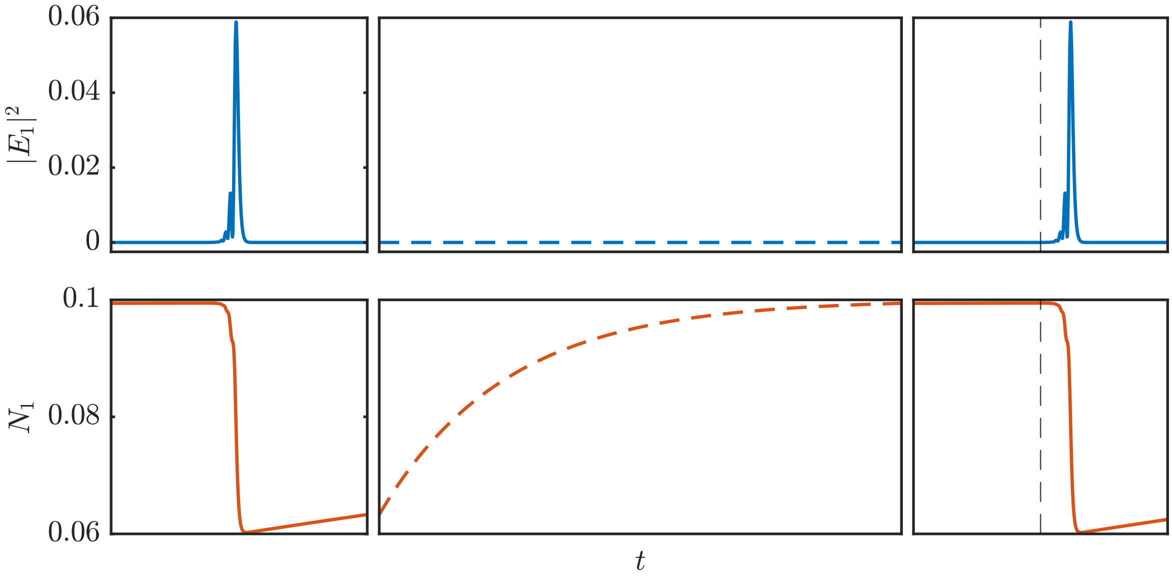

Figure 3.2: Illustration of the functional mapping method. The left and right columns: Integration of the fast stage using the semi-implicit leapfrog method. Center column: Analytical approximation of the slow stage that is not integrated. Top and bottom row: Intensity of the electrical field and the value of the gain carriers, respectively. The dashed vertical line in the right column marks the previous pulse position.

Due to causality, TLS solutions have a period slightly larger than the round-trip time, leading to the pulse slowly drifting out of the box (cf. figure 3.2). The drift is compensated by shifting the box after each round-trip, centering the maximum pulse intensity and padding with the electrical field intensity value during the slow phase.

The functional mapping method shrinks the computational effort for solutions with period T by T_b/T. Hence, the functional mapping method is particularly well suited for the long cavity regime because there $T_b \ll T$ holds.

Explicitly, the reconnection formulas for each of the investigated systems read as follows.

For the MIXSEL (2.124)-(2.127), the reconnection between two fast stages reads

$$E^{n+1}(0) = 0, \tag{3.41}$$

$$N_1^{n+1}(0) = N_1^n(T_b)\zeta + (1-\zeta)J_1, \quad \zeta = e^{-(T^{n+1}-T^n-T_b)\gamma_1}, \tag{3.42}$$

$$N_2^{n+1}(0) = N_2^n(T_b)\zeta + (1-\zeta)J_2, \quad \zeta = e^{-(T^{n+1}-T^n-T_b)\gamma_2}. \tag{3.43}$$

$Y^{n+1}(0)$ is determined from the delay algebraic condition (2.127) from $E^n(0)$ and $Y^n(0)$ as

$$Y^{n+1}(0) = \eta[E^n(0) - Y^n(0)]. \tag{3.44}$$

For the VCSEL-RSAM (2.134)-(2.139), the reconnection between two fast stages is given by

$$E_1^{n+1}(0) = 0, \tag{3.45}$$

$$E_2^{n+1}(0) = 0, \tag{3.46}$$

$$N_1^{n+1}(0) = N_1^n(T_b)\zeta_1 + (1 - \zeta_1)J_1, \quad \zeta_1 = e^{-(T_{n+1} - T_n - T_b)\gamma_1}, \tag{3.47}$$

$$N_2^{n+1}(0) = N_2^n(T_b)\zeta_2 + (1 - \zeta_2)J_2, \quad \zeta_2 = e^{-(T_{n+1} - T_n - T_b)\gamma_2}. \tag{3.48}$$

$Y_1^{n+1}(0)$ and $Y_2^{n+1}(0)$ are determined from the delay algebraic conditions (2.138)-(2.139) from $E_1^n(0)$, $E_2^n(0)$, $Y_1^n(0)$ and $Y_2^n(0)$ as

$$Y_1^{n+1}(0) = \eta[E_2^n(0) - Y_2^n(0)], \tag{3.49}$$

$$Y_2^{n+1}(0) = \eta[E_1^n(0) - Y_1^n(0)]. \tag{3.50}$$

3.2 BIFURCATION ANALYSIS

Direct numerical simulation allows observing the dynamical behavior on an attractor, e. g., a stable steady state or a stable limit cycle. However, DNS cannot observe unstable structures in the phase space, which might significantly impact the dynamics. Therefore, to get a more comprehensive picture of the structure of the phase space, a bifurcation analysis can be performed, which allows following stable and unstable solutions through the control parameter space.

The bifurcation analysis is performed with the MATLAB [134] continuation package DDE-BIFTOOL [135, 136]. Until recently, it was impossible to perform a bifurcation analysis of DADEs using DDE-BIFTOOL. One contribution of this thesis is the implementation of the methods that enable the bifurcation analysis of DADEs [74]. Further, the demos in appendix A show how to use the extension for DADEs.

3.2.1 *Steady States*

Steady states $x(t) = x(t - \tau) = x^*$ are given as the zeros of the equation

$$0 = f(x^*, x^*), \tag{3.51}$$

where $f(x(t), x(t - \tau))$ is the right-hand side of the delayed dynamical system (2.48).

Numerically, equation (3.51) can be solved iteratively using the Newton-Raphson method [137–139]. The starting point of the method is an initial guess x^0. The value of the next iteration is found by approximating f with its tangent and using the tangent's zero as the value for the next iteration. The iteration is stopped once $||f(x^n, x^n)||$ is sufficiently close to zero.

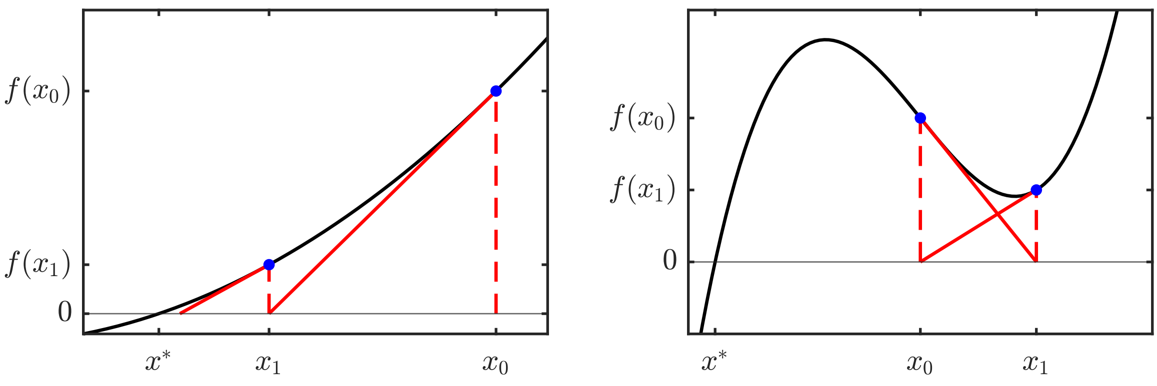

(a) Converging example (b) Failing example

Figure 3.3: A schematic of the Newton-Raphson method. The starting point of the method is an initial guess x_0. A zero of a function f is found by iteratively approximating f with its tangent and using the tangent's zero as the value for the next iteration. Black line: Value of the function f. Blue dots: Value of f at one of the iteration points. Solid red line: Tangent through the iteration points. Dashed red lines guide the eye from the zero of the current iteration's tangent to the next function value.

The formula of the tangent $t(x)$ through x^n is given by

$$t(x) = f(x^n, x^n) + J(x^n)(x - x^n), \tag{3.52}$$

where $J(x^n)$ is the Jacobi-matrix of f. Solving $t(x^{n+1}) = 0$ for x^{n+1} results in the updating formula for the Newton-Raphson method as

$$x^{n+1} = x^n - J^{-1}(x^n)f(x^n, x^n), \tag{3.53}$$

where $J^{-1}(x^n)$ is the inverse of the Jacobi-matrix of f.

Figure 3.3 (a) depicts how the Newton-Raphson finds the zero of an example function. As the initial guess is close enough to the zero of f, the residuum $||f(x^n)||$ decreases with every iteration until it is sufficiently close to zero.

The Newton-Raphson method is not guaranteed to converge. Because f is approximated locally around the current iteration value, the initial guess x_0 has to be sufficiently close to the zero of f to converge. An example where the Newton-Raphson method fails is depicted in figure 3.3 (b). Instead of converging to the zero of f, the iteration is caught in a 2-cycle.

3.2.2 *Linear Stability Analysis*

Eigenvalues of steady states of DDSs and especially DADEs can be numerically approximated by a pseudo-spectral method [140, 141] which discretizes the infinite-dimensional state into a finite-dimensional mesh approximation.

By defining a mesh

$$\Omega_N = \{\theta_i | i = 1, ..., N+1 \wedge -\tau \leq \theta_1 < \theta_j < \theta_{j+1} < \theta_{N+1} = 0\} \quad (3.54)$$

of $N+1$ distinct points in $[-\tau, 0]$, the state is discretized by only considering state values at the mesh points as

$$x_N = \begin{pmatrix} x(t+\theta_1) \\ \vdots \\ x(t+\theta_{N+1}) \end{pmatrix}. \quad (3.55)$$

The eigenvalue problem given by equation (2.54) can then be approximated by

$$|\mathcal{A}_N - \lambda M_N| = 0. \quad (3.56)$$

M_N and $\mathcal{A}_N$ are given as

$$M_N = \begin{pmatrix} I_{nN\times nN} & 0 \\ 0 & M \end{pmatrix} \quad (3.57)$$

and

$$(\mathcal{A}_N x_N)_i = (\mathcal{P} x_N)'(\theta_i), \quad i = 1, \dots, N \quad (3.58)$$

$$(\mathcal{A}_N x_N)_{N+1} = \mathcal{L}(\mathcal{P} x_N), \quad (3.59)$$

where $\mathcal{P} x_N$ is the polynomial interpolation of x_N and $\mathcal{L}$ is the linear operator that belongs to the DDS (2.48).

3.2.3 *Path Continuation*

The process of following a solution through the control parameter space is called path continuation.

In general, path continuation is as a repetition of two steps: The prediction of the next point with varied control and its correction.

When starting from a single point, its tangent is used to predict the second point. After that, a secant prediction through the last two points predicts the next point [136]. As a corrector, the Newton-Raphson method is used (see section 3.2.1).

However, folding solution curves complicate the continuation process. While there might be a solution at a parameter value μ in this case, it stops existing for $\mu + \delta\mu$. Keeping the parameter's value μ fixed leads to the continuation failing if a solution curve folds.

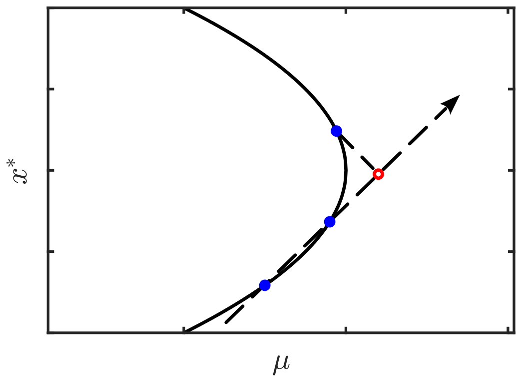

Figure 3.4: A pseudo-arclength continuation following a folding solution. In order to continue folding curves, the parameter μ is not kept fixed but is allowed to vary freely. Instead, the correction is required to lie orthogonal to the prediction. Solid black line: Solution curve. Empty red dot: Predicted point. Solid blue dots: Corrected points. Dashed lines: Secant through the last two points for prediction and the orthogonal line on which the correction is allowed to lie.

Pseudo-arclength continuation [142] circumvents this challenge. Here, the parameter value is not fixed but can vary freely. Instead, an additional condition requires that the correction lies orthogonal to the prediction which allows continuing curves around a fold. Figure 3.4 shows a pseudo-arclength following a folding solution.

3.2.4 *Determining Systems*

In addition to steady states, other types of solutions can be continued by extending the original dynamical system appropriately.

Fold and Andronov-Hopf bifurcations (see sections 2.1.6.1 and 2.1.6.3, respectively) are continued by solving the extended dynamical system

$$f(x^*, x^*; \mu) = 0, \tag{3.60}$$

$$\Delta(\lambda, \mu, x^*)v = 0, \tag{3.61}$$

$$c^T v - 1 = 0, \tag{3.62}$$

where f is the right-hand side from equation (2.48) with explicit depence on the control parameter μ, Δ is the characteristic matrix, λ and v are an eigenvalue and -vector, respectively, and c is a normalization vector.

Equation (3.60) ensures that the corrected point is a steady state of the original dynamical system. Equation (3.61) results in λ being an eigenvalue of the system with eigenvector v, which is normalized by equation (3.62).

For a fold bifurcation the λ is zero and the v is real, while for an Andronov-Hopf bifurcation v is complex and $\lambda = \pm i\omega$, $\omega \in \mathbb{R}$.

Periodic orbits are continued by solving the extended dynamical system

$$M\dot{x}(t) = f(x(t), x(t-\tau)), \tag{3.63}$$

$$x(t) = x(t+T), \tag{3.64}$$

$$\theta(x,t) = 0, \tag{3.65}$$

where $\theta(x,t)$ is the phase of x at time t.

While equation (3.63) ensures that the time trace of the periodic orbit fulfills the right-hand side of the dynamic system, equation (3.64) ensures that the time trace is periodic with period T. Further, a phase condition is applied with equation (3.65) to single out one of the infinitely many equivalent periodic orbits obtained by shifting the profile cyclically [136, 143].

Similarly, higher-order bifurcations, e. g., bifurcations of periodic orbits can be followed with a similar approach. For more details on the extended systems for the torus bifurcation, fold of periodic orbits and period-doubling, see [144].

3.2.5 *Co-Rotating Frame*

The system equations investigated in this thesis exhibit a phase symmetry that can be exploited to simplify the analysis. Because the electrical fields are complex and there is no reference phase, shifting the phase of an initial condition results in the same dynamics, albeit the phase of the solution is shifted by the same amount as the initial condition.

The right-hand side of a delayed dynamical system (2.48) is called phase invariant if it fulfills

$$f(e^{A\phi}x(t), e^{A\phi}x(t-\tau)) = e^{A\phi}f(x(t), x(t-\tau)) \tag{3.66}$$

for one specific generator matrix A and all value of the phase $\phi \in \mathbb{R}$.

Making the co-rotating ansatz

$$x(t) = e^{A\omega t}\chi(t), \quad \omega \in \mathbb{R} \tag{3.67}$$

the dynamical system (2.48) is rewritten in terms of the co-rotating variable $\chi(t)$ instead of $x(t)$ as

$$M\dot{\chi} = -MA\omega\chi(t) + f(\chi, \chi(t-\tau)). \tag{3.68}$$

In this way, continuous wave solutions

$$x(t) = e^{A\omega t}x_0, \quad x_0 \in \mathbb{R}^d \tag{3.69}$$

become stationary $\chi(t) = x_0$ and modulated wave solutions

$$x(t) = e^{A(\omega t+\Theta)} x_{per}(t), \quad x_{per}(t) = x_{per}(t-T), \quad \Theta \in \mathbb{R} \tag{3.70}$$

become periodic solutions $\chi(t) = x_{per}(t)$.

The new parameter ω is a free parameter in the continuation fixed by an appropriate phase condition [136].

3.2.6 *Starting Solutions*

Starting solutions for the continuation can be obtained from direct numerical simulation. DNS is a convenient choice for pulsed solutions because it might be complicated to continue a known analytical CW steady state to the solution of interest.

In contrast to bifurcation analysis, DNS allows the exploration of regimes without knowing a stable solution beforehand. Converting the results to a solution in the bifurcation software allows following the solution to an unstable regime, which is impossible with DNS. On the other hand, DNS verifies the result obtained from bifurcation analysis in the stable regimes and allows observing transient behavior, chaos, and modulated periodic orbits emerging from a torus bifurcation.

The frequency of the co-rotating frame (see section 3.2.5) is estimated from a time trace as

$$\omega \approx \frac{\phi(t_{end}) - \phi(t_{start})}{t_{end} - t_{start}}, \tag{3.71}$$

where ϕ is the angle of the complex field E_1 and t_{end} and t_{start} are the time of the end and the beginning of the profile, respectively.

In order to save computational effort, the number of intervals and the polynomial degree is chosen to minimize the dimension of the resulting system. Combinations of the number of intervals and the polynomial degree are tried until one of them successfully corrects.

3.3 MULTI-SCALE ANALYSIS

Multi-scale analysis constructs a uniformly valid approximation for dynamical systems that evolve on different time scales [145]. This thesis uses the multi-scale method to derive normal form PDEs from DADE laser models close to the CW threshold. The time variable t is split into multiple time scales $T_1, T_2, \ldots, T_n$, which evolve on different orders of magnitude, and are treated as if they were independent.

In detail, a nth order multi-scale analysis consists of the following steps:

1. A smallness parameter ϵ is defined that separates the different time scales.

2. Using the smallness parameter, the different time scales can be separated as

$$T_i = \epsilon^i t. \tag{3.72}$$

3. The system's variables are redefined by making the multi-scale ansatz

$$x(t) = \sum_i \epsilon^i x_i(T_0, T_1, \dots, T_n), \tag{3.73}$$

where $x_i(T_0, T_1, \dots, T_n)$ is the ith order solution of $x(t)$.

4. The time variable t is eliminated from the system's equations, and the separated time scales are introduced. For that, the time derivatives and time delays are rewritten using the chain rule

$$\frac{\mathrm{d}}{\mathrm{d}t} = \sum_i \frac{\partial T_i}{\partial t}\frac{\partial}{\partial T_i} = \sum_i \epsilon^i \frac{\partial}{\partial T_i}, \tag{3.74}$$

$$\begin{aligned} x(t-\tau) &= x(T_0 - \tau, T_1 - \epsilon\tau, \dots, T_n - \epsilon^n \tau) \\ &= \sum_i \mathcal{L}_i \epsilon^i x(t-\tau, T_1, \dots, T_n) \end{aligned} \tag{3.75}$$

with $\mathcal{L}_i$ obtained from the Taylor expansion of $x(T_0 - \tau, T_1 - \epsilon\tau, \dots, T_n - \epsilon^n\tau)$ around $(T_0 - \tau, T_1, \dots, T_n)$.

5. Inserting equations (3.73)-(3.75) into the dynamical system (2.48) yields a polynomial equation in ϵ. All terms are sorted according to the power of ϵ to obtain a hierarchy of equations for each order of ϵ. The equation for each order is a linear algebraic inhomogenous system that can be written as

$$\mathcal{S}x = b, \tag{3.76}$$

where $\mathcal{S}$ is a non-invertible linear operator, x is the independent variable and b is an inhomogeneity. Because $\mathcal{S}$ is non-invertible, the solution equation (3.76) cannot simply be written as $x = \mathcal{S}^{-1}b$ and the existence of a solution has to be ensured by a solvability condition.

6. Starting at the zeroth order of ϵ, a solvability condition is obtained for each order through Fredholm's alternative [146, 147]. It states that the system (3.76) has a solution if and only if for all y with $\mathcal{S}^\dagger y = 0$ it holds that $y^\dagger b = 0$, where † indicates the adjoint. In other words: An inhomogeneous linear equation has a solution if and only if the kernel of the adjoint is orthogonal to the inhomogeneity. The result are solvability conditions relating the different time scales T_i to each other.

7. Finally, the uniformly valid PDE approximation is obtained by reconstructing the time scale

$$\frac{\partial x}{\partial \xi} = \left(\frac{d}{dt} - \frac{\partial}{\partial T_0}\right) x, \tag{3.77}$$

where the term $-\partial_{T_0} x$ transforms a solution with period T into a slowly drifting steady state from one round-trip to the next one. The right side of equation (3.77) is made to depend only on the time T_0 by inserting the relations between the time scales as obtained from Fredholm's alternative.

3.3.1 *Scaling Time*

For delayed dynamical systems, if the period T is slightly larger than the delay time τ, it is possible to incorporate the slow evolution on the time scale T_1 by scaling the zeroth order time scale T_0 with the frequency of the periodic solution $\omega = 2\pi/T$, thereby eliminating T_1 from the derivation. The modified ansatz reads

$$T_0 = \omega t, \quad T_1 = 0, \quad T_i = \epsilon^i t, \quad i \geq 2, \tag{3.78}$$

$$\omega = 1 + \sum_{i\geq 1} \epsilon^i \omega_i. \tag{3.79}$$

Equations (3.78)-(3.79) propagate to equations (3.73)-(3.75), yielding

$$\frac{d}{dt} = \sum_{i=0}^{n} \epsilon^i \mathcal{T}_i, \tag{3.80}$$

$$E(t) = \sum_{i=0}^{n} \epsilon^i E_i(T_0, T_2, \ldots, T_n), \tag{3.81}$$

$$E(t-\tau) = \sum_{i=0}^{n} \epsilon^i \mathcal{L}_i E(T_0 - \tau, T_2, \ldots, T_n) = \sum_{i=0}^{n}\sum_{j=0}^{i} \epsilon^i \mathcal{L}_j E_{i-j}^{\tau}, \tag{3.82}$$

where $E_i^\tau = E_i(T_0 - \tau, T_2, \ldots, T_n)$ is used as a shorthand.

The operators $\mathcal{T}_i$ are obtained by using the chain rule using the new time scale and inserting the value of ω from equation (3.79). Similarly, the operators $\mathcal{L}_i$ are obtained from the Taylor expansion of $E(t-\tau) = E(T_0 - \omega\tau, T_2 - \epsilon^2\tau, \ldots, T_n - \epsilon^n \tau)$ around $(T_0 - \tau, T_2, \ldots, T_n)$. Explicitly, the resulting operators up to third order read

$$\mathcal{T}_0 = \partial_0, \quad \mathcal{T}_1 = \omega_1 \partial_0, \quad \mathcal{T}_2 = \omega_2 \partial_0 + \partial_2, \quad \mathcal{T}_3 = \omega_3 \partial_0 + \partial_3, \tag{3.83}$$

$$\mathcal{L}_0 = 1, \tag{3.84}$$

$$\mathcal{L}_1 = -\omega_1 \partial_0, \tag{3.85}$$

$$\mathcal{L}_2 = -\omega_2 \partial_0 + \frac{\omega_1^2}{2}\partial_0^2 - \partial_2, \tag{3.86}$$

$$\mathcal{L}_3 = -\omega_3 \partial_0 - \frac{\omega_1^3}{6}\partial_0^3 + \omega_1\omega_2\partial_0^2 + \omega_1 \partial_0 \partial_2 - \partial_3. \tag{3.87}$$

3.3.2 *Example with Time-Delay*

An example of how to apply the multi-scale analysis for a second order approximation is the linear equation

$$\dot{E} = -E + E(t-\tau), \quad \tau \gg 1. \tag{3.88}$$

After rescaling the time $t \to t/\tau$, the smallness parameter $\epsilon = 1/\tau$ is introduced to equation (3.88)

$$\epsilon \frac{d}{dt} E = -E + E(t-1). \tag{3.89}$$

Inserting the ansatzes for $\frac{d}{dt}$, $E(t)$ and $E(t-1)$ from equations (3.80), (3.81) and (3.82), respectively, yields

$$\begin{aligned} \epsilon\left(\mathcal{T}_0 + \epsilon\mathcal{T}_1 + \epsilon^2\mathcal{T}_2\right)\left(E_0 + \epsilon E_1 + \epsilon^2 E_2\right) = &-\left(E_0 + \epsilon E_1 + \epsilon^2 E_2\right) \\ &+ [\mathcal{L}_0 E_0^\tau + \epsilon(\mathcal{L}_0 E_1^\tau + \mathcal{L}_1 E_0^\tau) \\ &+ \epsilon^2(\mathcal{L}_0 E_2^\tau + \mathcal{L}_1 E_1^\tau + \mathcal{L}_2 E_0^\tau)], \end{aligned} \tag{3.90}$$

where $E_i = E_i(T_0, T_2)$ and $E_i^\tau = E_i(T_0 - 1, T_2)$.

Next, equation (3.90) is sorted for powers of ϵ and the orders are solved after each other starting from zeroth order.

The equation for ϵ^0 reads

$$0 = -E_0 + \mathcal{L}_0 E_0^\tau. \tag{3.91}$$

Inserting $\mathcal{L}_0 = 1$ leads to

$$0 = -E_0 + E_0^\tau, \tag{3.92}$$

which shows that E_0 has period one.

The equation for ϵ^1 reads

$$\mathcal{T}_0 E_0 = -E_1 + \mathcal{L}_0 E_1^\tau + \mathcal{L}_1 E_0^\tau. \tag{3.93}$$

Expanding $\mathcal{T}_0$, $\mathcal{L}_0$ and $\mathcal{L}_1$ from equations (3.83)-(3.85) results in

$$\partial_0 E_0 = -E_1 - \omega_1 \partial_0 E_0 + E_1(t_0 - 1) \tag{3.94}$$

$$\implies E_1 - E_1(t_0 - 1) = -(1 + \omega_1)\partial_0 E_0. \tag{3.95}$$

After choosing $\omega_1 = -1$, the right side vanishes and E_1 has period one.

The equation for ϵ^2 reads

$$\mathcal{T}_1 E_0 + \mathcal{T}_0 E_1 = -E_2 + (\mathcal{L}_0 E_2^\tau + \mathcal{L}_1 E_1^\tau + \mathcal{L}_2 E_0^\tau) \tag{3.96}$$

$$\implies E_2 - E_2(t-1) = (1 - \omega_2)\partial_0 E_0 + \frac{1}{2}\partial_0^2 E_0 - \partial_2 E_0, \tag{3.97}$$

where equations (3.83)-(3.86) are were used to substitute $\mathcal{T}_i$ and $\mathcal{L}_i$. After choosing $\omega_2 = 1$, the solvability condition is

$$\partial_2 E_0 = \frac{1}{2}\partial_0^2 E_0. \tag{3.98}$$

Rebuilding the time derivative according to equation (3.77) gives

$$\frac{\partial E_0}{\partial \xi} = \omega_1 \partial_0 + \epsilon^2 \partial_2. \tag{3.99}$$

Finally, inserting $\omega_1 = -1$ and equation (3.98) into equation (3.99) results in

$$\partial_\xi E = -\partial_0 E + \frac{1}{2}\partial_0^2 E \tag{3.100}$$

as the multi-scale approximation of equation (3.88).

3.3.3 *Example without Time Scaling*

Consider the same example without time scaling, i. e., $\omega_i = 0$, to see the effects of the scaling on the derivation.

Inserting the regular ansatz (3.73)-(3.75) into equation (3.88) results in

$$\begin{aligned} \epsilon\left(\partial_0 + \epsilon\partial_1 + \epsilon^2\partial_2\right)\left(E_0 + \epsilon E_1 + \epsilon^2 E_2\right) = &- \left(E_0 + \epsilon E_1 + \epsilon^2 E_2\right) \\ &+ [E_0^\tau + \epsilon(E_1^\tau - \partial_1 E_0^\tau) \\ &+ \epsilon^2(E_2^\tau - \partial_1 E_1^\tau + \left(\frac{1}{2}\partial_1^2 - \partial_2\right) E_0^\tau)], \end{aligned} \tag{3.101}$$

where $E_i = E_i(T_0, T_1, T_2)$ and $E_i^\tau = E_i(T_0 - \tau, T_1, T_2)$.

The solvability condition for the zeroth order remains unchanged, i. e.,

$$0 = -E_0 + E_0^\tau, \tag{3.102}$$

which shows that E_0 has period one.

The equation for ϵ^1 reads

$$\partial_0 E_0 = -E_1 + E_1^\tau - \partial_1 E_0 \tag{3.103}$$

$$\implies E_1 - E_1^\tau = (\partial_0 + \partial_1)E_0. \tag{3.104}$$

The solvability condition for equation (3.104) is

$$\partial_1 = -\partial_0, \tag{3.105}$$

which when fulfilled shows that E_1 has period one.

The equation for ϵ^2 reads

$$\begin{aligned} \partial_0 E_1 + \partial_1 E_0 = &- E_2 + E_2^\tau \\ &- \partial_1 E_1^\tau \\ &+ \left(\frac{1}{2}\partial_1^2 - \partial_2\right) E_0^\tau . \end{aligned} \tag{3.106}$$

Using the fact that E_0 and E_1 are period one allows rearranging equation (3.106) to

$$E_2 - E_2^\tau = -\left(\partial_0 + \partial_1\right) E_1 + \left(\frac{1}{2}\partial_1^2 - \partial_0 - \partial_2\right) E_0 . \tag{3.107}$$

Inserting equation (3.105) into (3.107) makes the term in front of E_1 vanish and leaves the solvability condition

$$\partial_2 = \frac{1}{2}\partial_0^2 - \partial_0 . \tag{3.108}$$

As the final step, rebuilding the time derivative remains. The general formula for the rebuilt time derivative (3.77) is

$$\frac{\partial}{\partial \xi} = \left(\frac{d}{dt} - \frac{\partial}{\partial T_0}\right) = \epsilon \partial_1 + \epsilon^2 \partial_2 . \tag{3.109}$$

Inserting both solvability conditions from equations (3.105) and (3.108) into (3.109) yields

$$\partial_\xi = -\epsilon \partial_0 + \epsilon^2 \left(\frac{1}{2}\partial_0^2 - \partial_0\right) . \tag{3.110}$$

Rescaling time $\partial_0 \to \partial_0/\epsilon$ and keeping the zeroth order in ϵ results in

$$\frac{\partial E_0}{\partial \xi} = -\partial_0 + \frac{1}{2}\partial_0^2 \tag{3.111}$$

as the multi-scale approximation of equation (3.88) up to second order.

3.3.4 *Example with the Functional Mapping Method*

This section derives the normal form for equation (3.88) for a third time using the functional mapping method. The functional mapping method allows double-checking the results obtained from the multi-scale analysis and vice versa. The approach consists of three steps:

1. Deriving an iterative map for the field evolution in Fourier space from the original equation;
2. Assuming a PDE and integrating it in the slow time to obtain an iterative map;
3. Matching both iterative maps, thereby obtaining the coefficients for the PDE.

Starting point is the scaled version with ϵ introduced

$$\epsilon \frac{d}{dt} E = -E + E(t-1). \tag{3.112}$$

Assuming periodicity for E and transforming into Fourier space $\frac{\mathrm{d}}{\mathrm{d}t} \to -i\omega$ results in

$$-i\epsilon\omega\tilde{E}_n = -\tilde{E}_n + \tilde{E}_{n-1} \tag{3.113}$$

$$\implies \tilde{E}_n = \frac{1}{1 - i\epsilon\omega}\tilde{E}_{n-1} = \mathcal{M}(\omega)\tilde{E}_{n-1}. \tag{3.114}$$

Equation (3.114) shows that the evolution of E can be written as an iterative map with linear multiplier $\mathcal{M}$ in Fourier space.

Assume that a PDE with two time scales ζ and T_0 exists that can be written as

$$\frac{\partial E}{\partial \zeta} = \mathcal{L}(T_0)E. \tag{3.115}$$

Here, ζ is the slow time scale from one round-trip to another round-trip, and T_0 is the fast time scale.

Rearranging the terms and integrating equation (3.115) over one round-trip $\zeta = n$ to $\zeta = n+1$ yields

$$\int_n^{n+1} \frac{1}{E}\frac{\partial E}{\partial \zeta}\mathrm{d}\zeta = \int_n^{n+1} \mathcal{L}\mathrm{d}\zeta \tag{3.116}$$

$$\implies \ln \frac{E_{n+1}}{E_n} = \mathcal{L} \tag{3.117}$$

$$\implies E_{n+1} = e^{\mathcal{L}}E_n. \tag{3.118}$$

Comparing equation (3.118) with equation (3.114) shows that

$$\mathcal{M}(\omega) = e^{\mathcal{L}} \tag{3.119}$$

$$\implies \mathcal{L} = \ln \mathcal{M}(\omega) \tag{3.120}$$

$$= \ln\left(\frac{1}{1 - i\epsilon\omega}\right) \tag{3.121}$$

$$= -\ln(1 - i\epsilon\omega) \tag{3.122}$$

$$= i\epsilon\omega + \frac{1}{2}\epsilon^2\omega^2 + \mathcal{O}(\epsilon^3). \tag{3.123}$$

Inserting $\mathcal{L}$ into the PDE ansatz (3.115) and applying the reverse Fourier transform $-i\omega \to \frac{\partial}{\partial T_0}$ results in

$$\frac{\partial E}{\partial \zeta} = \left(-\frac{\partial}{\partial T_0} + \frac{1}{2}\frac{\partial^2}{\partial T_0^2}\right)E \tag{3.124}$$

as the normal form approximation of equation (3.112).

4

MIXSEL

The results presented in this chapter have been published in

[33] C. Schelte, D. Hessel, J. Javaloyes and S. V. Gurevich. "Dispersive Instabilities in Passively Mode-Locked Integrated External-Cavity Surface-Emitting Lasers." In: *Physical Review Applied* 13 (2020), p. 054050.

4.1 MODEL SYSTEM

The schematic setup of a MIXSEL system is depicted in figure 4.1. The gain and the absorber media are enclosed into a micro-cavity whose length is of the order of the lasing wavelength. The two mirrors of the latter provide additional degrees of freedom for controlling the light-matter interaction; the interaction strength with the active medium —that is only a few tens of nanometers long— can be dramatically increased, at the expense of the available bandwidth, by using high-Q cavities. Similarly, the effective saturation of the active material can be increased (or decreased) by using resonant or anti-resonant cavity designs, respectively. Because of the vast scale separation between the external cavity length and that of the micro-cavity, the natural framework for our theoretical analysis is that of time-delayed systems. The latter appear not only as natural modeling approaches for PML [73, 148] but in many branches of physics.

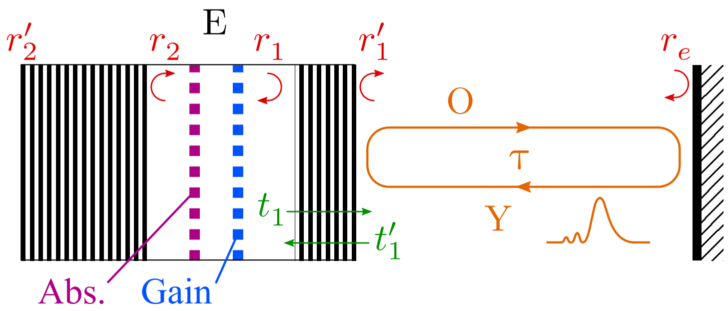

Figure 4.1: A schematic of the MIXSEL configuration, where both gain (blue) and saturable absorption (magenta) are contained in the same micro-cavity. E denotes the field amplitude in the active region. The output and injection fields in the external cavity are represented by O and Y, respectively. The external cavity round-trip time is τ. Reprinted with permission from [33].

We consider the case of a resonant cavity and we denote by E the micro-cavity field and Y the field in the external cavity. The output field is denoted by O, τ is the external cavity round-trip time, whereas $r_{1,2}$ are the top and bottom Distributed Bragg Reflector (DBR) reflectivities, t_1 is the transmission coefficient of the top DBR and r_e is the external mirror reflectivity. We follow the approach presented in section 2.2.1, which is briefly summarized again here, that consists in solving the field propagation in the linear sections of the micro-cavity. That way one obtains a dynamical model linking the two fields E and Y. Their coupling is achieved considering the transmission and reflection coefficients of the top DBR. After normalization, one obtains the rate equations for the field E, the gain N_1 and absorber N_2 population inversions as

$$\dot{E} = \left[(1 - i\alpha_1) N_1 + (1 - i\alpha_2) N_2 - 1\right] E + hY, \tag{4.1}$$

$$\dot{N}_1 = \gamma_1 (J_1 - N_1) - |E|^2 N_1, \tag{4.2}$$

$$\dot{N}_2 = \gamma_2 (J_2 - N_2) - s\,|E|^2 N_2, \tag{4.3}$$

$$Y = \eta O(t - \tau) = \eta \left[E(t - \tau) - Y(t - \tau)\right]. \tag{4.4}$$

We scaled equations (4.1)-(4.4) by the photon lifetime in the micro-cavity κ^{-1}, and α_1 and α_2 are the linewidth enhancement factors of the gain and absorption, respectively. We set the bias and the recovery time in the gain as (J_1, γ_1) and in the absorber section as (J_2, γ_2), respectively. The ratio of the gain and absorber saturation intensities is s. The cavity enhancement due to the high reflectivity mirrors can be scaled out, making that E and Y are of the same order of magnitude. This scaling has the additional advantage of simplifying the input-output relation of the micro-cavity that then reads $O = E - Y$. The minus sign represents the π phase shift of the incoming field Y upon reflection from the top DBR. After a round-trip in the external cavity of duration τ, the output field $O(t - \tau)$ is re-injected with an attenuation factor $\eta = r_e \exp(i\omega_0\tau)$, with $\omega_0\tau$ the propagation phase, defining ω_0 as the carrier frequency of the field. The coupling between E and Y is given in equation (4.4) by a delayed algebraic equation (DAE), that takes into account the multiple reflections in the external cavity. In the limit of a very low external mirror reflectivity $\eta \ll 1$, one would truncate the infinite hierarchy generated by equation (4.4) to obtain $Y = \eta E(t - \tau) + \mathcal{O}(\eta^2)$ leading to the so-called Lang-Kobayashi model [120]. Yet, for mode-locked configurations $\eta = \mathcal{O}(1)$ and the multiple reflections in the external cavity must be taken into account. Instead of considering an infinite number of delayed terms in equation (4.1) with values τ, 2τ, $\cdots$, $n\tau$, the DAE given by equation (4.4) allows for an elegant representation of the strongly coupled cavity dynamics without needing an *a priori* truncation.

The coupling efficiency of the external field Y into the micro-cavity is given by the parameter $h = (1 + |r_2|)(1 - |r_1|)/(1 - |r_1 r_2|)$. There exist three instructive limit cases of this factor corresponding to certain types of devices: A non-transmitting top DBR $|r_1| = 1$ yields $h = 0$ — equivalent to a single mirror. Equal reflectivities for both DBRs $|r_1| = |r_2|$ yield $h = 1$ and correspond to a symmetric Fabry-Perot cavity. Finally, a fully reflecting bottom DBR $|r_2| = 1$ yields $h = 2$, which corresponds to the Gires-Tournois interferometer case [75]. GTIs are known for inducing controllable second order dispersion and they are used as optical pulse-shaping elements. Photons transmitted into the micro-cavity will remain on average for the photon lifetime. When transmitted back into the external cavity they will have collected a phase difference with respect to the photons that are directly reflected from the top DBR. Note that this phase shift is a function of the detuning of the photons to the closest micro-cavity mode. The recombination of both types of photons in the external cavity then leads to dispersion. This process is captured by equation (4.4). Second order dispersion is typically the dominating effect and its amount is tunable by choosing the detuning. Using red or blue detuning one can achieve either normal or anomalous dispersion while around resonance third order dispersion becomes the leading term as the second order contribution vanishes and changes its sign. Gires-Tournois interferometers are designed to conserve the photon number using high reflective bottom mirrors and therefore yield purely dispersive spectrum in models such as given by equations (4.1)-(4.4), see [35] for more details.

In order to achieve directional emission and low losses the bottom DBRs of VCSELs and MIXSELs are optimized towards $|r_2| \to 1$, i.e., they are well approximated by the GTI regime and $h \to 2$. We set the photon lifetime as $\kappa^{-1} = 3\,\text{ps}$ which corresponds to a full width at half maximum of $\kappa\pi^{-1} = 106\,\text{GHz}$. The gain and absorber lifetimes are 1 ns and 30 ps, respectively, while we set the round-trip time in the cavity to 3 ns, hence $(\gamma_1, \gamma_2, \tau) = (0.003, 0.1, 1000)$. If not stated otherwise, the other parameters are $(J_2, \eta, s, h) = (-0.5, 0.7, 10, 2)$.

4.2 SATELLITE INSTABILITY

Due to third order dispersion from the GTI-like micro-cavity pulses can have a series of decaying satellites on the leading edge which might cause an instability of the pulse train [35]. We exemplify the importance of dispersion in equations (4.1)–(4.4) in figure 4.2, where we depict the evolution of a short Gaussian pulse traveling in a lossless external cavity ($\eta = 1$) coupled to a linear micro-cavity operated in the Gires-Tournois regime (i. e., $N_j = J_j = 0$ and h = 2). In the pseudo-space-time representation in figure 4.2, the drift is corrected so that the remaining effect of the third order dispersion is visible. An identical evolution can be obtained by solving the partial differential equation for the field $\tilde{E}(\xi, z)$ given by $\partial_\xi \tilde{E} == d_3 \partial_z^3 \tilde{E}$, which is discussed in section 4.4 and results in equation (4.32). Here, ξ is the round-trip number and z is the fast time variable along the propagation axis. The

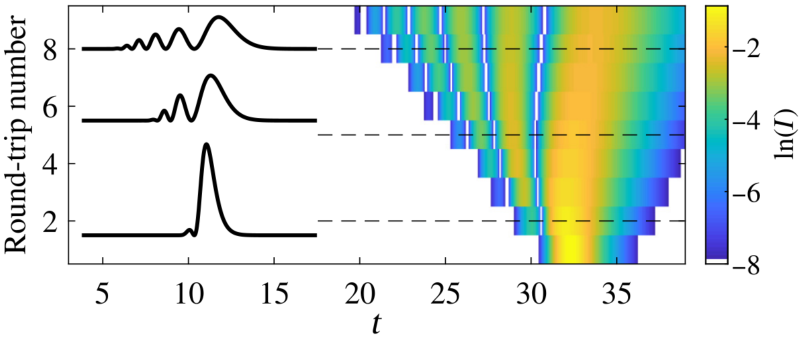

Figure 4.2: A pseudo-space-time diagram of the evolution of a Gaussian pulse in a lossless linear micro-cavity coupled to a perfectly reflecting mirror, i. e., $N_j = J_j = 0$ and $(\eta, h) = (1, 2)$, integrating numerically equations (4.1)–(4.4). The pulse profiles at different round-trips are shown as insets. The dynamics are essentially governed by third order dispersion. Reprinted with permission from [33].

coefficient $d_3 = -2/3$ corresponds to the third order dispersion of the micro-cavity at resonance.

Without linewidth enhancement factors $\alpha_1 = \alpha_2 = 0$ the satellites are most clearly developed because of the absence of chirp, and their instability can be better understood starting from this situation. In a real semiconductor medium the change in carrier density along the pulse profile causes a varying detuning with respect to the micro-cavity resonance due to the alpha factors. The resulting mixture between second and third order dispersion creates a more involved dynamics that will be discussed later in section 4.3.

We operate in the regime of localization where the pulses are temporal localized states (TLSs) that appear below the lasing threshold bias defined, in the long cavity limit, as

$$J_1^{\text{th}} = 1 - J_2 - \frac{h\eta}{1+\eta}. \tag{4.5}$$

As detailed in [125], the TLSs appear via a saddle-node bifurcation of limit cycles. Sufficiently close to the lasing threshold, the main pulses and therefore their parasitic satellites become large enough to bleach the absorber and open the net gain window prematurely. As a consequence, they grow exponentially from one round-trip towards the next while the parent pulse meets an increasingly depleted gain carrier density and eventually dies out. It is replaced by its satellite in front, resulting in forward leaping motion that can best be seen in a pseudo-space-time representation which is shown in figure 4.3 (a) where N_{rt} is the number of round-trips. The corresponding temporal trace obtained from direct numerical simulations (DNSs) of equations (4.1)-(4.4) is depicted in figure 4.3 (b). It demonstrates how this cycle of creation and annihilation leads to a low frequency modulation of the pulse train (see the purple crosses).

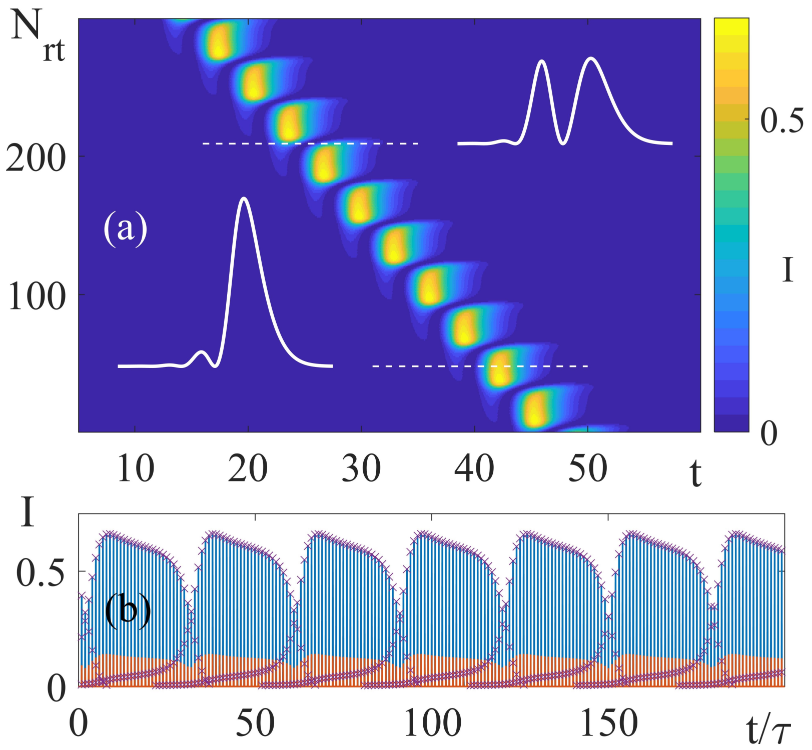

Figure 4.3: Pseudo-space-time diagram (a) and time trace (b) for the pulse train in the unstable satellite regime obtained from DNSs of equations (4.1)-(4.4). The pulse intensity for E (blue) and Y (orange) fields is shown. The purple crosses at the E field intensity peaks illustrate the creation-annihilation cycle. For sufficiently large gain the largest satellite is amplified, eventually replacing its parent pulse. Parameters are $(J_1, \alpha_1, \alpha_2) = (0.65, 0, 0)$. Reprinted with permission from [33].

We show in figure 4.4 (a) a numerical two parameter bifurcation diagram in the (J_1, α_1) plane for the single pulse solution. The latter is obtained using direct numerical integration. Here, the different regimes of TLS behavior are color coded: the blue region corresponds to the off state and cyan to stable TLSs, respectively. For high values of the line-width enhancement factor of the gain α_1, a quasiperiodic instability due to self-phase modulation is found, similar to that discussed in [149]. This instability is found to be a local secondary Andronov-Hopf bifurcation and is depicted in green. In addition to these regimes, which also exist in the generic mode-locked ring- laser model of [148], a different instability induced by third order dispersion is found for low values of α_1 (see the purple region). It corresponds to the regime depicted in figure 4.3. In addition, around $\alpha_1 \approx 1$, there exists a bistability region close to threshold between the principal stable TLS solution (cyan) and another stable passive-mode-locking regime with higher-intensity pulses (color coded in orange). Further, a low-frequency modulated passive mode locking (color coded in red) is also bistable with the principal TLS regime (cyan); these latter quasiperiodic dynamics have the characteristics of both instabilities found for low and high α_1; this is discussed in more detail in section 4.3. Where regions overlap, the colors are blended. Exemplary temporal profiles of three TLS are shown in solid white. Note that the parts along the borders of the pure trailing-edge and satellite instabilities are also bistable with the principal stable passive-mode-locking solution.

We plot in figure 4.4 (b) the branch for the single TLS solution in orange, showing the peak intensity as a function of the scaled gain bias J_1/J_1^{th} obtained using DDE-BIFTOOL [135]. At $\alpha_1 = 0$, the solution branch folds three times at F_1, F_2, F_3 (marked by red circles), with the second fold F_2 at a critical value of the current $J_1^c \sim 0.86 J_1^{\text{th}}$ that coincides with the onset of the satellite instability. The results from the corresponding DNSs are superposed (blue points), indicating the values of the pulse maxima of many round-trips. Shortly after the second fold F_2, a second unstable branch (dashed magenta) appears in a pitchfork bifurcation point BP. Above J_1^c, no stable single-TLS solutions exist and one observes the low-frequency periodic dynamics discussed in figure 4.3.

It should be noted that for $\alpha_1 \ll 1$, this instability does not stem from a local Andronov-Hopf bifurcation but from a global bifurcation. The limit cycle is born with infinite period at the second fold F_2 of the TLS branch in Fig 4.4 (b). To identify the type of the global bifurcation, the scaling of the oscillations period close to the critical value J_1^c is analyzed. The resulting period scaling is presented in figure 4.5 (a), where we show the period evolution for two exemplary small values of α_1 (blue and red crosses) and the characteristic scalings for saddle-node infinite-period (SNIPER) $(\mu^{1/2})$ and homoclinic $(-\ln \mu)$

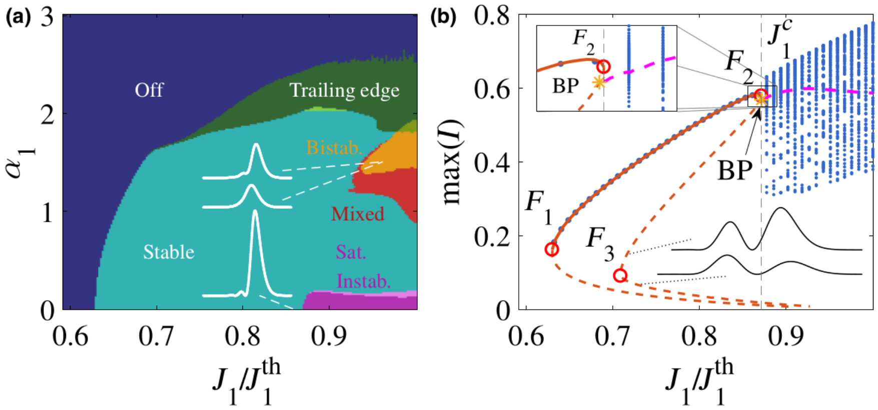

Figure 4.4: (a) Bifurcation diagram in the (J_1, α_1)-plane obtained with DNSs of equations (4.1)-(4.4) for $\alpha_2 = 0$. The different regimes of TLS behavior are color coded blue for the off state, cyan for stable, green for the trailing-edge instability at high α_1, and purple for the satellite instability at low α_1. A bistable region between the principal (cyan) and a more energetic TLS is shown in orange. The latter can become unstable and its oscillating regime is depicted in red. This oscillation exhibits mixed dynamics of both previous instabilities. The cyan and green regions continue unaffected underneath this bistable region. Where regions otherwise overlap, the colors are blended. Exemplary temporal profiles of three TLSs are shown in solid white. These are mutually up to scale: the dashed white lines indicate their parameters. The upper and central profiles correspond to orange and cyan regions, respectively. (b) A branch of a single pulse solution showing the peak intensity max(I) as a function of the scaled gain bias J_1/J_1^{th}, superposing results from DNS (blue points) and path continuation (orange line) for $\alpha_1 = 0$. The branch has three folds F_i on the limit cycle (red circles) and stability is indicated by a solid line, otherwise dashed. The satellite instability does not stem from secondary Andronov-Hopf bifurcation. After the fold F_2 on the unstable branch, there is a supercritical pitchfork bifurcation BP (yellow star) that gives birth to another unstable branch (magenta). Reprinted with permission from [33].

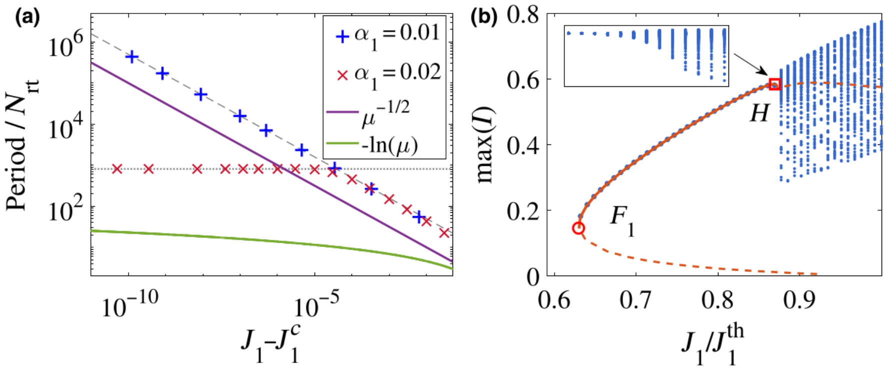

Figure 4.5: (a) The dependence of the period on the distance to the bifurcation point J_1^c for two different values of α_1. The crosses denote the period obtained from direct numerical simulations of equations (4.1)-(4.4) for $\alpha_1 = 0.01$ (blue) and $\alpha_1 = 0.02$ (red). The asymptotic trends of the periods are infinity and constant, respectively. The straight lines correspond to the theoretically predicted scaling behavior for a homoclinic (green) and a SNIPER (purple) bifurcation, for comparison. The gray dashed and dotted lines illustrate the evolution of the blue and red crosses and are guides for the eye. (b) A branch of a single-TLS solution, showing the peak intensity as a function of the gain bias J_1 scaled to J_1^{th}, superposing results from direct numerical simulations (blue points) and path continuation (orange) for $\alpha_1 = 0.02$. The branches have reconnected and the pitchfork BP and fold points F_2 have merged into an Andronov-Hopf bifurcation point H. The satellite instability now starts at H, with a small amplitude and a finite period (see the inset). Reprinted with permission from [33].

bifurcations as a function of the distance to the bifurcation point J_1^c. The gray dashed and dotted lines illustrate the evolution of the blue and red crosses and are guides for the eye. The results reveal that for very small values of α_1 (cf. the scaling for $\alpha_1 = 0.01$), the satellite instability can be identified to be of the SNIPER type, since the period diverges as an inverse square root as J_1^c is approached (cf. the characteristic scaling in magenta). However, for increasing α_1, the SNIPER bifurcation changes into a local Andronov-Hopf bifurcation. Indeed, the scaling for $\alpha_1 = 0.02$ in figure 4.5 (a) indicates that in this case the period is finite at the bifurcation point and fits neither the SNIPER nor the homoclinic scaling laws. The corresponding branch of the single TLS obtained from the continuation (orange line) and direct numerical simulations (blue points) for $\alpha_1 = 0.02$ is shown in figure 4.5 (b). One can see that the bifurcation structure is different from that of figure 4.4 (b): here, there is no limiting point on the high-power branch and it continues without the additional folds F_2 and F_3 and only becomes Andronov-Hopf unstable at the bifurcation point H. The inset shows the emergence of the periodic solution with the finite amplitude in the vicinity of the H bifurcation point.

4.3 COMBINED INSTABILITIES

With realistic linewidth enhancement factors for semiconductor media the satellite and self-phase modulation instabilities combine to form a dynamics of the kind presented in [35]. By performing parameter scans as a function of various parameters we were able to deduce some general features of the satellite instability. Generally, the pulse-width is proportional to the photon lifetime and can be written as $\tau_p = \kappa^{-1} f(\cdots)$ with $f(\cdots)$ a function that depends on all the other parameters of the PML setup. Optimizing PML consists in finding the parameter combination for which the function f approaches unity. It is in these optimal cases for which $\tau_p \sim \kappa^{-1}$ where, as depicted in figure 4.3, the satellites become better resolved and are prone to become unstable. Hence, the satellite instability can be obtained by tuning any parameter leading to the optimal pulse-width, making it an essential limitation in the optimization procedure to find the narrowest pulse widths. For instance, increasing the saturation s or even the linewidth enhancement factor of the absorber α_2, if it compensates for the chirp induced in the gain section. Note that in the VCSEL-SESAM setup the detuning between the micro-cavities is an additional factor in this balance. Finally, we show in figure 4.6 how the satellite instability evolves in more realistic situations with $\alpha_1 = 2.1$ and $\alpha_2 = 0.5$. We note that, in addition, this regime can be bistable with the stable pulsating solution, see figure 4.4 (a).

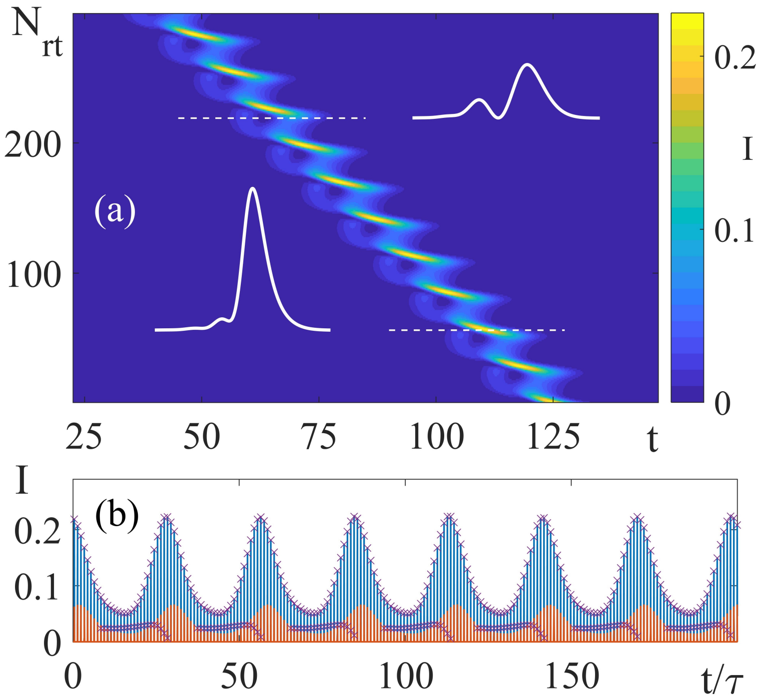

Figure 4.6: Pseudo-space-time diagram (a) and corresponding time trace (b) for the single pulse train in the satellite unstable regime. The pulse intensity for E (blue) and Y (orange) fields are shown. With realistic values of the linewidth enhancement factors the dynamics is more involved due to the chirp that induces pulse broadening. Here, instead of dying out completely the parent pulse merges with its growing satellite. Parameters are $(J_1, \alpha_1, \alpha_2) = (0.65, 2.1, 0.5)$. Reprinted with permission from [33].

4.4 MASTER EQUATION

As bifurcation analysis does not always allows for an intuitive interpretation of the dynamics, that can furthermore stay hidden in the structure of time-delayed equations, even if they contain most of the physics of PML, we derive in this section a partial differential equation (PDE) for the field amplitude E that shall approximate the dynamics of the full DADE model (4.1)-(4.4). In the PDE representation, the field depends on a slow and a fast time, i.e. $E \equiv E(\xi, z)$. Here, the slow time ξ represents the evolution of the field profile from one round-trip to the next while the "spatial variable" z describes the fast evolution of the pulse within the round-trip. While this approach has been used in several time-delayed systems, see e.g., [71, 72] for a review, such PDE models are usually termed Haus master equations in the framework of mode-locking as the Haus equation was originally derived to study active mode-locking, see [23] for a review.

In the case of high frequency PML dynamics, i.e. the regimes in which the cavity round-trip is much shorter than the gain recovery time, a PDE approximating the dynamics of a ring cavity model based upon delayed differential equations [148] was proposed in [150]. The multiple time scales analysis method was used and the scaling of parameters consisted in assuming low losses, low gain, and weak spectral filtering. In the model of [148], these three physical effects are controlled by three independent parameters. In the multiple time scales approach one finds, at the lowest order, a periodic solution, e.g., a pulse evolving over the fast time scale z that circulates in the cavity without deformation. At third order in the expansion scheme, a solvability condition allows finding that the dynamics on the slow time scale ξ is governed by the weak effects of gain, loss and spectral filtering. In the PDE representation, the gain filtering in the model of [148] takes the form of a diffusion over the fast time, i.e. a term $d_2 \partial_z^2 E$ with $d_2 > 0$. While the smallness of gain, losses and filtering can be, in some situations, debatable, the advantage of the approach presented in [150] is the uniform accuracy of the PDE representation that was not, e.g., limited to the vicinity of the lasing threshold. For instance, no *a priori* conditions over the magnitude of the field were necessary.

However, it is interesting —and surprising— to notice that the aforementioned approach fails if one tries to export it to the case of the DADE model (4.1)-(4.4); the resulting PDE obtained similarly as a third order solvability condition does possess gain and losses, yet it is devoid of spectral filtering $(d_2 = 0)$ which leads to singular dynamics and unphysical pulse collapse. The physical reason that underlies this mathematical phenomenon is that the filtering of the micro-cavity in our modeling approach is not independent from gain and losses. It is the actual level of the population inversion in the micro-cavity that defines the breadth and hence the curvature of the resonance. This effect is particularly pronounced in the Gires-Tournois regime (i.e., $h = 2$), where the empty cavity reflectivity is unity, which corresponds to no curvature at all and $d_2 = 0$. That is, positive (resp. negative) curvature induces diffusion (resp. anti-diffusion). Generally, the average gain experienced by the pulse must be positive to compensate for the cavity losses incurred by the mirror reflectivity η.

A proper analysis of the model given by equations (4.1)-(4.4) shall result in a PDE whose diffusion term d_2 depends on other parameters such as the cavity losses. This discussion materializes by taking the cavity at the lasing threshold as the expansion point instead of the empty cavity, as done in [150]. At the lasing threshold, the unsaturated gain and losses exactly compensate. This modification will allow to obtain the filtering induced by the cavity at threshold, instead of that of the empty cavity. The drawback of our approach is that we have to assume the pulse to be not too intense and treat the nonlinear effects perturbatively.

We start by normalizing time by the cavity round-trip τ time as $\sigma = t/\tau$ and define a smallness parameter $\varepsilon = 1/\tau$. As we operate in the long cavity limit, the carriers are not independent functions of time that can lead to resonant terms and solvability conditions. Instead, the carrier evolutions depend uniquely on the initial conditions at the beginning of the round-trip, which in the long cavity limit is the equilibrium value, and on the amplitude of the field, i.e., $N_j = N_j\left(J_j, E\right)$. Hence, we can concentrate solely on the field dynamics that reads

$$\begin{aligned} \varepsilon\frac{dE}{d\sigma} &= \left[\left(1-i\alpha_1\right)N_1 + \left(1-i\alpha_2\right)N_2 - 1\right]E + hY, && (4.6)\\ Y\left(\sigma\right) &= \eta\left[E\left(\sigma-1\right) - Y\left(\sigma-1\right)\right]. && (4.7) \end{aligned}$$

We assume a small deviation of the gain and absorber with respect to their equilibrium values that we scales as

$$N_j = J_j + \varepsilon^3 n_j \qquad (4.8)$$

with $j \in [1,2]$. We also assume η to be real as the feedback case is irrelevant in the long cavity regime. Defining the Fourier transform of the field profiles at the n-th round-trip as $\left(E_n, Y_n\right)$ and using that $\frac{d}{d\sigma} \to -i\omega$ we obtain

$$\left(1 - G_t - i\varepsilon\omega\right)E_n = hY_n + \varepsilon^3\sum_{j=1}^{2}\left(1-i\alpha_j\right)\left(n_j E\right)_n, \qquad (4.9)$$

where total complex gain $G_t = \left(1-i\alpha_1\right)J_1 + \left(1-i\alpha_2\right)J_2$ was used as a shorthand.

Noticing that the DAE for $Y(\sigma)$ in Fourier space reads

$$Y_n + \eta Y_{n-1} = \eta E_{n-1} \tag{4.10}$$

and, by making a linear combination of E_n and ηE_{n-1} as well as simplifying, we obtain the functional mapping

$$\begin{aligned} E_n = {} & \eta \frac{h - 1 + G_t + i\varepsilon\omega}{1 - G_t - i\varepsilon\omega} E_{n-1} \\ & + \varepsilon^3 \frac{1}{1 - G_t - i\varepsilon\omega} \sum_{j=1}^{2} \left(1 - i\alpha_j\right) \left[\left(n_j E\right)_n + \eta \left(n_j E\right)_{n-1}\right]. \end{aligned} \tag{4.11}$$

We impose the value of G_t to be a convenient expansion point and set the threshold condition through the linear multiplier μ

$$\mu = \eta \frac{h - 1 + G_t + i\varepsilon\omega}{1 - G_t - i\varepsilon\omega} = 1, \tag{4.12}$$

which allows finding the lasing frequency shift at threshold as

$$\varepsilon\omega_t = \alpha_1 J_1 + \alpha_2 J_2. \tag{4.13}$$

This leaves us with a real equation for the amplification factor

$$\eta \frac{h - 1 + N_t}{1 - N_t} = 1\,, \tag{4.14}$$

where we defined $N_t = J_1 + J_2$. The last relation implies that the threshold is defined by

$$N_t = J_1 + J_2 = 1 - \frac{h\eta}{1 + \eta}\,. \tag{4.15}$$

We can now express the field multiplier μ from one round-trip towards the next as

$$\mu\left(\omega, N_t\right) = \eta \frac{h - 1 + N_t + i\varepsilon\left(\omega - \omega_t\right)}{1 - N_t - i\varepsilon\left(\omega - \omega_t\right)} \tag{4.16}$$

and the functional mapping given by equation (4.11) reads

$$\begin{aligned} E_n = {} & \eta \frac{h - 1 + N_t + i\varepsilon\left(\omega - \omega_t\right)}{1 - N_t - i\varepsilon\left(\omega - \omega_t\right)} E_{n-1} \\ & + \varepsilon^3 \frac{1}{1 - N_t - i\varepsilon\left(\omega - \omega_t\right)} \sum_{j=1}^{2} \left(1 - i\alpha_j\right) \left[\left(n_j E\right)_n + \eta \left(n_j E\right)_{n-1}\right]. \end{aligned} \tag{4.17}$$

One only needs equation (4.17) to be accurate up to third order in ε in order to obtain the proper expression of the diffusion, third order dispersion and nonlinear terms. As such, we can simplify the last term of equation (4.17) by replacing the value of E_n at the lowest order, i.e., we can set

$$E_n = \eta \frac{h - 1 + N_t}{1 - N_t} E_{n-1} + \mathcal{O}\left(\varepsilon\right) = E_{n-1} + \mathcal{O}\left(\varepsilon\right), \tag{4.18}$$

where we used the threshold definition given by equation (4.15). Using that $E_n = E_{n-1}$ in the nonlinear term of equation (4.17), replacing the expression of the threshold and noticing that all the frequencies are relative to that of the lasing threshold, so that one can set $\tilde{\omega} = \omega - \omega_t$, yields the expression

$$\begin{aligned} E_n &= \eta \frac{h-1+N_t+i\varepsilon\tilde{\omega}}{1-N_t-i\varepsilon\tilde{\omega}} E_{n-1} \\ &+ \varepsilon^3 \frac{(1+\eta)^2}{h\eta} \sum_{j=1}^{2} \left(1-i\alpha_j\right) \left(n_j E\right)_{n-1} + \mathcal{O}\left(\varepsilon^4\right) . \end{aligned} \tag{4.19}$$

Now let us assume there exists a PDE for the field $E(\xi, z)$ with ξ and z the slow and fast times, respectively. In Fourier space for the variable z, one obtains

$$\partial_\xi E = \mathcal{L}(\tilde{\omega}) E + \varepsilon^3 \mathcal{N}(\xi, \tilde{\omega}) . \tag{4.20}$$

The form of equation (4.20) consists naturally of a linear operator $\mathcal{L}(\tilde{\omega})$ that should correspond to the linear multiplier of the mapping in equation (4.19), while $\mathcal{N}(\sigma, \tilde{\omega})$ accounts for nonlinear gain and absorber effect. We assume that $\mathcal{L}(\tilde{\omega})$ is small, i.e, $\mathcal{L}(\omega) \sim 0 + \mathcal{O}(\varepsilon)$. Such a scaling is consistent with the definition of the lasing threshold and will be checked a posteriori. Integrating equation (4.20) *exactly* over a round-trip yields

$$E_n = e^{\mathcal{L}} E_{n-1} + \varepsilon^3 \int_{n-1}^{n} e^{(n-\xi)\mathcal{L}} \mathcal{N}(\xi, \tilde{\omega})\, d\xi . \tag{4.21}$$

Because the integral term in equation (4.21) is already at third order in ε, we can approximate $e^{(n-\xi)\mathcal{L}} = 1 + \mathcal{O}(\varepsilon)$ and evaluate the nonlinear operator using the Euler explicit method. Indeed, since $\mathcal{N}$ depends on the field, the error in the integration will be proportional to the slow evolution of the field from one round-trip towards the next, i.e., $\partial_\xi \mathcal{N} \sim \partial_\xi E \sim \mathcal{O}(\varepsilon)$. That is, we find

$$E_n = e^{\mathcal{L}} E_{n-1} + \varepsilon^3 \mathcal{N}(n-1, \tilde{\omega}) + \mathcal{O}\left(\varepsilon^4\right) . \tag{4.22}$$

Comparing equation (4.19) and equation (4.22) we deduce that

$$\mathcal{L} = \ln\left(\eta \frac{h-1+N_t+i\varepsilon\tilde{\omega}}{1-N_t-i\varepsilon\tilde{\omega}}\right) . \tag{4.23}$$

Using equation (4.15) the last expression can be simplifies as

$$\mathcal{L} = \ln\left(\frac{1+i\varepsilon\eta\frac{1+\eta}{h\eta}\tilde{\omega}}{1-i\varepsilon\frac{1+\eta}{h\eta}\tilde{\omega}}\right) . \tag{4.24}$$

We can verify easily that $\mathcal{L} = \mathcal{O}(\tilde{\varepsilon})$ which allows to check a posteriori our approximation regarding the order of the operator $\mathcal{L}$. One can also expand equation (4.24) in $\tilde{\omega}$ up to third order yielding the drift, diffusion and third order dispersion coefficients d_1, d_2 and d_3 as

$$\mathcal{L} = d_1 \left(-i\varepsilon\tilde{\omega}\right) + d_2 \left(-\varepsilon^2\tilde{\omega}^2\right) + d_3 \left(i\varepsilon^3\tilde{\omega}^3\right) + \mathcal{O}\left(\varepsilon^4\right) \tag{4.25}$$

with

$$\begin{aligned} d_1 &= -\frac{(\eta+1)^2}{h\eta}, && (4.26) \\ d_2 &= \frac{1-\eta^2}{2}\left(\frac{\eta+1}{h\eta}\right)^2, && (4.27) \\ d_3 &= -\frac{\eta^3+1}{3}\left(\frac{\eta+1}{h\eta}\right)^3. && (4.28) \end{aligned}$$

The values of the coefficient d_j are particularly instructive and, in particular, how they deviate from the expression one can find easily in the case of an empty Gires-Tournois micro-cavity coupled to an external mirror: $(d_1, d_2, d_3) = (-2, 0, -2/3)$. Here, we notice that although d_1 and d_3 are modified by the value of the cavity losses, the value of d_2 is vanishing. In the good cavity limit $\eta \to 1$, we have $d_2 \sim 1-\eta \to 0$, which explains why third order dispersion is important as it becomes the leading order term.

Further, we identify the nonlinear operator $\mathcal{N}$ as

$$\mathcal{N}\left(n-1, \tilde{\omega}\right) = \frac{(1+\eta)^2}{h\eta}\sum_{j=1}^{2}\left(1-i\alpha_j\right)\left(n_j E\right)_{n-1} \tag{4.29}$$

Finally, reverting equation (4.20) to direct space using that $-i\varepsilon\tilde{\omega} \to \partial_z$, the sought PDE for the field E reads

$$\begin{aligned} \partial_\xi E &= \left(d_1\partial_z + d_2\partial_z^2 + d_3\partial_z^3\right) E && (4.30) \\ &+ \frac{(1+\eta)^2}{h\eta}\sum_{j=1}^{2}\left(1-i\alpha_j\right)\left(N_j - J_j\right) E. \end{aligned}$$

By using the definition of the lasing threshold and that of the carrier frequency, we find that the dispersive master equation for the field E in the long cavity limit reads

$$\begin{aligned} \partial_\xi E &= \left(d_1\partial_z + d_2\partial_z^2 + d_3\partial_z^3\right) E && (4.31) \\ &+ \frac{(1+\eta)^2}{h\eta}\left\{\left(1-i\alpha_1\right) N_1 + \left(1-i\alpha_2\right) N_2 - 1 + \frac{h\eta}{1+\eta} - i\omega_t\right\} E, \end{aligned}$$

whereas the equations for the carriers N_1 and N_2 take the form

$$\begin{aligned} \frac{\partial N_1}{\partial z} &= \gamma_1(J_1 - N_1) - |E|^2 N_1, && (4.32) \\ \frac{\partial N_2}{\partial z} &= \gamma_2(J_2 - N_2) - s|E|^2 N_2. && (4.33) \end{aligned}$$

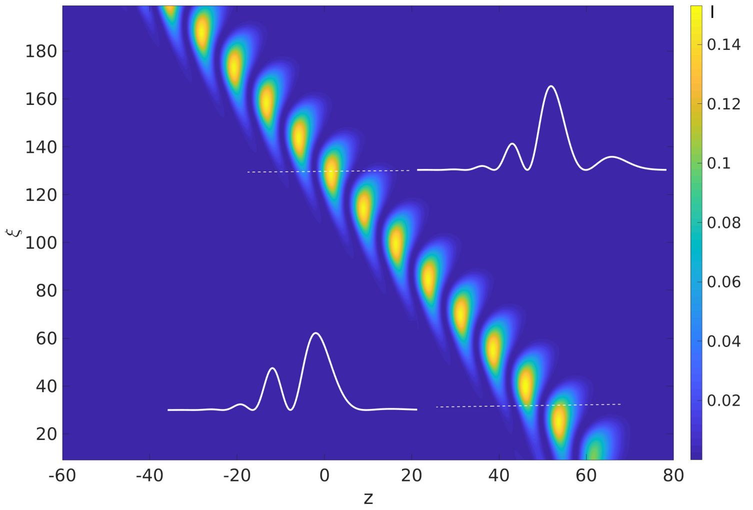

Figure 4.7: Space-time diagram of the satellite instability found in the DNS of the master PDE (4.32)-(4.33). The pulse intensity $I = |E|^2$ is shown. Parameters are $(J_1, J_2, \alpha_1, \alpha_2, \eta, s) = (0.119, -0.1, 0, 0, 0.9, 15)$. Reprinted with permission from [33].

Note that the rotation term $i\omega_t$ in equation (4.32) is immaterial and can be removed by setting $\tilde{E}\left(\xi, z\right) = E\left(\xi, z\right)\exp\left(i\omega_t\xi\right)$.

First, a numerical study of the PDE model (4.32)-(4.33) demonstrates the existence of the satellite instability in the parameter space and the resulting space-time diagram obtained for zero linewidth enhancement factors $\alpha_1 = \alpha_2 = 0$ is shown in figure 4.7. Again, we observe the clean cut satellite instability in this parameter range.

To compare the PDE (4.32)-(4.33) with the DAE (4.1)-(4.4) in detail we performed bifurcation analysis of the PDE by using pseudo-arclength continuation methods within the pde2path framework [151]. To this aim, first we seek for the steady localized pulse solutions of equations (4.32)-(4.33) that can be found by setting $E(z,\xi) = E(z - v\xi)e^{-i\varpi\xi}$ leading to the following equation for the stationary field E

$$\begin{aligned} 0 &= v\frac{\partial E}{\partial z} + d_2\frac{\partial^2 E}{\partial z^2} + d_3\frac{\partial^3 E}{\partial z^3} + i\varpi E \\ &+ \frac{(1+\eta)^2}{h\eta}\left((1-i\alpha)N_1 + (1-i\beta)N_2 - 1 + \frac{h\eta}{1+\eta}\right)E\,. \end{aligned} \tag{4.34}$$

Note that both the spectral parameter ϖ and the drift velocity v become free parameters that can be found by imposing additional auxiliary integral conditions. In addition we set the following boundary conditions for the domain $z \in [0, L]$

$$\begin{aligned} \left.\frac{\partial E}{dz}\right|_{z=0,L} &= 0\,, \\ \left.N_1\right|_{z=0} &= J_1\,, \quad -\left.\frac{\partial N_1}{\partial z}\right|_{z=L} + \gamma_1\left(J_1 - \left.N_1\right|_{z=L}\right) = 0\,, \\ \left.N_2\right|_{z=0} &= J_2\,, \quad -\left.\frac{\partial N_1}{\partial z}\right|_{z=L} + \gamma_2\left(J_2 - \left.N_2\right|_{z=L}\right) = 0\,. \end{aligned}$$

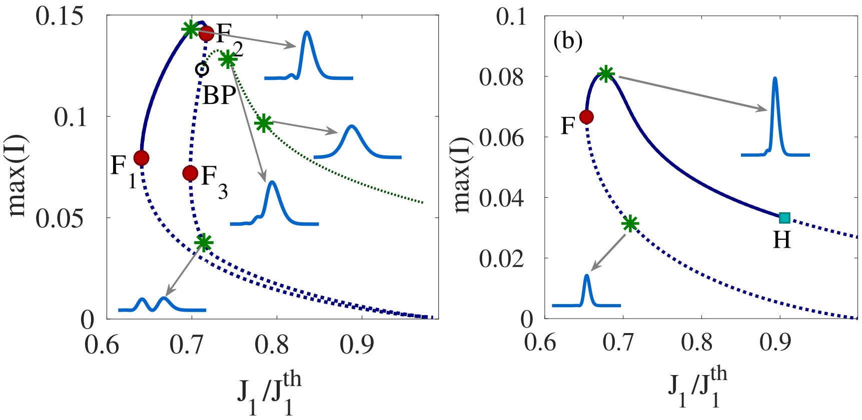

Figure 4.8: Branches of the TLSs in the master PDE (4.32)-(4.33). The maximum of the field intensity $I = |E|^2$ as a function of the normalized pump current is shown. (a) For $(\alpha_1, \alpha_2) = (0, 0)$ the pulse profiles show defined satellites. The branch has three folds F_i and a branching point BP. The second fold F_2 coincides with an infinite period limit cycle in a global SNIPER bifurcation. An unstable branch emerges from BP in a pitchfork bifurcation. (b) For $(\alpha_1, \alpha_2) = (1.5, 0.5)$, F_2 and BP have merged into an Andronov-Hopf bifurcation point H. The profiles only show intensity bumps on the leading edge of the pulse and there is no longer a SNIPER. Other parameters are $(J_2, \eta, s) = (-0.1, 0.9, 15)$. Reprinted with permission from [33].

Next, we follow the TLS of the PDE (4.32)-(4.33) in parameter space and in figure 4.8 we present two branches of TLSs for different values of the linewidth enhancement factors. Panel (a) shows the intensity of the TLS as a function of the normalized pump rate for the case of $\alpha_1 = \alpha_2 = 0$. Like in the DAE case (cf. figure4.4), one can see that the branch folds three times (points F_i) when continuing in the pump rate J_1 and the second fold F_2 is responsible for the SNIPER bifurcation after the first leading satellite becomes sufficiently large to saturate the absorber (cf. figure 4.7). Note that an additional unstable branch connects to the main one in a branching point BP. Panel (b) shows the same gain interval for non-vanishing linewidth enhancement factors $\alpha_1 = 1.5$ and $\alpha_2 = 0.5$. Here, the branch continues without the additional folds F_2 and F_3 and only becomes Andronov-Hopf unstable at large gain value. Indeed, the second fold and the branching point have merged while the part of the branch with the third fold has detached, giving a qualitatively different scenario. The chirp induced by the linewidth enhancement factors smears out the third order dispersion effect responsible for the satellites.

Finally, in figure 4.9 we superpose the results on top of data obtained through DNSs of the DAE model (4.1)-(4.4) in the long delay limit using the functional mapping approach [133]. Pulses are fully localized TLSs in this regime. In panel (a) the standard deviation of the pulse energy is shown as a function of the gain bias J_1 normalized to threshold J_1^{th} and the gain linewidth enhancement factor α_1 along with the bifurcation curves from continuation. For small α_1 one can see the satellite unstable region which is similar to the previous parameter set, i.e., close to $\alpha_1 = 0$ there is an additional fold presented in solid blue and the satellite instability sets in as a global SNIPER bifurcation after it. Panel (b) shows a zoom-in on this area where the fold merges with a branching point (dotted blue), thereby forming an Andronov-Hopf bifurcation depicted in dash dotted red. Both models quantitatively agree in this area. The principal fold of the subcritical TLS branch in solid red is also reproduced correctly. For higher α_1 the stable pulse region is limited by another Andronov-Hopf bifurcation corresponding to self-phase modulation, shown as well in dash dotted red. In contrast to the DAE, for the PDE model the bifurcation curve slopes down in α_1 for increasing gain. Both the nature of the instability and the discrepancy found in the equivalent PDE are somewhat similar to the bifurcation structure in the Vladimirov-Turaev model for passive mode-locking in a unidirectional ring laser [148, 149].

For the parameters of figure 4.9 (a), the DAE system exhibits a region close to threshold at high values of α_1 that is partly stable. The corresponding fold and Andronov-Hopf curves, shown in dotted orange and indicated by red crosses, respectively, are found in the PDE with a qualitatively similar shape but the position of this area is shifted significantly towards lower gain as compared to the DAE. This region corresponds to the bistable region for the previous parameter set. Indeed we found that generally it moves and changes shape significantly as a function of the other parameters and so do the principal pulse and satellite instability regions. For example, by increasing α_2, the lower region of stable pulses shifts up in α_1 by roughly the same amount, while the satellite instability moves down. The second region moves up in α_1 much quicker and completely detaches, at least when constricting one's view at the area below threshold (see figure 4.10).

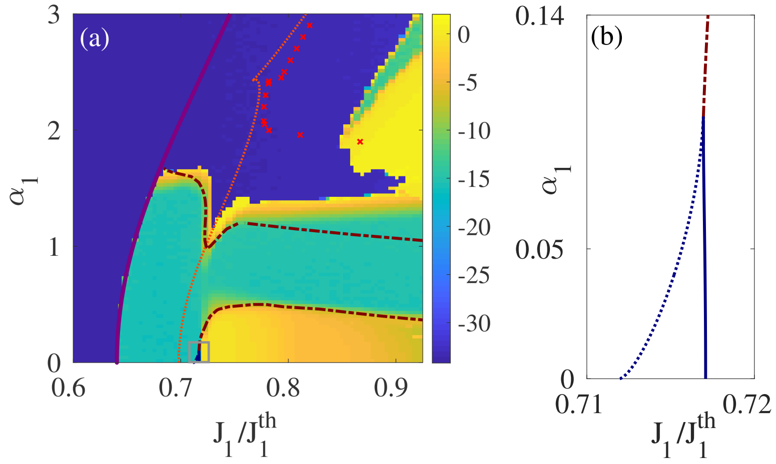

Figure 4.9: (a) Bifurcation diagram in the (J_1, α_1) plane of the DAE model (4.1)-(4.4) in the long delay limit superposed with the bifurcation diagram of the equivalent PDE (4.32)-(4.33). The color coding shows the standard deviation of the pulse energy obtained by DNSs of the DAE. The evolution of the fold F_1 is marked by a solid red line, the satellite instability around $\alpha_1 = 0$ with the corresponding fold F_3 (branching point) is in solid (dotted) blue and the Andronov-Hopf part in dash dotted red. The other Andronov-Hopf bifurcation corresponding to self-phase modulation slopes down for the PDE case in contrast to the DAE. The high α_1 region in the PDE is significantly shifted with respect to the DAE. Its fold branch is depicted in dotted orange and Andronov-Hopf bifurcations are indicated by red crosses. Parameters are $(J_2, \alpha_2, \eta, s) = (-0.1, 0, 0.9, 15)$. (b) Zoom-in on the SNIPER region where a fold and a branching point merge into an Andronov-Hopf bifurcation. Reprinted with permission from [33].

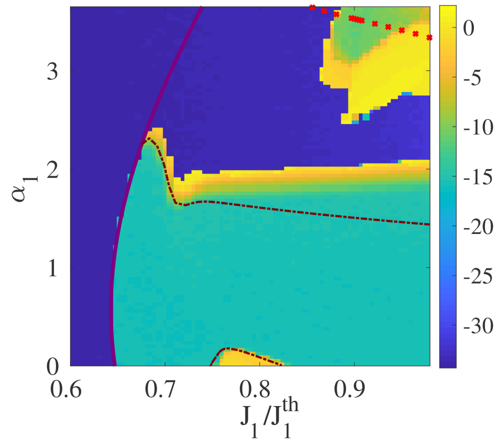

Figure 4.10: For larger α_2 the different regions move and deform. The stable pulse region moves up in α_1 by a similar amount while the satellite region moves down. The high α_1 region completely detaches in the area below threshold. Results from bifurcation analysis of the PDE strongly differs from the DAE in this region. Parameters are $(J_2, \alpha_2, \eta, s) = (-0.1, 0.5, 0.9, 15)$. Reprinted with permission from [33].

5

VCSEL-RSAM

The results presented in sections 5.1 and 5.3 have been published in

[34] D. Hessel, S. V. Gurevich and J. Javaloyes. “Wiggling instabilities of temporal localized states in passively mode-locked vertical external-cavity surface-emitting lasers.” In: *Optics Letters* 46 (2021), pp. 2557–2560.

The results presented in sections 5.2, 5.4 and 5.5 are in preparation for submission:

[152] D. Hessel, S. V. Gurevich and J. Javaloyes. “Super mode-locking in passively mode-locked vertical external-cavity surface-emitting lasers.” *(in preparation)*.

5.1 MODEL SYSTEM

The schematic setup the VCSEL-RSAM system is depicted in Fig. 5.1 (a). It consists of two micro-cavities: a VCSEL gain mirror and a resonant saturable absorber mirror separated by a time of flight τ. The fields in the micro-cavities are denoted E_i, where $i = 1, 2$ correspond to the gain and the absorber mirrors, respectively. The output field O_i of each nonlinear mirror turns into the injection field Y_i of the other after passing a beam splitter that is used to extract a signal. The system is operated in the regime where the round-trip time is much longer than the semiconductor gain recovery time. In this so-called long cavity regime, TLSs can be observed below the continuous wave (CW) threshold [125, 133]. One typical time trace corresponding to stable fundamental mode-locking in the long cavity regime is depicted in Fig. 5.1 (b). There, the shape of the pulse does not change from round-trip to round-trip as can be seen more easily in the pseudo space-time representation in Fig.5.7 (a).

Following the approach developed in [35, 73, 133, 153] and presented in section 2.2.1, one can write the dynamical model for the intra-cavity fields E_i and population inversions N_i as

$$\kappa_1^{-1}\dot{E}_1 = \left[(1 - i\alpha_1)N_1 - 1\right] E_1 + h_1 Y_1 \,, \tag{5.1}$$

$$\kappa_2^{-1}\dot{E}_2 = \left[(1 - i\alpha_2)N_2 - 1 + i\delta\right] E_2 + h_2 Y_2 \,, \tag{5.2}$$

$$\dot{N}_1 = \gamma_1(J_1 - N_1) - |E_1|^2 N_1 \,, \tag{5.3}$$

$$\dot{N}_2 = \gamma_2(J_2 - N_2) - s|E_2|^2 N_2 \,. \tag{5.4}$$

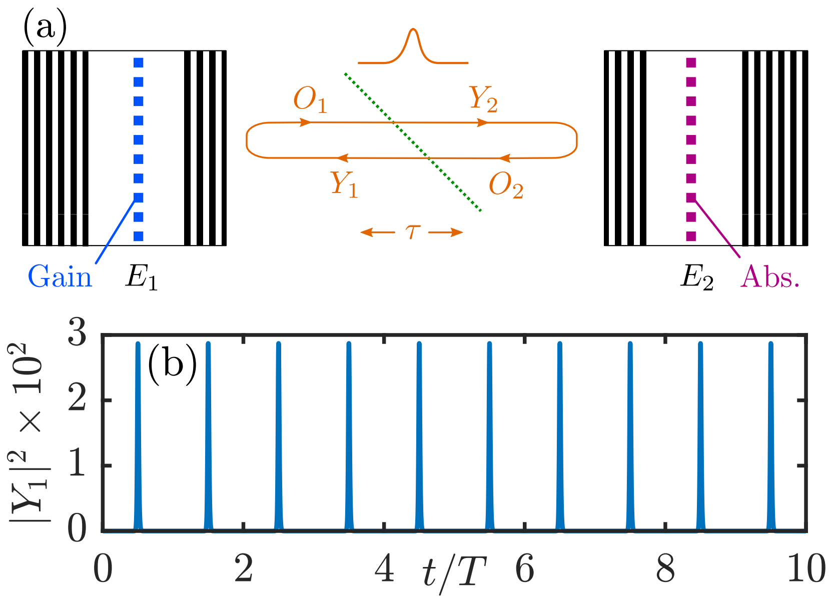

Figure 5.1: (a) A schematic setup of the VCSEL-RSAM. (b) The system can exhibit temporal localized structures below the threshold for continuous wave emission. (b) is a time trace of equations (5.1)-(5.5) for $j = 0.5406$. The time has been trimmed to contain only the fast stage of the pulses. Reprinted with permission from [34].

Here, κ_i^{-1} are the photon lifetimes, α_i are the linewidth enhancement factors and δ is the detuning between the two micro-cavities, J_i are the bias in the gain and the absorber sections and γ_i are the corresponding lifetimes. The ratio of the gain and absorber saturation intensities is s. The field injected into a micro-cavity is denoted with Y_i whilst the coupling parameters $h_i \in [0, 2]$ depend on the cavity mirror reflectivities. The two micro-cavities mutually inject each other and their outputs is a superposition of the reflected and emitted fields. The link between the two micro-cavities, considering all multiple reflections, is given by two DADEs that physically correspond to the boundary conditions linking the fields defined in the three cavities composing the system,

$$Y_{1,2}(t) = \eta \left[E_{2,1}(t-\tau) - Y_{2,1}(t-\tau) \right] , \tag{5.5}$$

where η is the amplitude transmission of the beam splitter and the minus sign before the injected field represents a phase shift of π upon reflection from the top Bragg mirror.

We choose the photon and carrier lifetimes as $(\kappa_1^{-1}, \kappa_2^{-1}) = (343, 80)$ fs and $(\gamma_1^{-1}, \gamma_2^{-1}) = (800, 50)$ ps and the linewidth enhancement factors are set to $(\alpha_1, \alpha_2) = (2.5, 1)$. The saturable absorption modulation is 25%, which corresponds to $J_2 = -0.07$, whereas the ratio of the saturation energies of the gain and the absorber is $s = 5$ [126]. The beam splitter losses per pass are 2% in intensity hence $\eta = 0.99$. The round-trip time is $2\tau = 3.4$ ns which fullfils the long cavity limit condition for the fundamental mode-locking regime and for a full gain recovery since $e^{-2\gamma_1\tau} \simeq 0.01 \ll 1$. Further, time was scaled by κ_1, hence the time unit is 343 fs. The gain bottom Bragg mirror is assumed to be perfectly reflective giving $h_1 = 2$ and for the absorber, $h_2 = 1.9985$ models the presence of non-saturable losses of 3%. Note that $h_1 = 2$ corresponds to a Gires-Tournois interferometer regime [75]. The latter are designed to conserve the photon number using highly reflective bottom mirrors and yield a purely dispersive spectrum [35]. Models based upon DADEs such as equations (5.1)-(5.5) correctly reproduce this unitary, dispersive, response [35].

5.2 MODAL STRUCTURE

As described in section 2.2.3, the modal structure is investigated with the CW ansatz

$$E_i = e_i \exp(-i\omega t), \tag{5.6}$$

$$Y_i = y_i \exp(-i\omega t). \tag{5.7}$$

We scale the time of the VCSEL-RSAM equations (5.1)-(5.5) as $t \to \kappa_1 t$, introduce $\rho = \kappa_1/\kappa_2$, and insert the ansatz (5.6)-(5.7) to obtain

$$e_1 - y_1 = r_g y_1, \tag{5.8}$$

$$e_2 - y_2 = r_a y_2, \tag{5.9}$$

$$y_1 = \eta e^{i\omega t}(e_2 - y_2), \tag{5.10}$$

$$y_2 = \eta e^{i\omega t}(e_1 - y_1), \tag{5.11}$$

where

$$r_a = \frac{h_1}{1 - i\omega - N_1(1 - i\alpha_1)} - 1, \tag{5.12}$$

$$r_g = \frac{h_2}{1 - i\left(\rho\omega + \delta\right) - N_2(1 - i\alpha_2)} - 1 \tag{5.13}$$

are the unsaturated reflectivities of the gain and absorption cavity, respectively. They relate the output field to the injection field as

$$O_1 = E_1 - Y_1 = r_g Y_1, \tag{5.14}$$

$$O_2 = E_2 - Y_2 = r_a Y_2. \tag{5.15}$$

For determining the CW threshold, $N_i = J_i$ holds.

Inserting equation (5.8) into (5.11) and equation (5.9) into (5.10) yields

$$y_1 = \eta \exp(i\omega\tau) r_a y_2, \tag{5.16}$$

$$y_2 = \eta \exp(i\omega\tau) r_g y_1. \tag{5.17}$$

Combining these two equations results in the CW condition

$$r_g r_a \eta^2 \exp(2i\omega\tau) = 1. \tag{5.18}$$

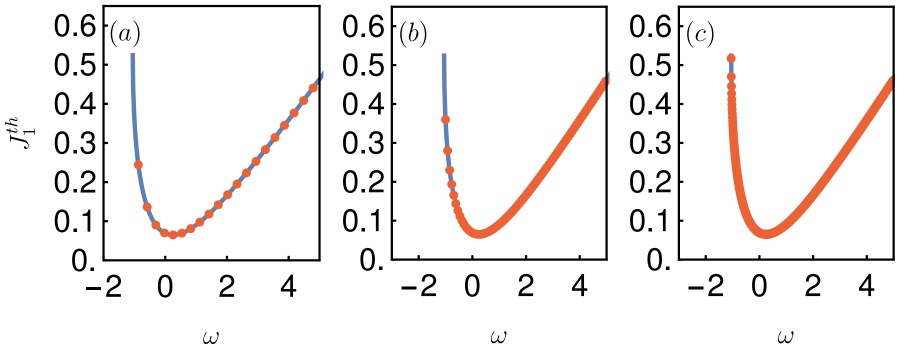

Figure 5.2: Gain value J_1^{th} for which a CW mode with frequency ω emerges from the off solution. If the delay τ is finite, the CW modes are discrete (red points). As the delay increases, the frequency distance between two neighboring modes decreases. Blue lines indicate the long delay limit $\tau \to \infty$. Parameters are $\tau = 10, 40, 500$ for (a), (b) and (c), respectively.

Seperating equation (5.18) into modulus squared and phase gives

$$R_g R_a \eta^4 = 1, \tag{5.19}$$

$$\phi + 2\omega\tau + \mathrm{Arg}[\eta] = 2k\pi, \quad k \in \mathbb{Z}, \tag{5.20}$$

where R_g and R_a are the squared magnitudes of r_g and r_a, respectively, and ϕ is the phase of the product $r_g r_a$.

After some algebra R_g, R_a and ϕ are given by

$$R_g = \frac{(h_1 - 1 + J_1)^2 + (\omega - \alpha_1 J_1)^2}{(1 - J_1)^2 + (\omega - \alpha_1 J_1)^2}, \tag{5.21}$$

$$R_a = \frac{(h_2 - 1 + J_2)^2 + (\rho\omega + \delta - \alpha_2 J_2)^2}{(1 - J_2)^2 + (\rho\omega + \delta - \alpha_2 J_2)^2}, \tag{5.22}$$

$$\begin{aligned}\phi = {} & \arctan\frac{\omega - \alpha_1 J_1}{h_1 - 1 + J_1} + \arctan\frac{\omega - \alpha_1 J_1}{1 - J_1} \\ & + \arctan\frac{\rho\omega + \delta - \alpha_2 J_2}{h_2 - 1 + J_2} + \arctan\frac{\rho\omega + \delta - \alpha_2 J_2}{1 - J_2}.\end{aligned} \tag{5.23}$$

Solving the CW condition given by equation (5.18) exactly leads to infinitely many discrete pairs (J_1^n, ω^n), $n \in \mathbb{N}$, where $\omega^{n+1} - \omega^n \approx \pi/\tau$. The overall CW threshold is the minimum value of all J_1^n values. The values for ω^n become quasi-continuous in the long delay limit. Then it can be assumed that for every J_1 there exists an ω that solves the phase condition (5.20), and only the equation for the absolute value (5.19) remains to be solved.

Figure 5.2 depicts three examples of the gain threshold $J_1^{th}(\omega)$ as a function of the different CW modes existing in the VCSEL-RSAM for increasing delay values. The blue lines indicate the long delay approximation $\tau \to \infty$.

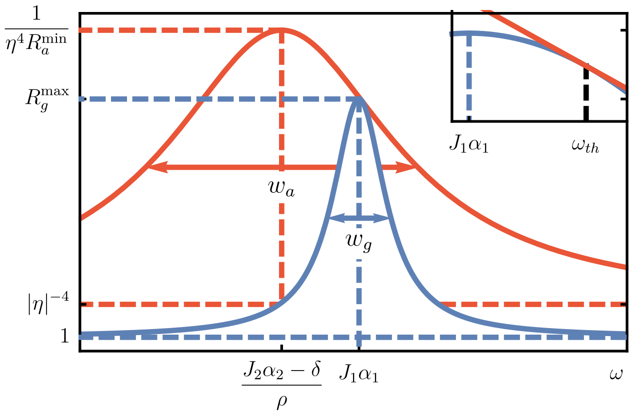

Figure 5.3: Graphical representation for determining the CW threshold frequency. The blue and red lines depict the gain reflectivity R_g and the inverse absorber reflectivity $G_a = (\eta^4 R_a)^{-1}$, respectively. As the gain bias J_1 increases, the CW threshold is reached when both curves intersect for the first time. Inset: Due to the curvature of the inverse absorber reflectivity, the CW frequency ω_{th} is located slightly away from the maximum of the gain reflectivity $J_1\alpha_1$. The other quantities are explained in more detail in the main text.

For an intuitive understanding of the CW modes, it is instructive to characterize the curves that are given by R_g and $G_a = (\eta^4 R_a)^{-1}$, referred to as the gain reflectivity and the inverse absorber reflectivity, respectively. Geometrically and in the long delay limit, the CW threshold is given by the first intersection between the two curves as J_1 increases (cf. figure 5.3).

The limits for G_a and R_g for large frequencies are

$$\lim_{\omega\to\pm\infty} G_a = \eta^{-4}, \tag{5.24}$$

$$\lim_{\omega\to\pm\infty} R_g = 1. \tag{5.25}$$

Equations (5.24)-(5.25) show an essential instability at $\eta = 1$, where an infinite amount of modes emerge as the cavity setup becomes lossless.

The maximums of both curves are located at

$$\omega_g^{\max} = J_1\alpha_1, \tag{5.26}$$

$$\omega_a^{\max} = \frac{J_2\alpha_2 - \delta}{\rho}. \tag{5.27}$$

If the gain curve is narrow compared to the inverse absorber reflectivity curve, the overall CW threshold is close to the gain reflectivity peak (cf. the inset of figure 5.3).

The height at the maximum is given by

$$G_a^{\max} = \frac{1}{\eta^4 R_a^{\min}} = \frac{(1-J_2)^2}{\eta^4(h_2+J_2-1)^2}, \tag{5.28}$$

$$R_g^{\max} = \frac{(h_1+J_1-1)^2}{(1-J_1)^2}. \tag{5.29}$$

As G_a has values between G_a^∞ and $G_a^{\max}$, for the overall CW threshold $J_1^{\text{th}}(\omega_{th})$ it holds that

$$\frac{1+\eta^2-h_1\eta^2}{1+\eta^2} \leq J_1^{\text{th}}(\omega_{th}) \leq \frac{1+(h_1+h_2-h_1h_2-1)\eta^2 - J_2(1+(h_1-1)\eta^2)}{1+(h_2-1)\eta^2+J_2(\eta^2-1)}, \tag{5.30}$$

which can be shown by setting $R_g^{\max}$ equal to G_a^∞ and $G_a^{\max}$ and solving the resulting equation for J_1.

Let the width of a unimodal symmetric curve $R(\omega)$ be defined by the difference between the two solutions of $R(\omega) = \frac{1}{2}\left(R^{\max} - R^{\inf}\right) + R^{\inf}$ with $R^{\max} = \max_\omega R(\omega)$ and $R^{\inf} = \lim_{\omega\to\infty} R(\omega)$. Then the widths of R_g and G_a are

$$w_g = 2(1-J_1), \tag{5.31}$$

$$w_a = \frac{2|h_2-1+J_2|}{\rho}. \tag{5.32}$$

The width of R_g decreases linearly with J_1 and does not depend on any other parameters. On the other hand, the width of G_a depends on h_2 and J_2.

A further important control parameter compared to the MIXSEL system is the detuning δ between the two micro-cavities. It shifts the inversed absorber reflectivity curve G_a by δ/ρ. Therefore, it has a major effect on the overall CW threshold if the gain reflectivity peak is close to the peak of the inversed absorber reflectivity. This relationship between the CW threshold and the detuning is depicted in figure 5.4 (a) and (c) where both J_1^{th} as well as the corresponding CW frequency ω_{th} are shown as a function of the detuning δ.

While J_1^{th} changes continuously with δ, ω_{th} has multiple discontinuities when varying δ. Figure 5.5 shows the different lasing modes that exist as a function of δ. While the frequency of each mode changes continuously with δ, the mode that emerges first from the off solution switches, explaining the discontinuities in the overall threshold frequency. As $\tau \to \infty$, the modes are separated by an infinitesimal amount and the overall CW threshold frequency becoms pseudo-continuous.

For $\rho > 1$ the CW threshold curve has a cusp where the CW frequency has a discontinuity independent of the delay (cf. figure 5.4 (b) and (d)). The cusp can be understood using the graphical representation

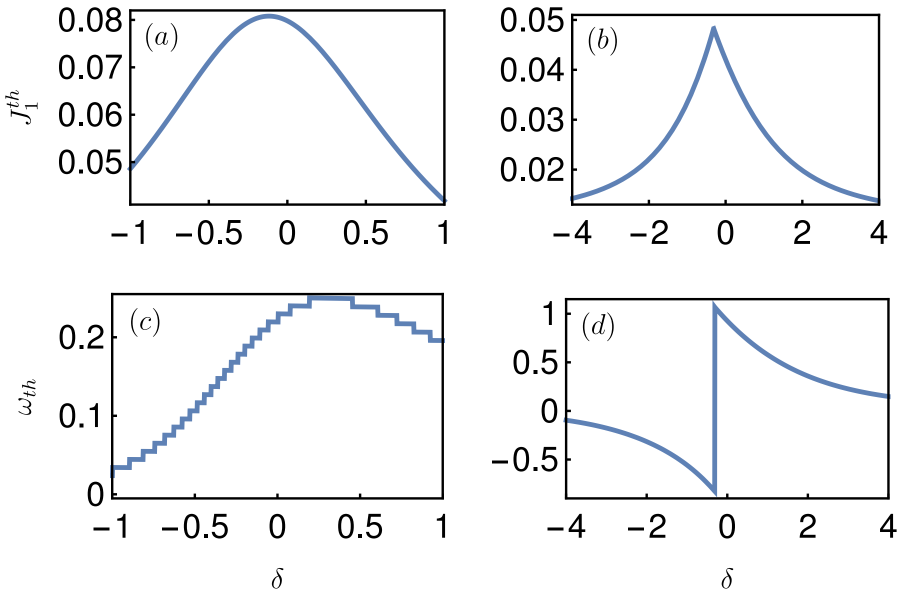

Figure 5.4: Overall gain threshold J_1^{th} (a, b) and the corresponding threshold frequency ω_{th} (c, d) as a function of the detuning δ. Parameters are $(\tau, \rho) = (300, 1/4.2857)$ and $(\tau, \rho) = (10000, 2)$ for the left and right column, respectively.

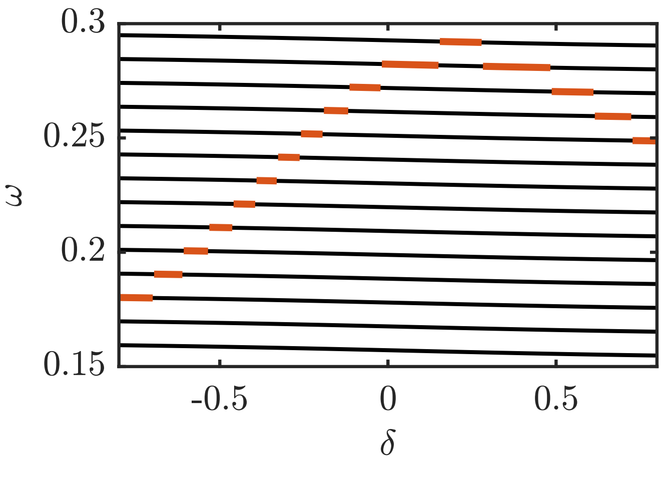

Figure 5.5: The dependence of the CW mode frequency ω on the detuning δ in a VCSEL-RSAM as given by equations (5.1)-(5.5) for $\tau = 300$. While the frequencies of the different CW modes (black lines) change continuously with the detuning, the mode that emerges first from the off solution (thick red line) switches, thereby explaining the discontinuouities seen in figure 5.4 (c).

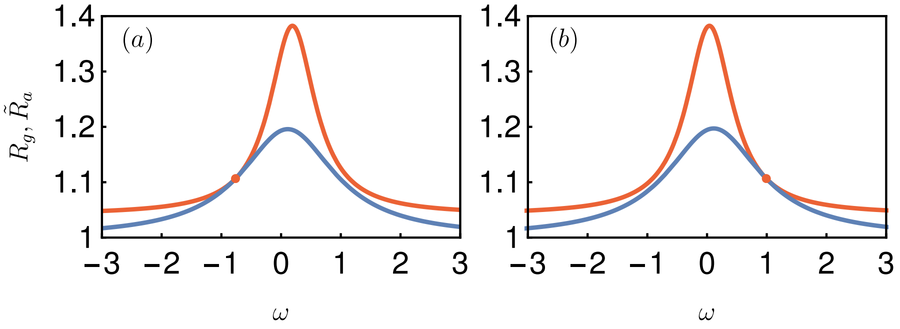

Figure 5.6: Intersections of the gain and inverse absorber reflectivity R_g and G_a as a function of the detuning δ for the kink case $\rho > 1$. The blue line, red line and red point indicate the effective gain reflectivity R_g, the inverse effective absorber reflectivity G_a, and the intersection of the two curves, respectively. Because the absorber curve is narrow compared to the gain curve, the frequency jumps from the left to the right side of the gain curve when the detuning is slightly changed, thereby explaining the discontinuouity seen in figure 5.4 (d). Parameters are $(\rho, \delta) = (2, -0.45)$ and $(\rho, \delta) = (2, -0.15)$ for (a) and (b), respectively.

of the reflectivities as for $\rho > 1$ the inversed absorption curve has comparable width to the gain curve. Therefore, at a particular value of δ, the mode where both curves intersect jumps from the right to the left side of the gain curve (cf. figures 5.6 (a) and (b)). A similar mechanism has been observed experimentally in a semiconductor laser [154].

5.3 WIGGLING INSTABILITY

In the following, we operate in the regime of localization, where the pulses are TLSs that appear below the lasing threshold bias. We denote with $j = J_1/J_{\text{th}}^{\text{max}}$ the gain bias scaled with the maximum value of the threshold for CW emission, i.e. $J_{\text{th}}^{\text{max}} = \max J_{\text{th}}(\delta)$, where $J_{\text{th}}(\delta)$ is the CW threshold depending on δ. In the long delay limit, $J_{\text{th}}(\delta)$ is computed by imposing the round-trip reflectivity of the full system to be unity, i.e. $R(\omega, J_1) = |r_a||r_g|\eta^2$. In the long cavity regime lasing occurs very close to the frequency ω_{max} that maximizes $R(\omega, J_1)$.

The long cavity and the multiscale nature of the problem render the direct numerical simulations particularly tedious. To circumvent this difficulty, we use the functional mapping method (see section 3.1.3) [133]. For all numerical simulations the length of the integration time box in the vicinity of the pulse was set to $t_{\text{box}} = 140\,\text{ps}$ which is 25 the typical pulse width of $\sim 5.5\,\text{ps}$.

The functional mapping method allows us to perform efficient parameter scans for the single TLS regime and we present some of our results in Fig. 5.7. We start with the parameter set yielding a stable pulsating

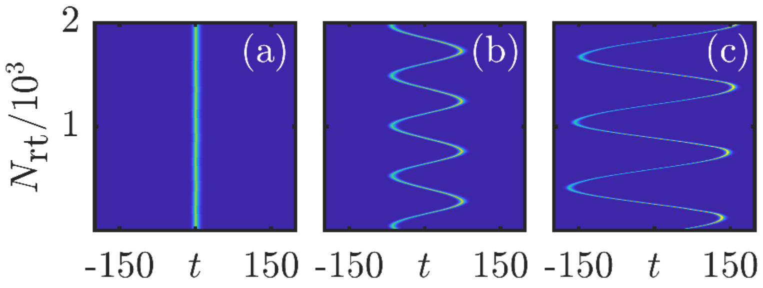

Figure 5.7: Pseudo space-time diagrams for the single pulse train found by direct numerical simulations of equations (5.1)-(5.5). The intensities $|Y_1|^2$ are shown. (a) Stable TLS; (b) Wiggling TLS; (c) The period and the amplitude of the wiggling oscillation strongly increases. Parameters are $\delta = -0.5$ and $j = (0.5406,\ 0.5398,\ 0.5356)$ for (a), (b) and (c), respectively. Reprinted with permission from [34].

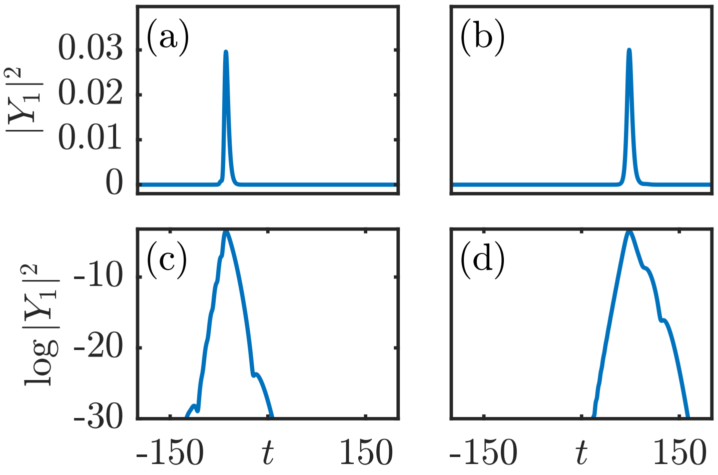

Figure 5.8: Details on the pulse profile in the wiggling regime (linear and logarithmic scales) for the same parameters as in Fig. 5.7(c). Panels (a,c) and (b,d) correspond to the round-trip numbers 47 and 281, respectively. Reprinted with permission from [34].

regime (cf. Fig. 5.1 (b)) and its pseudo space-time representation is presented in Fig. 5.7 (a). There, we used as a folding parameter the exact period of the solution which results in a vertical spatio-temporal trace. As the scaled gain bias j is decreased, keeping all other parameters fixed, the pulse starts to oscillate in its amplitude and position, see Fig.5.7 (b). We refer to these oscillations where the pulse moves back and forth without a net drift as *wiggling*. Remarkably, by further decreasing j, the period and the amplitude of the wiggling oscillations can be made much larger letting j approach a specific value j_{Hom}. Below j_{Hom} only the off solution is stable. The temporal evolution of a TLS with j even closer to j_{Hom} can be seen in Fig. 5.7 (c) where the period and the amplitude of the wiggling is remarkably larger than in panel (b).

It was shown in [35], that the third order dispersion stemming from the lasing micro-cavity induces a train of decaying satellites on the leading edge of the TLSs observed in this system. Due to the nonlinear interaction with carriers, these satellites may get amplified, eventually replacing the parent pulse that would die out. This regime was termed a satellite instability, see Fig. 4(a) in [35]. A similar phenomenon also appears in mode-locked integrated external-cavity surface-emitting lasers, see section 4.2. There, the gain and the absorber share the same micro-cavity, which leads to a somewhat simpler scenario. In the present case, we note that the wiggling oscillations are not stemming from a satellite instability since the parent pulse remains fully merged with its leading satellite, see Fig. 5.8 (a,b), the latter could merely be observed using a logarithmic scale as shown in Fig. 5.8 (c,d). However, since this wiggling instability was also observed in [35] Fig. 4(b), for slightly different parameters than for the satellite instability, we shall conclude that, in all cases, third order dispersion remains at the root of the observed oscillatory motion. Here, the emerging satellites immediately melt within the main pulse which creates an overall, apparent, wiggling motion.

In order to shed further light on the mechanism responsible for the wiggling, we performed a bifurcation analysis of the system (5.1)-(5.5) using the modified version of the continuation tool DDE-BIFTOOL [135] adapted to DADEs.

Figure 5.9 (a) shows the part of a branch of a single TLS, where a maximum of the injected field intensity $|Y_1|^2$ as a function of the scaled gain bias j for the fixed detuning δ slightly smaller than in Fig. 5.7. The TLSs are periodic orbits of the DADEs (5.1)-(5.5) and they emerge in a saddle-node of limit cycles bifurcation at $j = j_F$ (blue circle). The TLSs are unstable over the low power branch (dashed black line) and stable on the upper branch close to the fold if j is increased (solid black line). However, for increasing j, an Andronov-Hopf bifurcation appears at $j = j_T$ (red circle) and a quasi-periodic solution, that corresponds to a wiggling TLS, emerges. Since the path-continuation of quasiperiodic orbits is not possible within DDE-BIFTOOL, we conducted numerical simulations to reconstruct this orbit (red line). Here, the maximum and minimum intensity values per round-trip are represented. One can clearly see that the branch corresponding to wiggling TLSs emerges supercritically and connects two torus bifurcation points. Further increasing j, the high power branch of TLS recovers its stability until $j = j_{\text{th}}$. If the magnitude of $|\delta|$ is increased, the wiggling orbit grows, see Fig.5.9 (b), until its lower part touches the unstable TLS branch. This point $j = j_{\text{Hom}}$ corresponds to a fold of two emerging *homoclinic bifurcations of periodic orbits*. If $|\delta|$ is further increased beyond this point (see Fig.5.9 (c)), the torus orbit splits into two parts, each limited by a homoclinic bifurcation

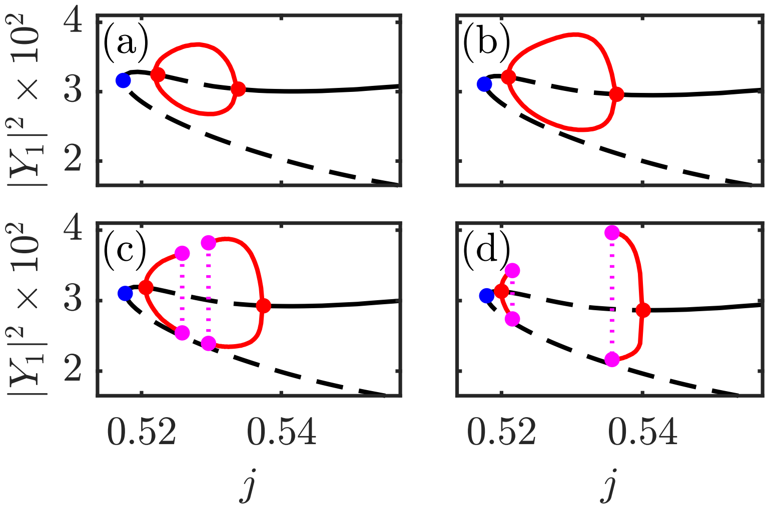

Figure 5.9: The branches of single TLS, showing the peak intensity $|Y_1|^2$ as a function of the normalized gain j for different values of $\delta = (-0.475, -0.485, -0.49, -0.5)$ (a,b,c,d) superposing results from DDE-Bifftool and direct numerical simulations. Solid (dashed) black line corresponds to the stable (unstable) TLS. Blue points mark the folds. The quasi-periodic branch corresponding to wiggling TLSs is in red. As the amplitude of the wiggling grows with δ, the inflating red branch breaks in two parts (c,d) each terminated by a homoclinic bifurcation. Reprinted with permission from [34].

point (magenta circles) and a homoclinic orbit connecting these points, which is schematically depicted in dashed magenta line. Note that in the interval between the two dashed magenta lines, no stable solution exists and the system converges to the off state. For larger values of $|\delta|$, the torus bifurcation points slowly move away from each other along the TLS branch, whereas the homoclinic points are moving towards the j_T points, as presented in Fig.5.9 (d). Now the behaviour observed in Fig. 5.7 becomes feasible: For high gain bias values, a TLS is stable, see Fig.5.9 (d) and Fig. 5.7 (a). Decreasing j, a torus bifurcation sets in at $j = j_T$ and a wiggling TLS occurs (cf. Fig. 5.7 (b)). Further decreasing j one moves along the torus orbit and the oscillation period grows (Fig. 5.7 (c)) and can be arbitrarily large approaching the homoclinic point $j = j_{\mathrm{Hom}}$, where it becomes theoretically infinite.

Finally, in Fig. 5.10 we present a two-parameter study that reveals the interplay between the value of the bias current and the detuning between the two micro-cavities. We depict the pulse energy E of the Y_1 field obtained from direct numerical simulations of equations (5.1)-(5.5) in the (j, δ) plane. Intuitively, one understands that the region of existence of the TLS solutions must be bounded between the threshold line j_{th} (black solid line) – where the (background) off solution becomes unstable – and the fold of period orbits j_F (blue solid line) where the TLS branch emerges. However, studying the stability of the TLS

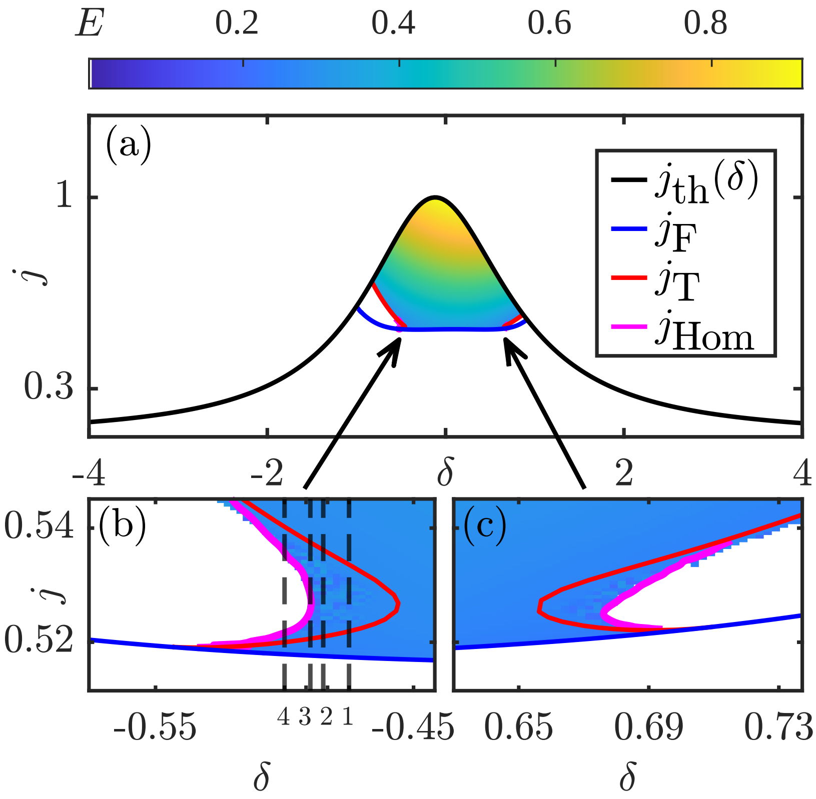

Figure 5.10: (a) Two-parameter bifurcation diagram in the (j, δ) plane together with the pulse energy E of the injected field Y_1 obtained from direct numerical simulations of equations (5.1)-(5.5). (b) and (c): Insets in the vicinity of the left and right co-dimension two point, respectively. Black, blue, red and magenta solid lines indicate the threshold for continuous wave emission j_{th}, the fold of periodic orbits j_F, torus bifurcation line as well as homoclinic bifurcation line of periodic orbits, respectively. Black dashed lines from right to left correspond to the cross-sections depicted in Figs. 5.9 (a)-(d), respectively. Reprinted with permission from [34].

solution imposes more stringent conditions and reveals the importance of the detuning δ. While for small $|\delta|$ the TLS is stable for all bias values between the two aforementioned bordering lines, two unstable regions for both positive and negative detunings appear if $|\delta|$ is increased. There, the onset of stable TLS emission is governed by the torus (red) lines and the homoclinic bifurcations (magenta). Both lines collide at one point in the (j, δ) plane where they meet with the fold line. This point corresponds to a so-called co-dimension two point, which is the analogon of a Bogdanov-Takens bifurcation point found in dynamical systems governed by ordinary differential equations (see section 2.1.6.6). The branches presented in Fig. 5.9 can be seen as four cross-sections of the Fig. 5.15 (b,c) for different δ values, that are indicated by the four dashed black labeled lines; the labels (from right to left) correspond to the panels (a)-(d) of the Fig. 5.9, respectively.

5.4 MASTER EQUATION

In this section, a Haus master equation for the intra-cavity field in the gain section E_1 (as an arbitrary choice instead of E_2) is derived, allowing an intuitive interpretation of the dynamics. The resulting partial differential equation expands the dynamics to third order around the CW threshold.

What follows is the derivation using the functional mapping method (see section 3.3.4). Similarly, a multi-scale analysis (see section 3.3) leads to the same results. For brevity, the multi-scale derivation is attached in appendix C.2.

As a first step, the system's variables are transformed into the co-rotating frame that rotates with the lasing frequency ω_l. For that the ansatzes

$$E_i = e_i e^{-i\omega_l t}, \tag{5.33}$$

$$Y_i = y_i e^{-i\omega_l t} \tag{5.34}$$

are inserted into the equations (5.1)-(5.5) for the VCSEL-RSAM, after which one obtains

$$\epsilon \dot{e}_1 = \left[(1 - i\alpha_1)N_1 - 1 + i\omega_l\right] e_1 + h_1 y_1, \tag{5.35}$$

$$\rho\epsilon \dot{e}_2 = \left[(1 - i\alpha_2)N_2 - 1 + i(\rho\omega_l + \delta)\right] e_2 + h_2 y_2, \tag{5.36}$$

$$y_1(t) = \zeta \left[e_2(t-1) - y_2(t-1)\right], \tag{5.37}$$

$$y_2(t) = \zeta \left[e_1(t-1) - y_1(t-1)\right]. \tag{5.38}$$

Here, the ratio of the photon lifetimes $\rho = \kappa_1/\kappa_2$ and the effective amplitude transmission of the beam splitter $\zeta = \eta e^{i\omega_l \tau}$ were introduced as shorthand notations. Further, time was scaled as $t \to t\tau$ so that the smallness parameter $\epsilon = 1/\tau$ could be introduced.

Let $L_1(\omega)$, $L_2(\omega)$ be defined as

$$L_1(\omega) = -[(1 - i\alpha_1)J_1^{th} - 1 + i(\omega_l + \epsilon\omega)], \tag{5.39}$$

$$L_2(\omega) = -[(1 - i\alpha_2)J_2 - 1 + i(\rho(\omega_l + \epsilon\omega) + \delta)], \tag{5.40}$$

and denote $L_i^0 = L_i(0)$ and $L_i(\omega) = L_i$ for brevity. Introducing L_1 and L_2 into equations (5.35)-(5.38) leads to the condition

$$0 = -L_1(0)e_1 + h_1 y_1, \tag{5.41}$$

$$0 = -L_2(0)e_2 + h_2 y_2, \tag{5.42}$$

$$0 = \zeta[e_2 - y_2] - y_1, \tag{5.43}$$

$$0 = \zeta[e_1 - y_1] - y_2. \tag{5.44}$$

Imposing a singular determinant on equations (5.41)-(5.44) yields the same threshold condition as in section 5.2

$$R(0) = 1, \quad R(\omega) = \xi^2 \frac{h_2 - L_2}{L_2} \frac{h_1 - L_1}{L_1}. \tag{5.45}$$

Next, the carriers are expanded around the CW threshold as

$$N_1 = J_1^{th} + \epsilon^3 n_1, \tag{5.46}$$
$$N_2 = J_2 + \epsilon^3 n_2, \tag{5.47}$$
$$J_1 = J_1^{th} + \epsilon^3 j_1. \tag{5.48}$$

In Fourier space the equations are of the form

$$L_1(\omega) e_1^{(n)} = h_1 y_1^{(n)} + \epsilon^3 \mathcal{N}_1^{(n)}, \tag{5.49}$$
$$L_2(\omega) e_2^{(n)} = h_2 y_2^{(n)} + \epsilon^3 \mathcal{N}_2^{(n)}, \tag{5.50}$$
$$0 = \zeta[e_2^{(n-1)} - y_2^{(n-1)}] - y_1^{(n)}, \tag{5.51}$$
$$0 = \zeta[e_1^{(n-1)} - y_1^{(n-1)}] - y_2^{(n)}, \tag{5.52}$$

where the superscripts indicate the round-tripe number. The nonlinearities $\mathcal{N}_i^{(n)}$ are defined as

$$\mathcal{N}_1^{(n)} = (1 - i\alpha_1)(n_1 e_1)^{(n)}, \tag{5.53}$$
$$\mathcal{N}_2^{(n)} = (1 - i\alpha_2)(n_2 e_2)^{(n)}. \tag{5.54}$$

Now, the injection fields y_i are eliminated from the equations. For that take a linear combination of equations (5.49) and (5.50) to obtain

$$\begin{aligned} h_2 L_1(\omega) e_1^{(n)} + \zeta h_1 L_2(\omega) e_2^{(n-1)} &= h_1 h_2 [y_1^{(n)} + \zeta y_2^{(n-1)}] \\ &\quad + h_2 \epsilon^3 \mathcal{N}_1^{(n)} + \zeta h_1 \epsilon^3 \mathcal{N}_2^{(n-1)}, \end{aligned} \tag{5.55}$$
$$\begin{aligned} h_1 L_2(\omega) e_2^{(n)} + \zeta h_2 L_1(\omega) e_1^{(n-1)} &= h_1 h_2 [y_2^{(n)} + \zeta y_1^{(n-1)}] \\ &\quad + h_1 \epsilon^3 \mathcal{N}_2^{(n)} + \zeta h_2 \epsilon^3 \mathcal{N}_1^{(n-1)}. \end{aligned} \tag{5.56}$$

We rewrite equations (5.51) and (5.52) as

$$y_1^{(n)} + \zeta y_2^{(n-1)} = \zeta e_2^{(n-1)}, \tag{5.57}$$
$$y_2^{(n)} + \zeta y_1^{(n-1)} = \zeta e_1^{(n-1)}, \tag{5.58}$$

and insert these two relationships into equations (5.55) and (5.56), respectively, to get two relationships for $e_i^{(n)}$

$$e_1^{(n)} = \zeta \frac{h_1}{h_2} \frac{h_2 - L_2(\omega)}{L_1(\omega)} e_2^{(n-1)} + \frac{\epsilon^3}{L_1(\omega)} \left[\mathcal{N}_1^{(n)} + \zeta \frac{h_1}{h_2} \mathcal{N}_2^{(n-1)} \right], \tag{5.59}$$
$$e_2^{(n)} = \zeta \frac{h_2}{h_1} \frac{h_1 - L_1(\omega)}{L_2(\omega)} e_1^{(n-1)} + \frac{\epsilon^3}{L_2(\omega)} \left[\mathcal{N}_2^{(n)} + \zeta \frac{h_2}{h_1} \mathcal{N}_1^{(n-1)} \right]. \tag{5.60}$$

For further notational simplicity, the equations are rewritten in matrix form. Define

$$v_n = \begin{pmatrix} e_1^{(n)} \\ e_2^{(n)} \end{pmatrix}, \tag{5.61}$$

$$\Xi(\omega) = \begin{pmatrix} 0 & \zeta \frac{h_1}{h_2} \frac{h_2 - L_2(\omega)}{L_1(\omega)} \\ \zeta \frac{h_2}{h_1} \frac{h_1 - L_1(\omega)}{L_2(\omega)} & 0 \end{pmatrix}, \tag{5.62}$$

$$N_{n,n-1} = \begin{pmatrix} L_1^{-1}(\omega)[\mathcal{N}_1^{(n)} + \zeta \frac{h_1}{h_2} \mathcal{N}_2^{(n-1)}] \\ L_2^{-1}(\omega)[\mathcal{N}_2^{(n)} + \zeta \frac{h_2}{h_1} \mathcal{N}_1^{(n-1)}] \end{pmatrix}. \tag{5.63}$$

Equations (5.59) and (5.60) can then be written as

$$v_n = \Xi(\omega) v_{n-1} + \epsilon^3 N_{n,n-1}. \tag{5.64}$$

The linear part of equation (5.64) defined by $\Xi(\omega)$ is anti-diagonal, i. e., couples e_1 to e_2 and vice versa. By iterating equation (5.64), the linear part can be made diagonal, which results in

$$\begin{aligned} v_n &= \Xi(\omega)[\Xi(\omega) v_{n-2} + \epsilon^3 N_{n-1,n-2}] + \epsilon^3 N_{n,n-1} \\ &= \Xi^2(\omega) v_{n-2} + \epsilon^3 [\Xi(\omega) N_{n-1,n-2} + N_{n,n-1}], \end{aligned} \tag{5.65}$$

where Ξ^2 is given by

$$\Xi^2(\omega) = R(\omega) \begin{pmatrix} 1 & 0 \\ 0 & 1 \end{pmatrix}. \tag{5.66}$$

Until now, equation (5.65) is an exact representation of the dynamics of the VCSEL-RSAM. In order to match it with the assumed PDE, the following two approximations are made:

First, it is assumed that the frequency deviation from the lasing frequency is small so that in the nonlinear term $L_i(\omega)$ can be replaced with L_i^0.

Because the nonlinearity is third order in ϵ, it is consistent to replace the electrical fields that appear in the nonlinearity with a zeroth order approximation as

$$v_n = \Xi v_{n-1} + \mathcal{O}(\epsilon). \tag{5.67}$$

This approximation allows decoupling e_1 and e_2 in the nonlinearity. For this $e_i^{(n-1)}$ in $\mathcal{N}_i^{(n-1)}$ is replaced as given by equation (5.67).

The equation for the electrical field with both approximations reads

$$v_n = \Xi^2(\omega) v_{n-2} + \epsilon^3 \tilde{N}_{n,n-2}, \tag{5.68}$$

with $\tilde{N}_{n,n-2}$ being obtained after simplifications as

$$\tilde{N}_{n,n-2} = \begin{pmatrix} \frac{h_1(1-i\alpha_1)}{L_1^0\left(h_1-L_1^0\right)} n_1^{(n-2)} + \frac{h_2(1-i\alpha_2)}{L_2^0\left(h_2-L_2^0\right)} n_2^{(n-1)} \\ \frac{h_2(1-i\alpha_2)}{L_2^0\left(h_2-L_2^0\right)} n_2^{(n-2)} + \frac{h_1(1-i\alpha_1)}{L_1^0\left(h_1-L_1^0\right)} n_1^{(n-1)} \end{pmatrix} \star v_{n-2}, \tag{5.69}$$

where $\star$ denotes a convolution. Explicitly, for e_1 one can write

$$e_1^{(n)} = R(\omega)\, e_1^{(n-2)} + \left(\frac{h_1\,(1-i\alpha_1)}{L_1^0\,(h_1 - L_1^0)} n_1^{(n-2)} + \frac{h_2\,(1-i\alpha_2)}{L_2^0\,(h_2 - L_2^0)} n_2^{(n-1)} \right) \star e_1^{(n-2)}. \tag{5.70}$$

Assume that a master equation with a linear and nonlinear operator exists that can be written as

$$\partial_\sigma E = \mathcal{L}(\omega) E + \epsilon^3 \mathcal{N}(\sigma, \omega). \tag{5.71}$$

Integrating equation (5.71) over a round-trip, i. e., 2 units of σ, yields

$$E_n = e^{2\mathcal{L}} E_{n-2} + \epsilon^3 \int_{n-2}^{n} e^{(n-\sigma)\mathcal{L}} \mathcal{N}(\sigma, \omega)\, d\sigma, \tag{5.72}$$

where E_n indicates the electrical field at the nth round-trip.

The integral (5.72) can be approximated using an Euler step

$$E_n = e^{2\mathcal{L}} E_{n-2} + 2\epsilon^3 \mathcal{N}(n-2, \omega). \tag{5.73}$$

The final step is the comparison of equation (5.70) obtained from the mapping with equation (5.73) obtained from the assumed PDE. The comparison gives the values of the operator $\mathcal{L}$ and $\mathcal{N}$.

For the linear operator the comparison results in

$$\mathcal{L} = \frac{1}{2} \ln R(\omega). \tag{5.74}$$

For the nonlinear operator the comparison yields

$$\mathcal{N}(n-2, \omega) = \frac{1}{2} \left(\frac{h_1\,(1-i\alpha_1)}{L_1^0\,(h_1 - L_1^0)} n_1^{(n-2)} + \frac{h_2\,(1-i\alpha_2)}{L_2^0\,(h_2 - L_2^0)} n_2^{(n-1)} \right) \star E_1^{(n-2)}. \tag{5.75}$$

Inserting both operators (5.74)-(5.75) into the PDE given by equation (5.71), expanding $\mathcal{L}$ to third order in ϵ and transforming back into time space using $-i\epsilon\omega \rightarrow \partial_z$, reveals the sought PDE as

$$\begin{aligned}\partial_\sigma E &= \left(\sum_{j=1}^{3} d_j \partial_z^j\right) E\left(\sigma, z\right)\\ &+ \frac{1}{2}\left[\frac{h_1\left(1-i\alpha_1\right)}{L_1^0\left(h_1 - L_1^0\right)}\left(N_1 - J_1^{th}\right) + \frac{h_2\left(1-i\alpha_2\right)}{L_2^0\left(h_2 - L_2^0\right)}\left(N_2 - J_2\right)\right] E\left(\sigma, z\right),\end{aligned} \tag{5.76}$$

where equations (5.46)-(5.47) were used to replace n_1 and n_2.

The coefficients d_j are obtained from the Taylor expansion of $\mathcal{L}$ as

$$d_j = \left.\frac{\mathrm{d}\mathcal{L}}{\mathrm{d}\epsilon}\right|_{\epsilon=0} (j!)^{-1}(-i)^{-j}. \tag{5.77}$$

Explicitly, the first three coefficients can be written as

$$\begin{aligned}d_1 &= \frac{h_1}{2(J_1 - 1 + i\omega)(h_1 - 1 + J_1 + i\omega)}\\ &+ \rho\frac{h_2}{2(J_2 - 1 + i(\rho\omega + \delta))(h_2 - 1 + J_2 + i(\rho\omega + \delta)))},\end{aligned} \tag{5.78}$$

$$\begin{aligned}d_2 &= \frac{h_1(h_1 + 2(J_1 - 1 + i\omega))}{4(J_1 - 1 + i\omega)^2(h_1 - 1 + J_1 + i\omega)^2}\\ &+ \rho^2\frac{h_2(h_2 + 2(J_2 - 1 + i(\rho\omega + \delta))}{4(J_2 - 1 + i(\rho\omega + \delta))^2(h_2 - 1 + J_2 + i(\rho\omega + \delta))^2},\end{aligned} \tag{5.79}$$

$$\begin{aligned}d_3 &= \frac{h_1\left(h_1^2 + 3h_1(J_1 - 1 + i\omega) + 3(J_1 - 1 + i\omega)^2\right)}{6(J_1 - 1 + i\omega)^3(h_1 - 1 + J_1 + i\omega)^3}\\ &+ \rho^3\frac{h_2\left(h_2^2 + 3h_2(J_2 - 1 + i(\rho\omega + \delta)) + 3(J_2 - 1 + i(\rho\omega + \delta))^2\right)}{6(J_2 - 1 + i(\rho\omega + \delta))^3(h_2 - 1 + J_2 + i(\rho\omega + \delta))^3}.\end{aligned} \tag{5.80}$$

The approximation of the linear operator $\mathcal{L}$ in equation (5.76) to third order results in an unstable linear operator. Figure 5.11 depicts the real part of the exact linear operator in Fourier space together with its third order approximation where high frequencies are unstable in the approximation. The truncated linear operator's stability is different from the MIXSEL because there the real part of the reflectivity curve is symmetric around the expansion point, ensuring that the expansion to third order results in a stable linear operator.

To obtain a stable linear operator, we insert another smallness parameter $\rho = \kappa_1/\kappa_2$, which corresponds to how broad the absorber reflectivity curve is as compared to the gain reflectivity curve. The absorber reflectivity curve in the limit $\rho \rightarrow 0$ is flat.

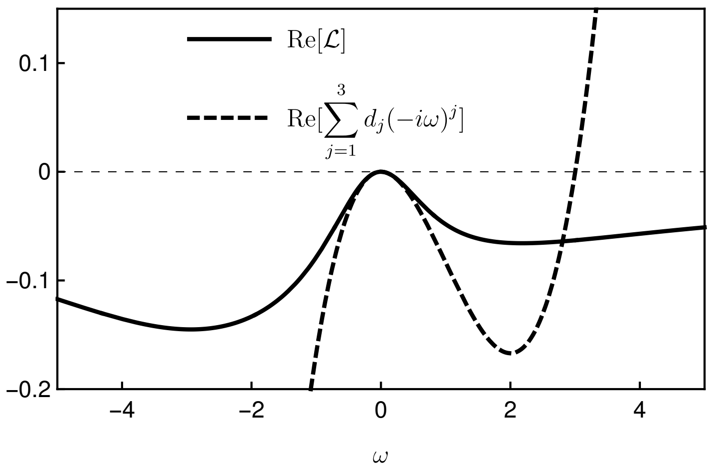

Figure 5.11: Real part of the linear operator $\mathrm{Re}[\mathcal{L}]$ (5.74) in Fourier space (solid line) together with its third order approximation $\mathrm{Re}[\sum_{j=1}^{3} d_j(-i\omega)^j]$ (dashed line). In this case, the third order approximation leads to an operator where the frequencies $\omega \gtrapprox 3$ are unstable.

Two expansions follow: First, the CW threshold is expanded as a function of ρ, i. e.,

$$\omega_{th}(\rho) = \sum_i \epsilon^i \rho^i \left.\frac{\mathrm{d}^i \omega_{th}}{\mathrm{d}\rho^i}\right|_{\rho=0}, \tag{5.81}$$

$$J_1^{th}(\rho) = \sum_i \epsilon^i \rho^i \left.\frac{\mathrm{d}^i J_1^{th}}{\mathrm{d}\rho^i}\right|_{\rho=0}. \tag{5.82}$$

Second, the coefficients d_i from equations (5.78)-(5.80) are expanded in ρ up to the $(3-i)$th order. As ∂_z^i is of ith order, the product $d_i \partial_z^i$ then is of third order.

Inserting the expanded version of ω_{th} and J_1^{th} into the threshold equation $R^2 = 1$, $\frac{\mathrm{d}R^2}{\mathrm{d}\omega} = 0$ produces the expansion terms

$$\omega_0 = \alpha_1 J_{1,0} \tag{5.83}$$

$$J_{1,0} = \frac{1 - \eta^2(h_1 - 1)R_{a,0}}{\eta^2 R_{a,0} + 1} \tag{5.84}$$

$$\omega_0' = -\frac{\eta^2 h_1 \left(\eta^2 \alpha_1^2 J_{1,0} R_{a,0} - \left(\alpha_1^2 + 1\right) J_{1,0} + 1\right)}{\left(\eta^2 R_{a,0} - 1\right)\left(\eta^2 R_{a,0} + 1\right)^2} \frac{dR_{a,0}}{d\delta} \tag{5.85}$$

$$J_{1,0}' = -\frac{\eta^2 \alpha_1 h_1}{\left(\eta^2 R_{a,0} + 1\right)^2} J_{1,0} \frac{dR_{a,0}}{d\delta}, \tag{5.86}$$

where $\omega_0 = \omega_{th}|_{\rho=0}$, $R_{a,0} = R_a|_{\rho=0}$ and $J_{1,0} = J_1^{th}|_{\rho=0}$ are shorthand expressions, and primes indicate the derivative with regard to ρ.

Figure 5.12 shows the CW threshold as a function of ρ together with a constant, linear and quadratic approximation of the threshold.

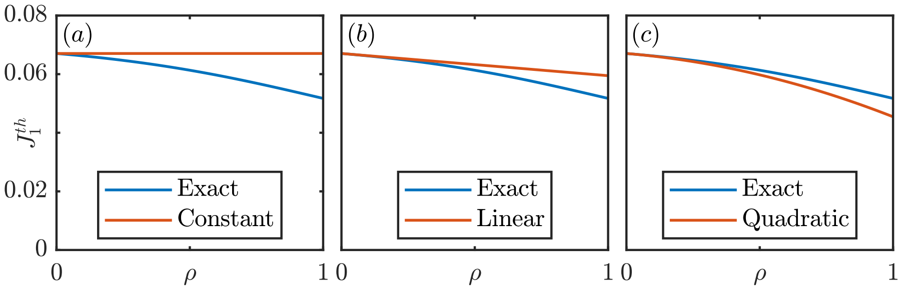

Figure 5.12: A comparison of the exact CW threshold with a constant (a), linear (b) and quadratic approximation (c) as a function of the photon lifetime ratio ρ.

Inserting the approximated CW threshold (5.81)-(5.82) into the coefficients d_i from equations (5.78)-(5.80) and expanding d_i up to the $(3-i)$th order in ϵ yields

$$\begin{aligned} d_1 &= d_1^g + \rho\left(J_1'\frac{\mathrm{d}d_1^g}{\mathrm{d}J_1} - 2i\omega_0' d_2^g + d_1^a\right) \\ &+ \rho^2\left(J_1''\frac{\mathrm{d}d_1^g}{\mathrm{d}J_1} + J_1'^2\frac{\mathrm{d}^2 d_1^g}{\mathrm{d}J_1^2} - 4iJ_1'\omega_0'\frac{\mathrm{d}d_2^g}{\mathrm{d}J_1} - 6\omega_0'^2 d_3^g - 2i\omega_0'' d_2^g\right), \quad (5.87) \\ d_2 &= d_2^g + \rho\left(J_1'\frac{\mathrm{d}d_2^g}{\mathrm{d}J_1} - 3i\omega_0' d_3^g\right), \quad (5.88) \\ d_3 &= d_3^g, \quad (5.89) \end{aligned}$$

where d_i^g indicates the gain coefficients obtained by setting $\rho = 0$ in equations (5.78)-(5.80) and $d_i^a = d_i - d_i^g$. The linear operator given by the new coefficients in the case of a broad absorber gives rise to a stable linear operator.

Note that $\mathrm{Im}[d_2] \neq 0$, which correponds to second order dispersion (or group velocity dispersion), is a critical difference compared to the MIXSEL (see section 4.4) and is one cause for soliton formation in photonic systems [155]. The following section shows how second order dispersion leads to a stabilization of a *super* mode-locked state.

5.5 SUPER MODE-LOCKING

This section investigates the VCSEL-RSAM system for a smaller delay value $\tau = 100\,\mathrm{ps}$, where the mode-locked branches emerge supercritically (as opposed to subcritically in the long cavity regime $\tau \to \infty$). The parameters used are the same as in the previous sections except for $\eta = 0.95$, $J_2 = -0.055$ and $\tau = 100\,\mathrm{ps}$. The value of the round-trip time 2τ is chosen that $e^{-s\gamma_2 2\tau} \ll 1$ while $e^{-\gamma_1 2\tau} = \mathcal{O}(1)$, i. e., only the absorption carriers with $\gamma_2^{-1} = 50\,\mathrm{ps}$ recover to the absorption bias, while the gain carriers with $\gamma_1^{-1} = 800\,\mathrm{ps}$ do not.

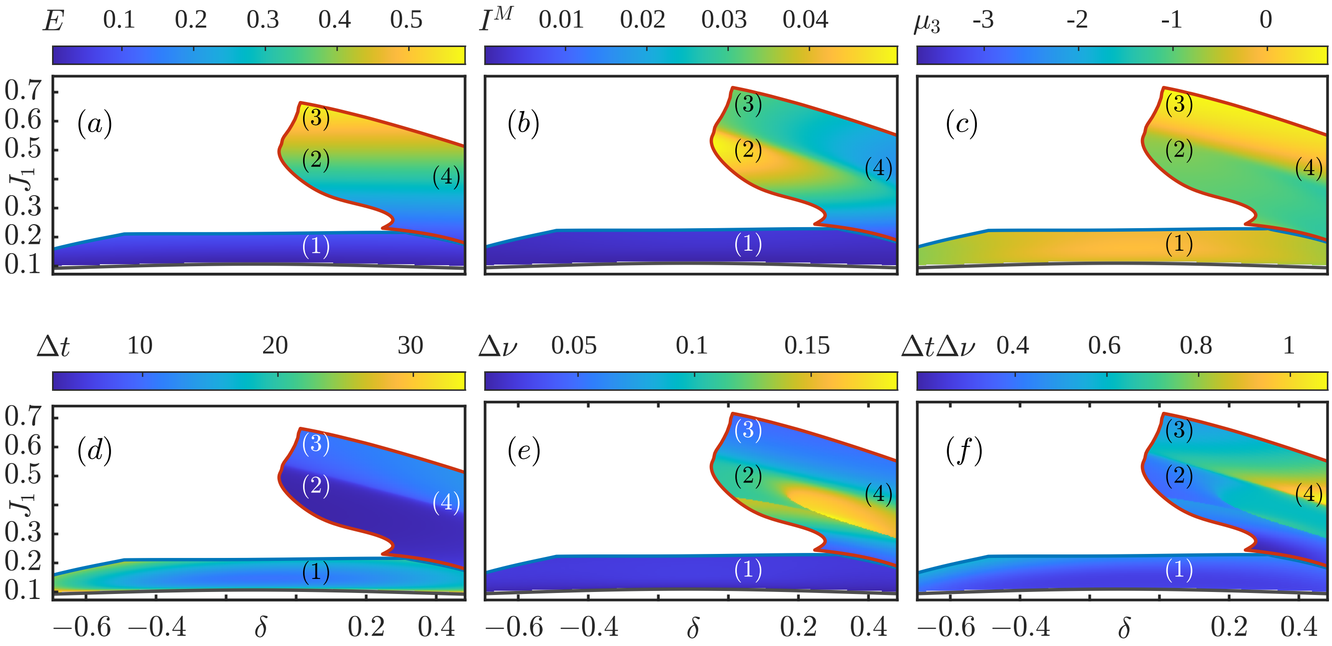

Figure 5.13: Two-dimensional diagrams in the (J_1, δ)-plane showing the region of stable existence of the FML (bounded by a blue curve) and SML (bounded by a red curve) solution obtained by direct numerical simulation of equations (5.1)-(5.5). The color code represents (a) the pulse energy E, (b) the maximum pulse intensity I^M, (c) the skewness of the intensity μ_3, (d) the full width at half maximum Δt, (e) the full width at half maximum of the spectrum $\Delta\nu$ and (f) the product $\Delta t \Delta\nu$. Regions outside the stable FML and SML solution are not shown for clarity. The labels (1)-(4) refer to the corresponding columns in figure 5.14.

In this regime, two different mode-locked solutions appear and might be stable. The first is the typical fundamental mode-locked solution (FML) corresponding to one pulse per period. Additionally, another mode-locked solution becomes stable for higher currents and high enough detuning, referred to as the super mode-locked (SML) solution due to its higher peak power. The region of existence of these two solutions in the (J_1, δ) plane is depicted in figure 5.13 where results from direct numerical simulation are shown. The pulse shape and optical spectrum for four different parameter sets can be seen in figure 5.14. The FML shape and optical spectrum consist of one symmetrical pulse (see fig. 5.14 (a)). We note that this is the case due to non-zero linewidth enhancement factors $(\alpha_1, \alpha_2) = (2.5, 1)$ and that the FML solution has satellites for $\alpha_1 = \alpha_2 = 0$. On the other hand, The SML solution is characterized by either having multiple satellites (cf. fig. 5.14 (b)) or by having a slight asymmetrical pulse shape and spectrum (cf. fig. 5.14 (c) and (d)). Figure 5.13 (c) shows best where the SML solution transitions from having multiple satellites to a single asymmetrical pulse shape. The skewness of the intensity μ_3 in the upper right regions transitions from a negative to a positive value as the SML solution loses its satellites.

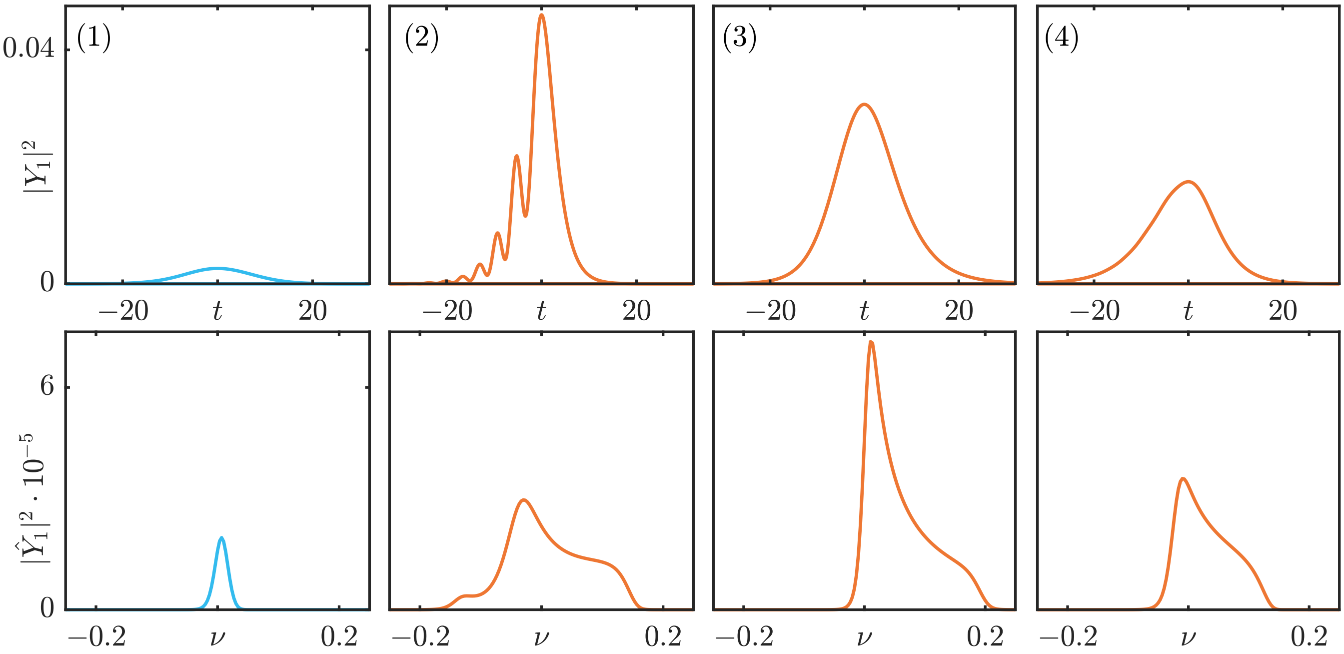

Figure 5.14: The top row depicts the pulse shape $|Y_1|^2$ and the bottom row the corresponding optical spectrum $|\hat{Y}_1|^2$ for the FML (cyan, column (1)) and SML solution (orange, columns (2)-(4)) obtained by direct numerical simulation of equations (5.1)-(5.5). Parameters are $(J_1, \delta) = ((0.165, 0.057), (0.463, 0.057), (0.607, 0.057), (0.405, 0.449))$, for (1)-(4), respectively.

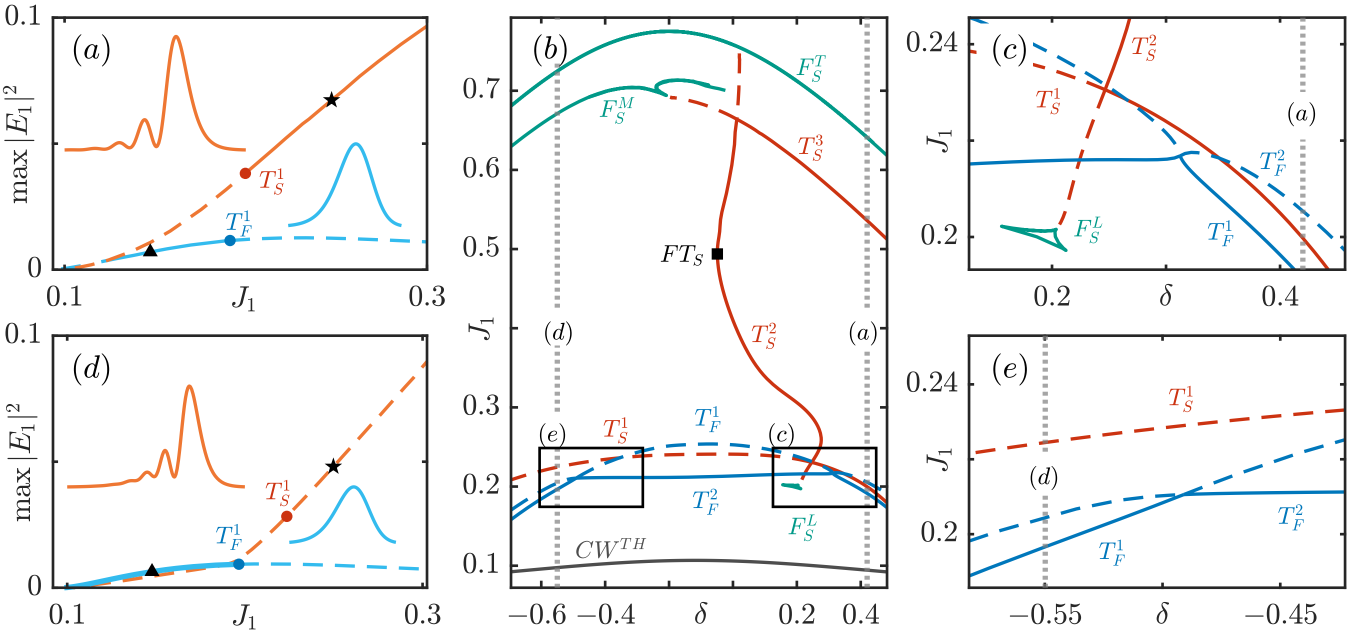

Figure 5.15: (b) Two-parameter bifurcation diagram in the (J_1, δ) plane of equations (5.1)-(5.5). (c) and (e): Insets of (b) in the vicinity of the crossing of torus bifurcation lines on the left and right side, respectively. Red and blue indicate the torus bifurcation lines T_S^1, T_S^2, T_S^3, T_F^1, T_F^2 of the SML (subindex S) and FML (subindex F), respectively. Teal and grey indicate the fold lines F_S^L, F_S^M, F_S^T of the SML and the threshold for continuous wave emission CW^{TH}, respectively. (a) and (d): Branches of the FML (cyan) and SML (orange) solution, showing the peak intensity $\max|E_1|^2$ as a function of the gain bias J_1 for $\delta = 0.42$ and $\delta = -0.55$, respectively. The star and triangle indicate the location of the inset profiles of the SML and FML, respectively. A solid line indicates stability, otherwise dashed.

In order to shed further light on the mechanism responsible for the emergence and stability of the SML solution, a bifurcation analysis of equations (5.1)-(5.5) is performed. Figure 5.15 (a) depicts both the FML and SML branch as a function of the gain bias J_1 for $\delta = 0.42$ together with a profile of the electrical field intensity.

While the FML branch (cf. cyan line in figure 5.15 (a)) loses its stability in the torus bifurcation T_F^1 (blue dot), the originally unstable SML branch (orange) gains stability in the torus bifurcation T_S^1 (red dot) later on. Between these two bifurcations is a region where both FML and SML branches are unstable. Direct numerical simulations indicate that the system behaves aperiodically in the interval between T_F^1 and T_S^1. Figure 5.16 (a) shows a zoom of figure 5.15 (a) together with the results from direct numerical simulations. In addition, figure 5.17 shows the maximum intensity per round-trip for two initial conditions separated by white noise with a standard deviation of 10^{-6} for $J_1 = 0.174$. Both

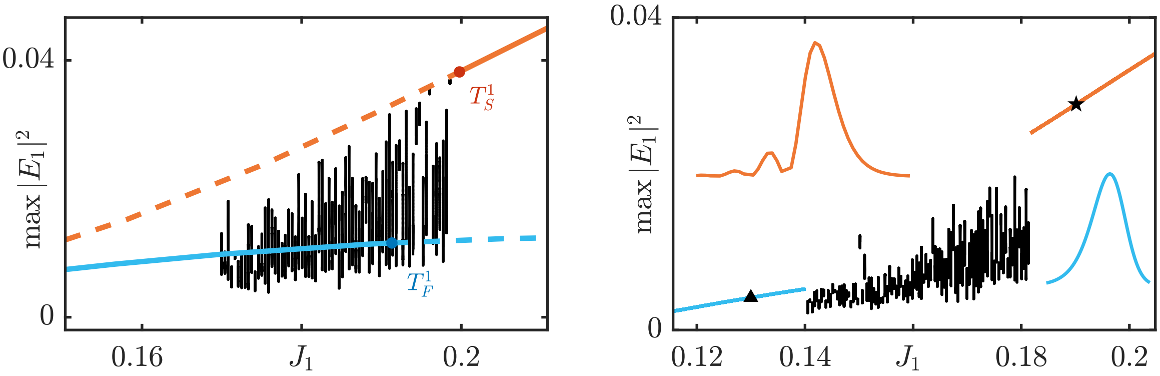

(a) DADE

(b) PDE

Figure 5.16: A comparison of the DADE model (5.1)-(5.5) with the normal form PDE (5.76). (a) For the DADE model, the superposition of results from direct numerical simulations (black points) and path continuation (cyan line: FML solution, orange line: SML solution). (b) Results from direct numerical simulations for the PDE model. Star and triangle indicate the points from the upper left and lower right profile inset, respectively.

initial conditions evolve aperiodically and diverge from each other, hinting at chaos-like dynamics.

For $\delta = -0.55$ the bifurcation scenario for the FML branch is the same (cf. cyan line in figure 5.15 (d)), i. e., it loses its stability in the torus bifurcation T_F^1 (blue dot). However, although the same torus bifurcation T_S^1 (red dot) occurs for the SML branch (orange), the SML branch remains unstable for all gain values. The analysis shows that there exists another torus bifurcation line T_S^2 that limits the region of stability for the SML solution (red line in figure 5.15 (b)). Because of T_S^2, stable SML solutions only exist for $\delta > \delta_{FT} \approx -0.049$ where δ_{FT} is the δ value at the point FT_S (block square in figure 5.15 (b)). For $\delta > \delta_{FT}$ the torus bifurcation T_S^3 (red line in figure 5.15 (b)) limits the region of stable SML solutions further. For the FML branch, the stability is limited by either the torus bifurcation T_1^F or T_2^F, depending on the value of δ (cf. blue lines in figures 5.15 (b), (c) and (e)).

Following the torus bifurcations T_1^S and T_2^S of the SML branch in J_1 and δ shows that the chaos emerges from a crossing of two torus bifurcations. Adding the continuation of the torus bifurcations T_1^F and T_2^F of the FML branch allows for predicting the parameter region where chaotic behavior can be observed numerically. Figure 5.15 (b), (c) and (e) depict the torus bifurcation lines T_S^1, T_S^2, T_S^3, T_F^1, T_F^2 of the SML and FML branches in the (J_1, δ)-plane. In figure 5.15 (c), it is inbetween the stable torus line of the FML (either T_F^1 or T_F^2) and the stable torus line T_S^1 of the SML that the chaotic solution is stable.

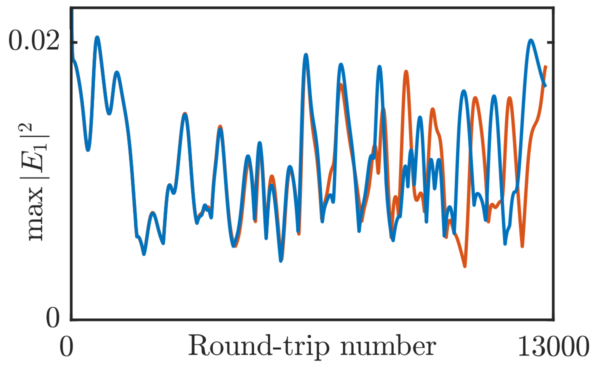

Figure 5.17: Maximum round-trip intensity max$|E_1|^2$ as a function of the round-trip number for two initial conditions separated by white noise with a standard deviation of 10^{-6} for $J_1 = 0.174$.

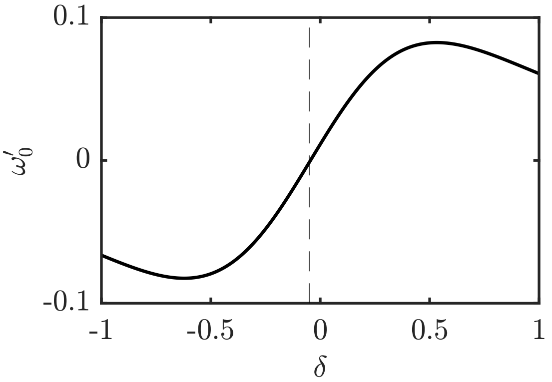

Figure 5.18: First correction of the CW frequency ω_0' as a function of the detuning δ. The vertical dashed line indicates the δ value of the fold of torus lines FT_S in figure 5.15 (b).

The normal form PDE (5.76) shows that it is for $\delta \approx \delta_{FT}$ that the first correction to the CW threshold frequency ω_0' from equation (5.85) changes its sign (cf. figure 5.18). This sign change also results in Im$[d_2]$ changing its sign (see equation (5.88)) and therefore leads to a second order dispersion induced stabilization of the SML branch. We argue that the stabilization is a solitonic effect similar to the dynamics observed in the nonlinear Schroedinger equation, where normal dispersion allows for bright solitons but anomalous dispersion does not [155]. For the MIXSEL d_2 was purely real; hence, SML solutions cannot be observed there.

Further, the PDE predicts all three observed cases: Stable FML, chaos and stable SML (cf. figure 5.16 (b)). The quantitative agreement is good close to the CW threshold, and the PDE shows qualitatively the same behavior observed in the DADE.

The SML and FML branch emerge from two different CW mode as figure 5.19 shows. Due to technical difficulties the mode-locked branches were corrected to the Andronov-Hopf bifurcation with a

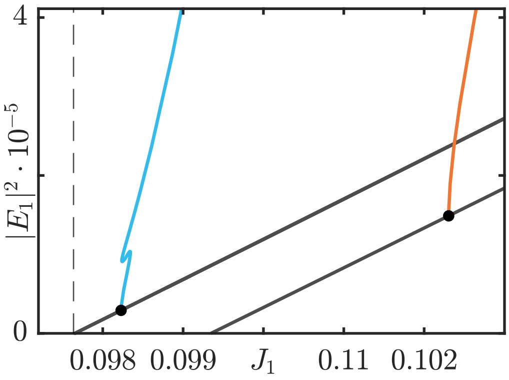

Figure 5.19: Details on the emergence of the FML and SML solutions from two different CW modes. Black, cyan and orange lines indicate CW modes, the FML and SML solution, respectively. Dots and the vertical dashed line mark the Andronov-Hopf bifurcation from which the mode-locked branches emerge and the overall CW threshold, respectively. Parameters are $\delta = -0.55$.

special system condition attached in appendix B.1. The SML branch folds and reconnects with the CW mode at a high gain bias (F_S^T in figure 5.10 (b)). This reconnection was previously observed in a ring laser model in the short cavity regime. For higher delay, the two Andronov-Hopf points, where the mode-locked branch emerges and reconnects from and to the CW, collide, after which the branch detaches from the CW solution [125].

The two-parameter continuation further reveals that the torus curve T_S^2 connects with the upper fold curve F_S^T in a codimension-two Bogdanov-Takens bifurcation. Further, two other fold curves F_S^L and F_S^M exist which are connected to the torus bifurcation lines of the SML solution, i. e., T_S^2 connects with F_S^L and T_S^3 connects with F_S^M in two Bogdanov-Takens bifurcations, see figure 5.15 (b).

6

SUMMARY AND OUTLOOK

In this thesis, the dynamics of coupled optical micro-cavities modeled as delayed algebraic differential equations (DADEs) were investigated using direct numerics and bifurcation analysis. One contribution of this thesis was the implementation of the methods that enable the bifurcation analysis of DADEs [74]. Further, master partial differential equations (PDE) were derived with multi-scale analysis and the functional mapping method, allowing for a more intuitive understanding of the dynamics.

In total, three different mechanisms related to the stability of mode-locked states were discovered: The satellite instability, wiggling and super mode-locking. The corresponding master equations explain all three mechanisms.

The first mechanism is the satellite instability which was investigated by the example of a mode-locked integrated external-cavity surface-emitting laser (MIXSEL) but is also present in other systems [35, 156, 157]. Satellites on the leading edge of pulses, which exist due to third order dispersion stemming from the dispersive micro-cavity, can become unstable when reaching sufficient energy to open a premature net-gain window. With the aid of a first-principle dynamical model based on delay algebraic equations and using a combination of direct time simulations and path-continuation methods we reconstructed the branch of a single pulse solution in the limit of vanishing linewidth enhancement factors as well as long delay and show that the onset of the satellite instability is associated with a global bifurcation of the saddle-node infinite period (SNIPER) type. In the case of non-vanishing linewidth enhancement factors, we showed that the satellite and self-phase modulation instabilities can combine leading to intricate oscillating dynamics. Finally, we derived an approximate dispersive master PDE model by expanding close around the threshold for continuous wave emission and performed a full bifurcation analysis. We demonstrate that this PDE reproduces the satellite as well as the low linewidth enhancement factor SNIPER and Andronov-Hopf bifurcation structure but it becomes increasingly inaccurate at high linewidth enhancement factor values. This is expected, as the normal form derivation assumes parameters close to the threshold for continuous wave emission and small electrical field intensities.

Second, wiggling mode-locked solutions were observed in a model for a vertical cavity surface-emitting laser coupled to a resonant saturable absorber mirror (VCSEL-RSAM). The wiggling results from the interplay between the third order dispersion stemming from the dispersive micro-cavity and their respective detuning. The latter is identified as an experimentally crucial design parameter that defines the range of existence of stable temporal localized states. The wiggling is the result of the interaction between the pulse and its emerging unstable satellites with which the pulse further coalesces thereby creating an apparent wiggling motion that fully explains the results obtained by [35]. Further, the existence of a homoclinic bifurcation of limit cycles was revealed allowing for a controllable tuning of the wiggling oscillation period. Both the satellite and wiggling instability highlight the importance of the DADE modeling approach: As both instabilities are due to third order dispersion, they cannot be observed in models based on the more commonly used delayed differential equations because their dispersive effects are negligible [35].

Third, apart from a conventional fundamental mode-locked state (FML) corresponding to one pulse per period, super mode-locked (SML) pulses were discovered in the model of the VCSEL-RSAM. For low gain, the SML solution has satellites on the leading edge. For higher gain, the SML solution is similar to the FML solution, although the power spectrum is broader than the FML solution and asymmetrical. If the detuning is high enough, a region exists where the SML solution is stable. Bifurcation analysis reveals that the FML and SML solutions emerge from two different CW branches. Further, it was shown that torus bifurcations border the stability of the SML region. The results were confirmed and complemented with direct numerical simulations, which show that a bistable chaos-like region exists between the FML and SML solutions. The master PDE predicts all three dynamical regimes involved in this scenario, i. e., FML, SML and bistable chaos. The threshold value for the existence of the stable SML solution was obtained from the master equation. There the value of the second order dispersion changes its sign as the SML solution first becomes stable.

The results from this thesis give rise to various exciting research directions that fall into three categories: Improving the numerical methods, further exploring the different dynamical regimes, and investigating other related laser systems.

First, regarding the numerical methods, further investigation into the stability computation for periodic orbits is needed. The remeshing procedure tends to allocate most mesh points in the vicinity of the pulse and relatively few points where no pulse is present. This leads to a distorted mesh that is far from equidistant. This, in turn, might

lead to computing spurious Floquet multipliers that are highly dependent on the discretization of the monodromy operator and are not Floquet multipliers of the actual monodromy operator [158]. One direction would be to explore a new criterion for how periodic orbits are remeshed. Another promising direction is exploiting the spectral properties of the pulses in the long-delay limit [159].
Another further improvement would be the implementation of different zero solvers. Although the standard Newton-Raphson method is sufficient in most cases, the radius of convergence can be small, especially for torus bifurcations.
A further research topic could be the heuristic that chooses the number of discretization points for the stability computation of steady states. For the systems investigated here, the maximum imaginary part of the computed eigenvalue set increases with the number of discretization points. Supposing one has a priori information about the stability-changing eigenvalue, the information could be exploited to use the minimally necessary number of discretization points that still resolve the critical eigenvalue.

Second, parts of the dynamical regimes of the MIXSEL and VCSEL-RSAM model systems are yet to be explored. Unexplored regimes include the behavior and bifurcation scenarios of multi-pulse solutions that were left out in this thesis.
Another promising regime in the VCSEL-RSAM system is that of a narrow absorber, i. e., where the photon lifetimes in the gain and absorber section are comparable. The investigation of the modal structure already indicates some novel results for this case.
Further, the transition between the short and long delay limits has yet to be fully explored. It is known from ring laser systems that the mode-locked solution emerges from a supercritical bifurcation in the short delay regime and a subcritical bifurcation in the long delay limit [125]. Preliminary results indicate that this transition also exists in the models for the MIXSEL and VCSEL-RSAM.
It would be interesting to investigate the bifurcation scenario of the satellite instability and the wiggling changes in the short delay limit. The other way around, it might be interesting to see if there are different stable mode-locked states in the long delay limit.
In the future, one might also delve into the effects of the detuning on the Andronov-Hopf bifurcations of the different CW modes in the VCSEL-RSAM.

Third, applying the approach of bifurcation analysis and normal form derivation to closely related systems appears promising. Encouraging candidates are V-shaped setups [160–162] or the Kerr-Gires-Tournouis-interferometer, where this approach has already successfully been used [163].

Experimental results indicate that it might be necessary to include parasitic reflections at the beam splitter to explain certain observations. Including parasitic reflections leads to a modified input-output relation, which correspond to non-local perturbations in the normal form. Finally, the investigations were concerned with the temporal evolution of coupled micro-cavities. A further step is the inclusion of the transverse dynamics, where bifurcation analysis can be carried out with existing continuation software like pde2path [151]. Recent experiments show that for this case spatio-temporal Turing patterns can be observed [164].

A

DEMOS FOR DDE-BIFTOOL

A.1 KERR-GTI

Listing A.1: DDE-BIFTOOL demo demonstrating the DDAE extension on a Kerr-Gires-Tournois interferometer

```
%% DDAE demo - Kerr Gires-Tournois interferometer
% This demo demonstrates using the extension for delay differential
% algebraic equations (DDAE) on a Kerr Gires-Tournois interferometer
% (KGTI). It assumes familiarity with the normal version of DDE-BIFTOOL
% which otherwise can be found in the manual or the other demos.
%
%
% The KGTI is a mono-mode micro-cavity containing a nonlinear Kerr medium
% coupled to a long external feedback cavity under continuous wave (CW)
% injection. The system's equation are given by
%
% $$\left\{
% \begin{array}{l}
% \dot{E}(t) = i (|E(t)|^2 - \delta) E(t) - E(t) + h Y(t) \\
% 0 = \eta [ E(t-\tau) - Y(t-\tau) ] + \sqrt{1-|\eta|^2} Y_0 - Y(t)
% \end{array}\right.$$
%
% where $E$ and $Y$ are the slowly varying electrical field amplitude in
% the micro-cavity and feedback cavity, respectively. The injection field
% is characterized by the injection field amplitude $Y_0$ and the detuning
% $\delta$ with respect to the closest micro-cavity mode. $\eta$ is the
% attenuation factor of the external mirror, $h$ is a coupling factor
% between the micro-cavity and the external cavity and $\tau$ is the
% round-trip time in the external cavity scaled to the photon lifetime.
%
% Both $E$ and $Y$ are complex, i. e. the system's dynamic variables are
% $\Re(E)$, $\Im(E)$, $\Re(Y)$ and $\Im(Y)$ while the other variables
% $\delta$, $h$, $\eta$, $Y_0$ are real parameters and $\tau$ is the
% time delay. Notice that that there is no time derivative in the
% second line, making the system delay algebraic.
%
% The setup is depicted in the figure that follows:
%
% <<kgti.png>>
%
```

```
% At difference with similar models like the Long-Kobayashi model [1] this
% system does not exhibit any phase invariance, as the injection field
% breaks it. For a example of a DDAE system with phase invariance see the
% <../../mixsel_demo/html/mixsel_demo.html MIXSEL demo>. Further, this model
% takes into account multiple reflections in the external cavity.
%
% This demo reproduces figure 4 (a) from [2] showing a branch of continous
% wave solutions in a bistable regime together with a branch of periodic
% orbits connecting the CW branch with itself.
%
% In [2] a singular perturbation approach was used, which replaces the $0$
% in the left hand side of the the system's equation for $Y$ with
% $\epsilon \dot{Y}$ with small $\epsilon$, thereby approximating the
% DDAE system with a delay differential equation.
%
%
% Here the proper DDAE system will be analyzed using the DDAE extension.
% For that the continuation is started at a trivial steady state which is
% then continued to the target parameter set from [2], although with lower
% $\tau$. A lower value of $\tau$ is chosen, because the steady states
% don't depend on the value of $\tau$ and this will make it easier to
% continue the periodic solutions later on.
%
% The resulting steady state is then continued in $Y_0$ showing a region of
% bistability. The stability of the branch is computed to find a Hopf
% bifurcation. Starting from this Hopf bifurcation the emerging periodic
% orbit is continued in $\tau$ to the same value as [2], because as opposed
% to the steady states the periodic orbits depend on the proper value of
% $\tau$.
%
% Finally, the periodic orbit is continued in $Y_0$ showing a snaking
% branch of periodic solutions connecting the branch of steady states with
% itself.
%
% Plotting both branches of steady states and periodic orbits then
% reproduces figure 4 (a) from [2].
%
% References:
%
% [1] Lang, R. and Kobayashi, K. (1980) 'External optical feedback effects
%     on semiconductor injection laser properties,' IEEE journal of quantum
%     electronics, 16(3), pp. 347-355. doi: 10.1109/jqe.1980.1070479.
%
% [2] Schelte, C. et al. (2019) 'Tunable Kerr frequency combs and temporal
%     localized states in time-delayed Gires-Tournois interferometers,'
%     Optics letters, 44(20), pp. 4925-4928. doi: 10.1364/OL.44.004925.
```

```

%% New parameters of DDAE extension
% Using the DDAE extension of DDE-BIFTOOL works just like the normal
% version with two key differences:
%
% * There is a new key in the |set_funcs| function called |'lhs_matrix'|
% with which you can define the left hand mass matrix $M$ of the system
% given by $M \dot{x} = f(x, x_\tau)$.
% In this example |'lhs_matrix'| will be set to |diag([1, 1, 0, 0])| as
% there is a time derivative of the field $\Re(E)$ and $\Im(E)$ but not for
% the field $\Re(Y)$ and $\Im(Y)$.
%
% * There is a new type of collocation implemented for periodic orbits that
% is preffered for the DDAE case and is called Chebychev collocation.
% Chebychev collocation for periodic orbits can be activated by suppling
% the key value pairs |'submesh'|, |'cheb'| and |'collocation_parameters'|,
% |'cheb'| to the |SetupPsol| function. Both options will be used in the
% continuation of periodic orbits below.

%% Load DDE-BIFTOOL and extension into path and initialize the system

% load DDE-BIFTOOL into path
base = [pwd(), '/../../'];
addpath([base, 'ddebiftool/'], ...
        [base, 'ddebiftool_extra_psol/'], ...
        [base, 'ddebiftool_utilities/'], ...
        [base, 'ddebiftool_extra_rotsym/']);

% make parameters accessible by name
% for that define the struct ip, so that ip.<parameter name> will be the
% index number corresponding to the parameter name
parnames = {'delta', 'h', 'eta', 'Y0', 'tau'};
cs = [parnames;num2cell(1:length(parnames))];
ip = struct(cs{:});

% pass the rhs function |kgti_rhs| to |set_funcs| to define the system
% notice the use of |lhs_matrix| to define the equations for $\Re(Y)$ and
% $\Im(Y)$ as delay algebraic
funcs = set_funcs('sys_rhs', @kgti_rhs, ...
                  'sys_tau', @() ip.tau, ...
                  'x_vectorized', true, ...
                  'lhs_matrix', diag([1, 1, 0, 0]));

%% Continuation of trival steady state to parameter set of interest
%

```

```
% start with a trivial steady state and continue it to the parameter set
% used in [2]
start.x = [1; 0; 1; 0];
start.parameter = [1, ...  delta   1
                   1, ...  h       2
                   0, ...  eta     3
                   1, ...  Y0      4
                   1, ...  tau     5
                  ];

figure;
% continue in h
subplot(2, 2, 1);
xlabel('h');
br_h = SetupStst(funcs,'step', 0.1, 'contpar', ip.h,...
                 'x', start.x, 'parameter', start.parameter, ...
                 'max_bound', [ip.h, 2]);
br_h = br_contn(funcs, br_h, 1000);
start = br_h.point(end);

% continue in delta
subplot(2, 2, 2);
xlabel('\delta');
br_delta = SetupStst(funcs, 'step', 0.001, 'contpar', ip.delta, ...
                    'x', start.x, 'parameter', start.parameter, ...
                    'max_bound', [ip.delta, 1.5]);
br_delta = br_contn(funcs, br_delta, 1000);
start = br_delta.point(end);

% continue in eta
subplot(2, 2, 3);
xlabel('\eta');
br_eta = SetupStst(funcs,'step', 0.001,'contpar', ip.eta, ...
                   'x', start.x, 'parameter', start.parameter, ...
                   'max_bound', [ip.eta, 0.5]);
br_eta = br_contn(funcs, br_eta, 1000);
start = br_eta.point(end);

% continue in tau
% here $\tau = 5$ instead of $\tau = 50$ is used, because steady states
% don't depend on the value of $\tau$ and this makes the continuation of
% the periodic orbits below easier.
subplot(2, 2, 4);
xlabel('\tau');
br_tau = SetupStst(funcs, 'step', 0.001, 'contpar', ip.tau, ...
                   'x', start.x, 'parameter', start.parameter, ...
```

```
                   'max_bound', [ip.tau, 5]);
br_tau = br_contn(funcs, br_tau, 1000);
start = br_tau.point(end);

suptitle('continuation of trivial steady state to target parameters');

%% Steady state continuation in Y0
%

% setup branch in Y0
br_stst = SetupStst(funcs, 'step', -0.01, 'contpar', ip.Y0,...
                    'x', start.x, 'parameter', start.parameter, ...
                    'min_bound', [ip.Y0, 0], ...
                    'max_bound', [ip.Y0, 1.2], ...
                    'max_step', [ip.Y0, 1e-2]);

% use (Y0, |E|^2) as the plot measure
xm.field = 'parameter';
xm.subfield = '';
xm.row = 'all';
xm.col = 'all' ;
xm.func = @(p) p(ip.Y0);

ym.field = 'x';
ym.subfield = '';
ym.row = 'all';
ym.col = 'all' ;
ym.func = @(x) x(1)^2 + x(2)^2;

br_stst.method.continuation.plot_measure.x = xm;
br_stst.method.continuation.plot_measure.y = ym;

% continue in Y0
figure;
xlabel('Y_0'); ylabel('|E|^2')
br_stst = br_contn(funcs, br_stst, 1000);
br_stst = br_rvers(br_stst);
br_stst = br_contn(funcs, br_stst, 1000);

title('branch of continous wave steady state solutions');

% compute stability to find bifurcation points (in particular Hopf)
br_stst = br_stabl(funcs, br_stst, 0, 0);
nunst = GetStability(br_stst, 'exclude_trivial', true);

% find bifurcation points by checking number of unstable eigenvalues
```

```
ind_hopf = find(abs(diff(nunst)) == 2);
ind_fold = find(abs(diff(nunst)) == 1);
% if the desired delay of $\tau = 50$ would have already been used above,
% more than two eigenvalues would cross the imaginary axis between
% two steps. The step size would have to be decreased to a unresonably
% small value to seperately detect the Hopf bifurcations.
% As the position of steady states is independent of the delay, only the
% periodic orbits are continued to the correct value of $\tau$.

%% Continuation of periodic orbits
%

% Periodic orbits branching off at Hopf bifurcation of steady states
% notice the use of 'submesh', 'cheb' and 'collocation_parameters', 'cheb'
br_psol_tau = SetupPsol(funcs, br_stst, ind_hopf(1), 'contpar', ip.tau, ...
                        'submesh', 'cheb', ...
                        'collocation_parameters', 'cheb', ...
                        'radius', 0.01, 'degree', 8, 'intervals', 20);
br_psol_tau.method.point.adapt_mesh_after_correct = 1;
br_psol_tau.parameter.max_bound = [ip.tau, 50];

% The periodic solution is continued to a value of $\tau = 50$ first before
% doing the continuation in $Y_0$.
figure;
xlabel('\tau'); ylabel('amplitude');
br_psol_tau = br_contn(funcs, br_psol_tau, 1000);

% Setup branch of periodic solutions to continue in Y0
br_psol = ChangeBranchParameters(funcs, br_psol_tau, ...
                                 length(br_psol_tau.point), ...
                                 'contpar', ip.Y0, 'step', 0.01);

br_psol.parameter.max_step = [ip.Y0, 1e-3];
% stop the continuation if one of the folds is reached:
Y0s_fold = [br_stst.point(ind_fold(1)).parameter(ip.Y0), ...
            br_stst.point(ind_fold(2)).parameter(ip.Y0)];
br_psol.parameter.min_bound = [ip.Y0, min(Y0s_fold)];
br_psol.parameter.max_bound = [ip.Y0, max(Y0s_fold)];

% Continue in Y0 up to lower and upper fold
figure;
xlabel('Y_0'); ylabel('amplitude')

br_psol=br_contn(funcs, br_psol, 400);
br_psol=br_rvers(br_psol);
br_psol=br_contn(funcs, br_psol, 400);
```

```

%% Plot results
xx_stst = br_measr(br_stst, xm);
yy_stst = br_measr(br_stst, ym);

xx_psol = br_measr(br_psol,xm);
% use the helper function |integrate_profile| as the measure for the
% periodic orbits:
yy_psol = arrayfun(@(p) integrate_profile(p), br_psol.point);

figure;
plot(xx_stst, yy_stst, 'k-')
hold on
plot(xx_psol, yy_psol, 'r-')
xlabel('Y_0');
ylabel('<|E|^2>');
xlim([0.3 0.7]);
```

Listing A.2: Right-hand side of the KGTI model.

```
function y = kgti_rhs(x, p)
    E = x(1,1,:) + 1i*x(2,1,:);
    Etau = x(1,2,:) + 1i*x(2,2,:);
    Y = x(3,1,:) + 1i*x(4,1,:);
    Ytau = x(3,2,:) + 1i*x(4,2,:);

    p = num2cell(p);
    [delta, h, eta, Y0] = p{:};

    dE = (-1 + 1i*(abs(E).^2 - delta)).*E + h*Y;
    dY = eta*(Etau - Ytau) + sqrt(1-eta^2)*Y0 - Y;
    y = vertcat(real(dE), imag(dE), real(dY), imag(dY));
end
```

Listing A.3: Helper function that computes the pulse energy of a periodic solution.

```
function y=integrate_profile(point)
    y=0;
    msh=point.mesh;
    EI=point.profile(1,:).^2+point.profile(2,:).^2;
    for ii=1:numel(msh)-1
        y = y+(EI(ii+1)+EI(ii))/2*(msh(ii+1)-msh(ii));
    end
end
```

A.2 MIXSEL

Listing A.4: DDE-BIFTOOL demo demonstrating the DDAE extension on a modelocked integrated external-cavity surface-emitting laser

```
%% DDAE demo - Modelocked integrated external-cavity surface-emitting laser
% This demo demonstrates using the extension for delay differential
% algebraic equations (DDAE) with phase symmetry on a modelocked integrated
% external-cavity surface-emitting laser (MIXSEL). It assumes familiarity
% with the normal version of DDE-BIFTOOL which otherwise can be found in
% the manual or the other demos.
%
% The MIXSEL is a micro-cavity enclosing gain and absorber media coupled to
% a long external feedback cavity. The system's equation are given by
%
% $$\left\{
% \begin{array}{l}
% \dot{E}(t) = ((1 - i\alpha_1) N_1
%              + (1 - i\alpha_2) N_2 - 1) E(t) + h Y(t) \\
% \dot{N_1} = \gamma_1 (J_1 - N_1) - |E|^2 N_1 \\
% \dot{N_2} = \gamma_2 (J_2 - N_2) - s |E|^2 N_2 \\
% 0 = \eta [ E(t-\tau) - Y(t-\tau) ] - Y(t)
% \end{array}\right.$$
%
% where $E$ and $Y$ are the slowly varying electrical field amplitude in
% the micro-cavity and feedback cavity, respectively. $N_1$ and $N_2$
% denote the gain and absorber population inversions, respectively. The
% bias, the recovery time and the line-width enhancement factor are
% $(J_1, \gamma_1, \alpha_1)$ in the gain and $(J_2, \gamma_2, \alpha_2)$
% in the absorber section, respectively. The ratio of the gain and absorber
% saturation intensities is $s$. $\eta$ is the attenuation factor of the
% external mirror, $h$ is a coupling factor between the micro-cavity and
% the external cavity and $\tau$ is the round-trip time in the external
% cavity scaled to the photon lifetime.
%
% Both $E$ and $Y$ are complex, i. e. the system's dynamic variables are
% $\Re(E)$, $\Im(E)$, $\Re(Y)$, $\Im(Y)$, $N_1$ and $N_2$ while the other
% appearing symbols are real parameters where $\tau$ is the time delay.
% Notice that that there is no time derivative in the last line, making the
% system delay algebraic.
%
% The setup is depicted in the figure that follows:
%
% <<mixsel.png>>
%
%
%
```

```
% This demo reproduces the bifurcation analysis part of figure 5 (b), one
% part of a branch of figure 4 (b), and figure 11 (b) from [1]. In contrast
% to [1] the parameter $\eta$ in this demo is kept the same in every figure
% for didactical purposes.
%
% The first two figures show how temporal localized structures depend on
% the gain $J_1$ for $\alpha_1 = 0.02$ and $\alpha_1 = 0$,
% respectively. The third figure shows the transition between those two
% parameter regimes by following a fold of periodic orbits and a torus
% bifurcation in $J_1$ and $\alpha_1$.
%
% The continuation in this demo is structured as follows:
%
% First, a branch of rotating waves is continued in $J_1$ for
% $\alpha_1 = 0.02$ starting from a simple guess and the stability of the
% branch is computed.
%
% Then, the first Hopf-bifurcation is detected, with the goal of
% continueing the emerging (modulated wave) periodic orbit to a regime of
% localized structures with $\tau = 800$. This is done in four steps:
%
% 1. Start the continuation with a few steps in $J_1$. Starting the
% continuation directly with $\tau$ is difficult, because the Hopf line is
% almost vertical in $\tau$.
%
% 2. Change the parameter to $\tau$ and continue until $\tau = 200$ is
% reached. For higher values of $\tau$ it is likely to switch branches by
% accident, if the value of $J_1$ is too high.
%
% 3. Decrease $J_1$ until $J_1 = 0.9 J_1^{th}$ is reached.
%
% 4. Increase $\tau$ to the final value of $\tau = 800$.
%
% Next, the obtained branch is continued in $J_1$ which will result in the
% branch shown in figure 5 (b) from [1].
%
% From there the branch is continued to $\alpha_1 = 0$ where the same
% continuation in $J_1$ is followed through, leading to figure 4 (b) from
% [1]. Further, a fold of periodic orbit continuation is done for one of
% the folds.
%
% The demo concludes with the continuation of a torus bifurcation and
% plotting the obtained branch together with the fold of periodic orbits.
% This the reproduction of figure 11 (b) from [1], although $\eta$ is equal
% to $0.7$ here as in the previous figures and not to $0.9$ as in the
% referenced article.
```

```
%
%
% References:
%
% [1] Schelte, C. et al. (2020) 'Dispersive instabilities in passively
%     mode-locked integrated external-cavity surface-emitting lasers,'
%     Physical review applied, 13(5). doi: 10.1103/physrevapplied.13.054050.
%
% [2] Breda, D. et al. (2006) 'Pseudospectral approximation of eigenvalues
%     of derivative operators with non-local boundary conditions,' Applied
%     Numerical Mathematics, 56(3), pp.318-331.
%     doi:10.1016/j.apnum.2005.04.011.

%% New parameters of DDAE extension
% Using the DDAE extension of DDE-BIFTOOL works just like the normal
% version with two key differences:
%
% * There is a new key in the |set_funcs| function called |'lhs_matrix'|
% with which you can define the left hand mass matrix $M$ of the system
% given by $M \dot{x} = f(x, x_\tau)$.
% In this example |'lhs_matrix'| will be set to |diag([1, 1, 0, 0, 1, 1])|
% as there is a time derivative for the dynamic variables $\Re(E)$ and
% $\Im(E)$, $N_1$ and $N_2$ but not for $\Re(Y)$ and $\Im(Y)$.
%
% * There is a new type of collocation implemented for periodic orbits that
% is preffered for the DDAE case and is called Chebychev collocation.
% Chebychev collocation for periodic orbits can be activated by suppling
% the key value pairs |'submesh'|, |'cheb'| and |'collocation_parameters'|,
% |'cheb'| to the |SetupPsol| function. Both options will be used in the
% continuation of periodic orbits below.

%% Load DDE-BIFTOOL and extension into path and initialize the system

% load DDE-BIFTOOL into path
base=[pwd(),'/../../'];
addpath([base,'ddebiftool/'],...
        [base,'ddebiftool_extra_psol/'],...
        [base,'ddebiftool_utilities/'],...
        [base,'ddebiftool_extra_rotsym/']);


% make parameters accessible by name
% for that define the struct ip, so that ip.<parameter name> will be the
% index number corresponding to the parameter name
parnames={'alpha1', 'alpha2', 'gamma1', 'gamma2', ...
          'J1', 'J2', 's', 'eta', 'h', 'tau', 'omega'};
```

```
cs=[parnames;num2cell(1:length(parnames))];
ip=struct(cs{:});

get_parameter = @(br, name) arrayfun(@(p) p.parameter(ip.(name)), br.point);

% Define the matrix $A$ that generates the rotation as well as the optional
% function $\phi \mapsto \exp(A \phi)$ and pass it to |set_rotfuncs|
% so that the system has the rotational symmetry $\exp(A \phi)$ with anti
% symmetric $A$
Crot = [0, -1; 1, 0];
A = blkdiag(Crot, Crot, 0, 0);

Crotphi = @(phi)[cos(phi), -sin(phi); sin(phi), cos(phi)];
expA = @(phi) blkdiag(Crotphi(phi), Crotphi(phi), 1, 1);

% in this demo the rhs is defined using symbolic functions
% see |generate_mixsel_sym_funcs| for how the sym_funcs are generated.
sfuncs = set_symfuncs(@mixsel_sym_funcs, ...
                     'sys_tau', @() ip.tau, 'p_vectorized', false);

% define the rotational funcs from the symbolic functions
% notice the use of |lhs_matrix| to define the equations for $\Re(Y)$ and
% $\Im(Y)$ as delay algebraic and that we pass |A| and |expA| for the
% rotational symmetry.
rfuncs = set_rotfuncs('sys_rhs',sfuncs.sys_rhs, 'sys_tau', @() ip.tau, ...
                      'sys_dirderi', sfuncs.sys_dirderi, ...
                      'x_vectorized', true, ...
                      'rotation', A, 'exp_rotation', expA, ...
                      'lhs_matrix', diag([1, 1, 0, 0, 1, 1]));

%% Setup initial parameter and state values
% start with low tau (35) and
% J1 slightly above continuous wave threshold (0.68)
% all other parameters are the same as in [1]
par0 = [0.02 0 0.003, 0.1, 0.68, -0.5, 10, 0.7, 2, 35, 0];
% start with a simple guess: small amplitude for E, smaller amplitude for Y
% and N1 and N2 are equal to J1 and J2, respectively.
x0 = [0.01; 0.01; 0.005; 0.005; 0.68; -0.5];

% threshold for continuous wave from analytical derivation
J1_th = 1 - par0(ip.J2) - par0(ip.h)*par0(ip.eta)/(1 + par0(ip.eta));

% define plot measures for live plotting
% parameters
m_tau = df_measr(0, ip.tau, '');
m_J1 = df_measr(0, ip.J1, '');
```

```
m_J1.func = @(J1) J1/J1_th;

m_alpha1 = df_measr(0, ip.alpha1, '');

% intensities for periodic orbits and steady states, respectively
m_max_intensity.field = 'profile';
m_max_intensity.subfield = '';
m_max_intensity.row = 'all';
m_max_intensity.col = 'all' ;
m_max_intensity.func = @(profile) max(sum(profile(1:2, :).^2));

m_intensity.field = 'x';
m_intensity.subfield = '';
m_intensity.row = 'all';
m_intensity.col = 'all' ;
m_intensity.func = @(x) x(1).^2 + x(2).^2;

%% Continue branch of continuous wave emission in J1

% initialize branch for continuation in J1 (and omega)
rw_branch=SetupStst(rfuncs, 'x', x0, 'parameter', par0, ...
                    'contpar', [ip.J1, ip.omega],...
                    'extra_condition', 1, ...
                    'max_step', [ip.J1, 1e-4], 'step', 1e-4, ...
                    'plot_measure', struct('x', m_J1, 'y', m_intensity));

figure;
xlabel('J_1 / J_1^{th}'); ylabel('|E|^2');

rw_branch = br_contn(rfuncs, rw_branch, 750);
rw_branch = br_rvers(rw_branch);
rw_branch = br_contn(rfuncs,rw_branch, 20);
rw_branch = br_rvers(rw_branch);

% compute the stability of the rw_branch using the Breda discretization [2]
% with Chebyshev polynomials. The mesh is adaptively increased until 20
% eigenvalues nearest to 0 are accurate.
[stat_nunst, ~, ~, rw_branch.point] = GetStability(rw_branch, ...
    'funcs', rfuncs, ...
    'exclude_trivial', true, ...
    'pointtype_list', @rot_pointtype_list, ...
    'nearest', 0);

%% Continue emerging periodic orbit to target parameter
%

```

```
% we start the continuation of the periodic orbit from the first Hopf
% bifurcation
ind_hopf = find(diff(stat_nunst) == 2);
ind_hopf = ind_hopf(1);

% our goal is to reach a value of tau = 800
% this is done in four steps:
% - first, continue for a few points in J1
% - then continue to a value of tau = 200, if you go higher one will get
%   problems with switching to another branch by accident.
% - Therefore, once tau = 200 is reached go back in J1 until the value
%   is at 0.9 times cw threshold
% - go higher in tau until the desired value of 800 is reached.
% higher values of tau can be reached the same way. however, it might be
% necessary to repeat this process a couple of this, i. e. increasing tau,
% then decreasing J1 and so on.

% set up the branch of periodic orbits in J1
% note the use of |collocation_parameters|, 'cheb' as well as |submesh|,
% 'cheb'
mw_branch = SetupPsol(rfuncs, rw_branch, ind_hopf,...
    'contpar', [ip.J1 ip.omega], ...
    'dir', ip.J1, ...
    'intervals', 150, ...
    'degree', 5, ...
    'submesh', 'cheb',...
    'collocation_parameters', 'cheb', ...
    'newton_nmon_iterations', 5, ...
    'newton_max_iterations', 50, ...
    'extra_condition', 1, ...
    'matrix','sparse', ...
    'max_step',[], ...
    'max_bound', [ip.J1 1.5*J1_th], ...
    'plot_measure', struct('x', m_J1 ,'y', m_max_intensity));

figure;
subplot(2, 2, 1);
xlabel('J_1 / J_1^{th}'); ylabel('max |E|^2');
mw_branch=br_contn(rfuncs,mw_branch, 50);


% go up in tau
mw_branch = ChangeBranchParameters(rfuncs, mw_branch, ...
    length(mw_branch.point), ...
    'contpar', [ip.tau, ip.omega], ...
    'max_bound', [ip.tau 200], ...
```

```
    'max_step', [ip.tau, 10], ...
    'plot_measure', struct('x', m_tau ,'y', m_max_intensity));

subplot(2, 2, 2);
xlabel('\tau'); ylabel('max |E|^2');
mw_branch =br_contn(rfuncs,mw_branch, 1000);


% go lower in J1
mw_branch = ChangeBranchParameters(rfuncs, mw_branch, ...
    length(mw_branch.point), ...
    'contpar', [ip.J1, ip.omega], ...
    'step', -1e-3, ...
    'max_step', [ip.J1 1e-2], ...
    'min_bound', [ip.J1 0.9*J1_th], ...
    'plot_measure', struct('x', m_J1 ,'y', m_max_intensity));

subplot(2, 2, 3);
xlabel('J_1 / J_1^{th}'); ylabel('max |E|^2');
mw_branch=br_contn(rfuncs, mw_branch, 1000);


% go up in tau again
mw_branch = ChangeBranchParameters(rfuncs, mw_branch, ...
    length(mw_branch.point), ...
    'contpar', [ip.tau, ip.omega], ...
    'max_bound', [ip.tau 800], ...
    'max_step', [ip.tau, 10], ...
    'plot_measure', struct('x', m_tau ,'y', m_max_intensity));

subplot(2, 2, 4);
xlabel('\tau'); ylabel('max |E|^2');
mw_branch =br_contn(rfuncs,mw_branch, 1000);

suptitle('Continuation to temporal localized state regime with long delay')
%% Plot the profile of the localized state
localized_state = mw_branch.point(end);

figure;
plot(localized_state.mesh*localized_state.period, ...
     sum(localized_state.profile(1:2, :).^2));
xlabel('t'); ylabel('|E|^2');
xlim([430 460]);

%% Reproduce figure 5 (b) from [1]

```

```
mw_branch = ChangeBranchParameters(rfuncs, mw_branch, ...
    length(mw_branch.point), ...
    'contpar', [ip.J1, ip.omega], ...
    'step', 1e-3, ...
    'max_step', [ip.J1 1e-2], ...
    'max_bound', [ip.J1 J1_th], ...
    'min_bound', [ip.J1 0], ...
    'plot_measure', struct('x', m_J1 ,'y', m_max_intensity));

figure;
xlabel('J_1 / J_1^{th}'); ylabel('max |E|^2');

mw_branch = br_contn(rfuncs,mw_branch, 200);
mw_branch = br_rvers(mw_branch);
mw_branch = br_contn(rfuncs, mw_branch, 1000);

%% Change to zero alpha1 regime

left_fold_ind = find(islocalmin(get_parameter(mw_branch, 'J1'), ...
                                'MinProminence', 0.01));
close_above_fold_ind = left_fold_ind - 3;

mw_branch_zero_alpha1 = ChangeBranchParameters(rfuncs, mw_branch, ...
    close_above_fold_ind, 'contpar', [ip.alpha1, ip.omega], ...
    'step', -1e-3, ...
    'max_step', [ip.alpha1 1e-3], ...
    'min_bound', [ip.alpha1 0], ...
    'plot_measure', struct('x', m_alpha1 ,'y', m_max_intensity));

figure;
ylim([0 0.3]);
xlabel('\alpha_1'); ylabel('max |E|^2');
mw_branch_zero_alpha1 = br_contn(rfuncs, mw_branch_zero_alpha1, 500);

%% Reproduce figure 4 (b) from [1]
mw_branch_zero_alpha1 = ChangeBranchParameters(rfuncs, ...
     mw_branch_zero_alpha1, ...
     length(mw_branch_zero_alpha1.point), ...
    'contpar', [ip.J1, ip.omega], ...
    'step', 1e-3, ...
    'max_step', [ip.J1 5e-3], ...
    'max_bound', [ip.J1 0.95*J1_th], ...
    'min_bound', [ip.J1 0], ...
    'plot_measure', struct('x', m_J1 ,'y', m_max_intensity));

figure;
```

```
xlabel('J_1'); ylabel('max |E|^2');
mw_branch_zero_alpha1 = br_contn(rfuncs,mw_branch_zero_alpha1, 250);
mw_branch_zero_alpha1 = br_rvers(mw_branch_zero_alpha1);
mw_branch_zero_alpha1 = br_contn(rfuncs, mw_branch_zero_alpha1, 250);


%% Reproduce figure 11 (b) - modulated wave fold and torus continuation
%

right_fold_ind = find(islocalmax(get_parameter(mw_branch_zero_alpha1, 'J1')));

% continue the fold of periodic orbits
[pofoldfuncs,pofold,suc]=SetupMWFold(rfuncs, ...
            mw_branch_zero_alpha1, right_fold_ind, ...
            'contpar', [ip.J1 ip.alpha1 ip.omega], ...
            'dir',ip.alpha1, 'step', 0.0025, ...
            'min_bound', [ip.alpha1 0], ...
            'max_step',[ip.alpha1 5e-3; ip.J1 1e-4], ...
            'plot_measure', struct('x', m_J1, 'y', m_alpha1));

figure;
xlabel('J_1 / J_1^{th}'); ylabel('\alpha_1');
pofold = br_contn(pofoldfuncs, pofold,  50);

% continue torus bifurcation next
% for that determine the number of unstable Floquet multipliers first
[po_nunst, ~, ~, mw_branch.point] = GetStability(mw_branch, ...
    'funcs', rfuncs, ...
    'exclude_trivial', true, ...
    'pointtype_list', @rot_pointtype_list);

% normally, one would detect the torus bifurcation with
% torus_ind = find(diff(po_nunst) == 2);
% but here fold and torus bifurcation are so close to each other
% that the last point with 2 unstable multipliers is chosen
[trfuncs, tr_branch] = SetupMWTorusBifurcation(rfuncs, ...
    mw_branch,...
    find(po_nunst == 2, 1, 'last'), ...
    'contpar',[ip.J1, ip.alpha1, ip.omega], ...
    'dir', ip.J1, ...
    'step', -0.001, ...
    'max_bound', [ip.alpha1 0.05], ...
    'max_step', [ip.alpha1 0.002, ip.J1 0.001], ...
    'plot_measure', struct('x', m_J1, 'y', m_alpha1));

figure;
```

```
xlabel('J_1 / J_1^{th}'); ylabel('\alpha_1');

tr_branch = br_contn(trfuncs, tr_branch, 30);
tr_branch = br_rvers(tr_branch);
tr_branch = br_contn(trfuncs, tr_branch, 100);

% Plot fold of periodic orbits and torus bifurcation in one diagram
figure; hold on;
xlabel('J_1 / J_1^{th}'); ylabel('\alpha1');
plot(get_parameter(pofold, 'J1'), get_parameter(pofold, 'alpha1'));
plot(get_parameter(tr_branch, 'J1'), get_parameter(tr_branch, 'alpha1'));
ylim([0 0.05]);
legend('PO Fold', 'Torus', 'Location', 'NorthWest');
```

Listing A.5: The script generating the right-hand side of the MIXSEL system.

```
%% Clear working space, make sure biftool is in path.
clear
base=[pwd(),'/../../'];
addpath([base,'ddebiftool'],[base,'ddebiftool_extra_symbolic']);
if dde_isoctave()
    pkg load symbolic
end

%% create parameter names as strings
parnames={'alpha1', 'alpha2', 'gamma1', 'gamma2', ...
          'J1', 'J2', 's', 'eta', 'h', 'tau'};
% Create symbols for parameters, states and delayed states
% The array |par| is the array of symbols in the same order as parnames.
% Due to the following two lines we may, for example, use either tau or
% par(4) to refer to the delay.
syms(parnames{:});       % create symbols for parameters
par=cell2sym(parnames);  % now a is par(1), tau is par(4) etc.
for i=1:length(parnames)
    assume(par(i),'real');
end

% create symbols for E(t) E(t-tau), Y(t), Y(t-tau)
syms Er Ei Ertau Eitau Yr Yi Yrtau Yitau n1 n2 n1tau n2tau

% define dynamic variables
E=Er+1i*Ei;
Etau=Ertau+1i*Eitau;
Y=Yr+1i*Yi;
Ytau=Yrtau+1i*Yitau;
% define rhs
dE_dt=((1-1j*alpha1)*n1+(1-1j*alpha2)*n2-1)*E+h*Y;
```

```
Y_a=eta*(Etau-Ytau)-Y;
dn1_dt=real(gamma1*(J1-n1)-conj(E)*E*n1);
dn2_dt=real(gamma2*(J2-n2)-s*conj(E)*E*n2);

% split rhs in real and imaginary part
dEr_dt=real(dE_dt);
dEi_dt=imag(dE_dt);
Yr_a=real(Y_a);
Yi_a=imag(Y_a);

%% Differentiate and generate code, exporting it to mixsel_sym_funcs
[fstr,derivs]=dde_sym2funcs(...
    ... % n x 1 array of derivative symbolic expressions
    [dEr_dt;dEi_dt;Yr_a;Yi_a;dn1_dt;dn2_dt], ...
    ... % n x (ntau+1) array of symbols for states (current & delayed)
    [Er,Ertau; Ei,Eitau; Yr,Yrtau; Yi,Yitau; n1, n1tau; n2, n2tau],...
    ... % 1 x np (or np x 1) array of symbols used for parameters
    par, ...
    ... % optional argument specifying output file
    'filename','mixsel_sym_funcs', ...
    'directional_derivative', true, ...
    'maxorder', 2);
```

B

CODE SAMPLES

B.1 sys_cond FOR CW ANDRONOV-HOPF CORRECTION

Listing B.1: sys_cond for CW Andronov-Hopf correction

```
function [res, cond] = sys_cond_cw_andronov_hopf(p)
    if strcmp(p.kind, 'psol')
        p.parameter(15) = 0;
        IE1 = sum(p.profile(1:2, :).^2);
        E_re = p.profile(1, :);
        E_im = p.profile(2, :);
        % https://en.wikipedia.org/wiki/Smooth_maximum
        alpha = 1e6;
        S_alpha = nan;
        while(isnan(S_alpha))
            S_alpha = sum(IE1.*exp(alpha*IE1)) / ...
                      sum(exp(alpha*IE1));
            grad_S_alpha = exp(alpha*IE1) / ...
                           sum(exp(alpha*IE1)) .* ...
                           (1 + alpha*(IE1 - S_alpha));
            alpha = alpha/10;
        end

        res(1) = S_alpha - mean(IE1);
        cond(1) = p_axpy(0 , p, []);
        cond(1).profile(1, :) = 2*E_re.*grad_S_alpha ...
                              - 2*E_re/size(p.profile, 2);
        cond(1).profile(2, :) = 2*E_im.*grad_S_alpha ...
                              - 2*E_im/size(p.profile, 2);
        cond(1).parameter(15) = 0;

        res(1) = res(1)*10.^3;
        cond(1).profile(1, :) = cond(1).profile(1, :)*10.^3;

    else
        error('SYS_COND: point is not psol.');
    end
end
```

C

MULTI-SCALE NORMAL FORM DERIVATION

The results presented in section C.1 have been published in

[33] C. Schelte, D. Hessel, J. Javaloyes and S. V. Gurevich. "Dispersive Instabilities in Passively Mode-Locked Integrated External-Cavity Surface-Emitting Lasers." In: *Physical Review Applied* 13 (2020), p. 054050.

The results presented in section C.2 are in preparation for submission:

[152] D. Hessel, S. V. Gurevich and J. Javaloyes. "Super mode-locking in passively mode-locked vertical external-cavity surface-emitting lasers." *(in preparation)*.

C.1 MIXSEL

We consider in this appendix the derivation of the PDE Eq. (4.32) by the use of multi-scale analysis. Our starting point is Eqs. (4.6)-(4.7) and, for the sake of simplicity, we set $\alpha_j = 0$ and assume that η is real. It is also convenient for our analysis to transform the DADE system as given by Eqs. (4.6)-(4.7) into a neutral differential delay equation (NDDE) reading

$$\begin{aligned}\varepsilon\left[\frac{dE}{d\sigma}(\sigma)+\eta\frac{dE}{d\sigma}(\sigma-1)\right] &= \left[(N_1+N_2)E\right](\sigma)-E(\sigma)\\ &\quad+\eta\left[(N_1+N_2)E\right](\sigma-1)\\ &\quad+(h-1)\eta E(\sigma-1)\,. \end{aligned} \tag{C.1}$$

We can define small deviations of the carriers as

$$N_j = J_j + \varepsilon^3 n_j \tag{C.2}$$

with $j \in [1,2]$ and scale the field, for convenience, as $E = \varepsilon^{\frac{3}{2}} A$. Inserting these scaling relations in Eq. (C.1), we find

$$A(\sigma) = \eta\frac{h-1+N_t}{1-N_t}A(\sigma-1)+\frac{\varepsilon^3\bar{N}-\varepsilon\bar{L}}{1-N_t}, \tag{C.3}$$

with $N_t = J_1 + J_2$ the threshold inversion given in Eq. (4.15) and the filtering $\bar{\mathcal{L}}$ and nonlinear operator $\bar{\mathcal{N}}$ defined by

$$\begin{aligned}\bar{\mathcal{L}} &= \frac{d}{d\sigma}\left[A(\sigma)+\eta A(\sigma-1)\right], & \text{(C.4)}\\ \bar{\mathcal{N}} &= (nA)(\sigma)+\eta(nA)(\sigma-1)\,. & \text{(C.5)}\end{aligned}$$

We can now use the definition of threshold given in Eq. (4.15) to find the system upon which one can perform the multi-scale analysis

$$A\left(\sigma\right)=A\left(\sigma-1\right)+\frac{1+\eta}{h\eta}\left(\varepsilon^{3}\bar{N}-\varepsilon\bar{L}\right). \tag{C.6}$$

By inspecting Equation (C.6), one notices that the solutions are weakly perturbed period one (P1) orbits. Because we assume that the nonlinear term scales as ε^3, we can safely restrict our analysis to the multi-scale analysis on the linear part of Eq. (C.6), that is

$$A\left(\sigma\right)=A\left(\sigma-1\right)-\tilde{\varepsilon}\frac{d}{d\sigma}\left[A\left(\sigma\right)+\eta A\left(\sigma-1\right)\right], \tag{C.7}$$

where we defined the short-hand $\tilde{\varepsilon}=\varepsilon\left(1+\eta\right)/\left(h\eta\right)$. The linear NDDE as given by Eq. (C.7) only depends on one parameter, which are the cavity losses, and the smallness parameter. It is also an excellent toy model to test various multi-scale schemes. Notice that such a linear NDDE can be solved in the Fourier domain directly. We, however, solve the dynamics by defining a multi-scale expansion. The fast time is $\sigma_0=\sigma/T$ with T the natural period of the solution. The period T shall be close to unity and its deviation leads to the slow drift in the PDE representation. We set $T=1+\tilde{\varepsilon}a$ where a can be chosen to cancel resonant terms in the multi-scale expansion at first order. This approach avoids introducing altogether the intermediate time scale $\sigma_1=\varepsilon\sigma$ (as explained and exemplified in sections 3.3.1-3.3.3). However, one can also analytically find the period of the solution using the functional mapping method which yields $a=1+\eta$. Finally, we define the slow times $\sigma_2=\tilde{\varepsilon}^2\sigma$ and $\sigma_3=\tilde{\varepsilon}^3\sigma$ in order to take into account the effect of nonlinearity, diffusion and third order dispersion. The chain rule yields

$$\frac{d}{d\sigma}=\frac{1}{T}\frac{\partial}{\partial\sigma_0}+\tilde{\varepsilon}^2\frac{\partial}{\partial\sigma_2}+\tilde{\varepsilon}^3\frac{\partial}{\partial\sigma_3}, \tag{C.8}$$

while for the conjugated Fourier variables, we have

$$\omega_\sigma=\frac{1}{T}\omega_0+\tilde{\varepsilon}^2\omega_2+\tilde{\varepsilon}^3\omega_3. \tag{C.9}$$

We expand the solution as

$$A\left(\sigma_0,\sigma_2,\sigma_3\right)=\sum_{j=0}^{\infty}\varepsilon^j A_j\left(\sigma_0,\sigma_2,\sigma_3\right). \tag{C.10}$$

The various solvability conditions lead to several conditions of the form $\bar{L}\tilde{A}\left(\omega_0,\omega_2,\omega_3\right)=0$ where $\tilde{A}\left(\omega_0,\omega_2,\omega_3\right)$ is the (triple) Fourier transform of $A\left(\sigma_0,\sigma_2,\sigma_3\right)$. The expression of $\bar{L}$ is

$$\bar{L}\left(\omega_\sigma\right)=\exp\left(i\omega_\sigma\right)-1+i\tilde{\varepsilon}\omega_\sigma\left[1+\eta\exp\left(i\omega_\sigma\right)\right]. \tag{C.11}$$

The zeroth order operator reads naturally

$$\bar{L}_0 = e^{i\omega_0} - 1, \tag{C.12}$$

hence showing that P1 solutions on the fast scale σ_0, i.e. $A_0\left(\sigma_0 - 1, \sigma_2, \sigma_3\right) = A_0\left(\sigma_0, \sigma_2, \sigma_3\right)$, belong to the kernel of $\bar{L}_0$. The first order solvability is trivially solved since $\bar{L}_1 = 0$ due to our adequate choice of the period T. The other operators found at second and third order are more complex, yet they simplify when acting on P1 solutions to

$$\bar{L}_2 = \left(\eta^2 - 1\right)\omega_0^2 + 2i\omega_2, \tag{C.13}$$

$$\bar{L}_3 = -i\frac{\eta^3+1}{3}\omega_0^3 - \frac{\eta-1}{2}\left(\eta+1\right)^2\omega_0^2 + i\omega_3. \tag{C.14}$$

One can then build the conjugated variable to the slow time ω_ξ as

$$\omega_\xi = \left(\frac{1}{T} - 1\right)\omega_0 + \omega_2\tilde{\varepsilon}^2 + \omega_3\tilde{\varepsilon}^3. \tag{C.15}$$

We note that adding the $-\omega_0$ corresponds to the stroboscopic effect that transforms a T-periodic solution into a slowly drifting steady state from one round-trip to the other. Upon simplification, we find

$$-i\omega_\xi = i\left(1+\eta\right)\tilde{\omega} + \frac{\eta^2-1}{2}\tilde{\omega}^2 - i\frac{\eta^3+1}{3}\tilde{\omega}^3 + \mathcal{O}\left(\varepsilon\right), \tag{C.16}$$

where we defined $\tilde{\varepsilon}\omega_0 = \tilde{\omega}$. Using the definition of $\tilde{\varepsilon}$ and going back to the original variable, i.e., $\varepsilon\omega_0 \to \omega$, gives the following expression for the slow evolution

$$\omega_\xi = d_1\omega - id_2\omega^2 - d_3\omega^3 \tag{C.17}$$

with the coefficients d_j defined in Eq. (4.32). Finally, using that $-i\omega \to \partial_z$ we get

$$\partial_\xi = d_1\partial_z + d_2\partial_z^2 + d_3\partial_z^3. \tag{C.18}$$

As we assumed that the nonlinear term scales as ε^3, it can simply be added to the highest order solvability condition found for the operator $\bar{L}_3$. By using that the carriers are also P1 solutions on the fast time scale (σ_0), we get that $\left(n_jA\right)\left(\sigma_0 - 1, \sigma_2, \sigma_3\right) = \left(n_jA\right)\left(\sigma_0, \sigma_2, \sigma_3\right)$ with $j \in [1,2]$, which allows finding the PDE in the main text.

C.2 VCSEL-RSAM

In this section, the multi-scale analysis is used to derive a normal form PDE to third order for the VCSEL-RSAM (5.1)-(5.5). After rewriting the system's equations in matrix form as a neutral delayed differential equation, the approach from section 3.3 is followed.

We shift the time of the absorber's variables by τ relative to the variables of the gain. Thereby, the variables of both cavities are aligned, and one obtains

$$\epsilon\dot{E}_1 = \tilde{f}_1 E_1 + h_1 Y_1 = \tilde{f}_1 E_1 + h_1\eta E_2 - h_1\eta Y_2 \tag{C.19}$$

$$\rho\epsilon\dot{E}_2 = f_2 E_2 + h_2 Y_2 = f_2 E_2 + h_2\eta S E_1 - h_2\eta S Y_1 \tag{C.20}$$

$$Y_1 = \eta\left(E_2 - Y_2\right) \tag{C.21}$$

$$Y_2 = \eta\left(S E_1 - S Y_1\right), \tag{C.22}$$

where $\rho = \kappa_1/\kappa_2$ is the ratio of photon lifetimes, S is the time-shift operator defined by $SX(t) = X(t-2\tau)$, and $\tilde{f}_1$ and f_2 are defined for notational convenience as $\tilde{f}_1 = J_1 - 1 + i\omega$ and $f_2 = J_2 - 1 + i(\rho\omega + \delta)$.

Next, Y_1 and Y_2 are eliminated from eqs. (C.19)-(C.22). For that we solve eq. (C.20) for Y_2, and insert it into eq. (C.19). Furthermore, we shift eq. (C.19) by applying S to both sides and solve it for SY_1 and insert it into eq. (C.20). The resulting system reads

$$\epsilon d_t E_1 = \tilde{f}_1 E_1 + h_1\eta E_2 - \frac{h_1}{h_2}\eta(\rho\epsilon d_t E_2 - f_2 E_2) \tag{C.23}$$

$$\rho\epsilon d_t E_2 = f_2 E_2 + h_2\eta S E_1 - \frac{h_2}{h_1}\eta(\epsilon S d_t E_1 - S\tilde{f}_1 S E_1). \tag{C.24}$$

We expand the system (C.23)-(C.24) around the CW threshold and ignore the nonlinearities because they are straight forward to include in the derivation. This results in $\tilde{f}_1$ being replaced with $f_1 = J_1^{th} - 1 + i\omega$. Rewriting equations (C.23)-(C.24) then in matrix form yields

$$(A - \epsilon B d_t)E = 0 \tag{C.25}$$

with

$$A = \begin{pmatrix} f_1 & (\frac{h_1}{h_2}f_2 + h_1)\eta \\ ((\frac{h_2}{h_1}f_1 + h_2)\eta)S & f_2 \end{pmatrix} =: \begin{pmatrix} f_1 & g_1\eta \\ g_2\eta S & f_2 \end{pmatrix}, \tag{C.26}$$

$$B = \begin{pmatrix} 1 & \frac{h_1}{h_2}\eta\rho \\ \frac{h_2}{h_1}\eta S & \rho \end{pmatrix}, \tag{C.27}$$

$$E = \begin{pmatrix} E_1 \\ E_2 \end{pmatrix}. \tag{C.28}$$

Eq. (C.25) is the starting point of the multi-scale analysis. Rewriting the matrices in powers of ϵ, i. e.,

$$A = \sum_{i \geq 0} \epsilon^i A_i \tag{C.29}$$

$$B = \sum_{i \geq 0} \epsilon^i B_i \tag{C.30}$$

and further inserting in the multi-scale ansatzes (3.80)-(3.82) one obtains

$$\sum_{i,j \geq 0} \epsilon^{i+j} A_i E_j - \sum_{i,j,k \geq 0} \epsilon^{i+j+k+1} B_i \mathcal{T}_j E_k = 0. \tag{C.31}$$

Sorting eq. (C.31) according to powers of ϵ yields

$$\epsilon^i : \quad \sum_{\substack{j+k=i \\ j,k \geq 0}} \mathcal{S}_j E_k = 0 \tag{C.32}$$

with

$$\mathcal{S}_j = A_j - \sum_{\substack{k+l=j-1 \\ k,l \geq 0}} B_k \mathcal{T}_l. \tag{C.33}$$

After inserting the values of A_j, B_k one obtains

$$\mathcal{S}_0 = A_0 = \begin{pmatrix} f_1 & g_1 \\ g_2 S & f_2 \end{pmatrix}, \tag{C.34}$$

$$\mathcal{S}_i = \begin{pmatrix} -\mathcal{T}_{i-1} & -\frac{h_1}{h_2} \eta r \mathcal{T}_{i-1} \\ \left(g_2 \mathcal{L}_i - \frac{h_2}{h_1} \eta \sum\limits_{\substack{k+l=i-1 \\ k,l \geq 0}} \mathcal{L}_k \mathcal{T}_l \right) S & -r \mathcal{T}_{i-1} \end{pmatrix}, \quad i \geq 1. \tag{C.35}$$

Because the system is expanded close around the CW threshold, in the following $S = 1$ holds.

Slightly rewriting eq. (C.32) shows that the equation for the ith power of ϵ is a linear system with inhomogeneity for E_i

$$\epsilon^i : \quad \mathcal{S}_0 E_i = b_i, \tag{C.36}$$

$$b_i = - \sum_{\substack{j+k=i \\ j \geq 1,\, k \geq 0}} \mathcal{S}_j E_k. \tag{C.37}$$

We apply Fredholm's alternative to eq. (C.36) and start by determining the kernel of the adjoint of $\mathcal{S}_0$

$$A_0^\dagger w = 0 \tag{C.38}$$

$$\Longrightarrow w = \mu \begin{pmatrix} -\frac{g_2^\dagger}{f_1^\dagger} \\ 1 \end{pmatrix} = \begin{pmatrix} w_1^\dagger \\ 1 \end{pmatrix}. \tag{C.39}$$

The vector perpendicular to w is

$$u = \mu \begin{pmatrix} 1 \\ \frac{g_2^\dagger}{f_1^{\mathcal{L}\dagger}} \end{pmatrix} = \begin{pmatrix} 1 \\ -w_1^\dagger \end{pmatrix}. \tag{C.40}$$

Fredholm's alternative gives the solvability condition of eq. (C.36) as

$$w^\dagger b = 0. \tag{C.41}$$

The general solution is obtained by projecting onto u

$$u^\dagger \mathcal{S}_0 E_i = u^\dagger b_i. \tag{C.42}$$

Equation (C.42) allows relating the components $E_{1,i}$ and $E_{2,i}$ of E_i as

$$\implies E_{1,i} = (f_1 - g_2 w_1)^{-1} u^\dagger b_i - \frac{g_1}{f_1} E_{2,i}. \tag{C.43}$$

Because the calculations are involved, the next pages show Mathematica [165] code, which explicitly computes all the solvability conditions to third order, reconstructs the PDE and determines the linear PDE coefficients in agreement to section 5.4.

```
In[1]:=  (* This notebook computes the linear
           coefficients of the normal form PDE for the VCSEL-
          RSAM with the multi-scale analysis method. *)

In[2]:=  (* defining frequency Ω and Taylor
          expansion coefficients L, see section 3.3.1. *)

In[3]:=  Ω = 1 + ϵ * ω[1] + ϵ ^ 2 * ω[2] + ϵ ^ 3 * ω[3];

In[4]:=  dt = Ω * d[0] + ϵ ^ 2 * d[2] + ϵ ^ 3 * d[3];

In[5]:=  L1 = -ω[1] * d[0];
         L2 = -ω[2] * d[0] + ω[1] ^ 2 / 2 * d[0] ^ 2 - d[2];
         L3 = -ω[3] * d[0] - ω[1] ^ 3 / 6 * d[0] ^ 3 +
            ω[1] * ω[2] * d[0] ^ 2 + ω[1] * d[0] * d[2] - d[3];

In[8]:=  L = {1, L1, L2, L3};

In[9]:=  T = CoefficientList[dt, ϵ];

In[10]:= (* t[i] and l[i] are corresponding
           to equations (3.83) - (3.87). *)

In[11]:= t[i_] := T⟦i + 1⟧; l[i_] := L⟦i + 1⟧;

In[12]:= TimeScales = {d[0], d[2], d[3]};

In[13]:= (* Define the S matrix (C.34) - (C.35) *)

In[14]:= S[0] = {{f1, g1 * η}, {g2 * η, f2}};
         S[i_] :=
          {{-t[i - 1], -h1 / h2 * η * r * t[i - 1]}, {g2 * η * l[i] - h2 / h1 *
              η * Sum[l[i - 1 - j] * t[j], {j, 0, i - 1}], -r * t[i - 1]}}

In[16]:= (* Define the inhomogeneity b (C.37). *)

In[17]:= b[0] := {0, 0};
         b[i_ /; i > 0] := -Sum[S[j].e[i - j], {j, 1, i}];

In[19]:= wdagger = {w1, 1};

In[20]:= udagger = {1, -w1};

In[21]:= (* shorthand for the
          electrical field vector (E_1, E_2) *)

In[22]:= e[i_] := {el[i][1], el[i][2]};

In[23]:= (* Later, we substitute all occurences
          of E_2 with E_1 using equation (C.43). *)

In[24]:= ElSubstitution[imax_: Infinity] :=
           el[i_][1] /; i < imax :> ((f1 - η * g2 * w1) ^ (-1) *
                udagger.b[i] - η * g1 / f1 * el[i][2]);

In[25]:= (* Note that we replace η
           according to the CW threshold condition
           η^2 g1 g2 / (f1 f2) == 1. *)
```

```
In[26]:= VarSub = {f1 → J1 - 1 + ⅈ * ω,
                   f2 → J2 - 1 + ⅈ * (r * ω + δ) ,
                   g1 → (h1 / h2 * f2 + h1),
                   g2 → (h2 / h1 * f1 + h2),
                   w1 → -η * g2 / f1,
                   η → Sqrt[f1 * f2 / (g1 * g2)]};

In[27]:= SolvabilityCondition[i_] := Block[
            {fredholm, previousωs, fredholmByScale, containsω},
            previousωs = Catenate[ωSol /@ Range[1, i - 1]];
            (* Fredholm's alternative states that wdagger.b has
             to be zero in order for a solution to exist. *)
            fredholm = wdagger.b[i] //. ElSubstitution[i] //.
              previousωs ;
            (* We split the solvability condition
              by time scales... *)
            fredholmByScale = MonomialList[
              fredholm, TimeScales];
            (* ... and choose ω[i] in such a way
             that the maximum number of terms in
             front of the time scales vanish. *)
            containsω = MemberQ[Variables[#], ω[i]] & /@
              fredholmByScale;
            ωSol[i] = First@Solve[Thread[
                Pick[fredholmByScale, containsω] == 0], ω[i]];
            (* What remains is the solvability condition
             that relates d[i] with d[0]. *)
            Plus @@ Pick[fredholmByScale, Not /@ containsω] == 0 /.
             TimeScaleRelation[i - 1]];

In[28]:= ωSol[i_] := Module[{},
            SolvabilityCondition[i];
            ωSol[i]];

In[29]:= TimeScaleRelation[i_] := If[i < 2, {},
          First@Solve[SolvabilityCondition[i], d[i]] // Simplify]

In[30]:= ωSols = ωSol[1] ~ Join ~ ωSol[2] ~ Join ~ ωSol[3];

In[31]:= TimeScaleRelations =
          TimeScaleRelation[2] ~ Join ~ TimeScaleRelation[3];

In[32]:= PDEAllOrders = ((Ω - 1) * d[0] + ϵ^2 * d[2] + ϵ^3 * d[3] /.
              TimeScaleRelations /. ωSols);

In[33]:= (* This is the reconstructed PDE
          with consistent order approximation: *)

In[34]:= PDE =
          Coefficient[PDEAllOrders /. {d[0] → d[0] / ϵ}, ϵ, 0];

In[35]:= (* We split the PDE into derivatives of
          d[0] to obtain the diffusion coefficients. *)
```

```
In[36]:= PDEbyScales = CoefficientList[PDE, d[0]];

In[37]:= (* We are basically done now,
         what follows is cosmectics to display
          the coefficients in a human readable way. *)

In[38]:= (* We divide the coefficients by two to ensure
           the same scaling of the slow time for the multi-
          scale analysis and the mapping approach
           derivation (corresponds to scaling
              the time by either τ or 2τ). *)

In[39]:= CoefficientRaw[i_] := PDEbyScales[[i + 1]] / 2 //. VarSub;

In[40]:= CoefficientGain[i_] :=
          CoefficientRaw[i] /. r → 0 // Simplify

In[41]:= CoefficientAbsorber[i_] :=
           CoefficientRaw[i] - CoefficientGain[i] // Simplify;

In[42]:= CoefficientHumanReadable[i_] :=
           CoefficientGain[i] + CoefficientAbsorber[i];

In[43]:= CoefficientHumanReadable[1]
```

Out[43]=

$$\frac{h1}{2\left(-1+J1+\mathbb{i}\,\omega\right)\left(-1+h1+J1+\mathbb{i}\,\omega\right)}+\frac{h2\,r}{2\left(J2+\mathbb{i}\left(\mathbb{i}+\delta+r\,\omega\right)\right)\left(h2+J2+\mathbb{i}\left(\mathbb{i}+\delta+r\,\omega\right)\right)}$$

```
In[44]:= CoefficientHumanReadable[2]
```

Out[44]=

$$\frac{h1\left(-2+h1+2\,J1+2\,\mathbb{i}\,\omega\right)}{4\left(-1+J1+\mathbb{i}\,\omega\right)^{2}\left(-1+h1+J1+\mathbb{i}\,\omega\right)^{2}}+\frac{h2\,r^{2}\left(h2+2\,J2+2\,\mathbb{i}\left(\mathbb{i}+\delta+r\,\omega\right)\right)}{4\left(J2+\mathbb{i}\left(\mathbb{i}+\delta+r\,\omega\right)\right)^{2}\left(h2+J2+\mathbb{i}\left(\mathbb{i}+\delta+r\,\omega\right)\right)^{2}}$$

```
In[45]:= CoefficientHumanReadable[3]
```

Out[45]=

$$\frac{h1\left(h1^{2}+3\,h1\left(-1+J1+\mathbb{i}\,\omega\right)+3\left(-1+J1+\mathbb{i}\,\omega\right)^{2}\right)}{6\left(-1+J1+\mathbb{i}\,\omega\right)^{3}\left(-1+h1+J1+\mathbb{i}\,\omega\right)^{3}}+\frac{h2\,r^{3}\left(h2^{2}+3\,h2\left(J2+\mathbb{i}\left(\mathbb{i}+\delta+r\,\omega\right)\right)+3\left(J2+\mathbb{i}\left(\mathbb{i}+\delta+r\,\omega\right)\right)^{2}\right)}{6\left(J2+\mathbb{i}\left(\mathbb{i}+\delta+r\,\omega\right)\right)^{3}\left(h2+J2+\mathbb{i}\left(\mathbb{i}+\delta+r\,\omega\right)\right)^{3}}$$

```
In[46]:= (* As expected,
         the coefficients are equal to equations (5.79)-
          (5.81) obtained from the mapping approach. *)
```

BIBLIOGRAPHY

[1] O. Darrigol. *A history of optics from Greek antiquity to the nineteenth century*. Oxford University Press, 2012.

[2] J. Kepler. *Ad Vitellionem paralipomena quibus astronomiae pars optica traditur*. Claudium Marnium and Haeredes Ioannis Aubrii, 1604.

[3] A. E. Shapiro. "Newton's Optics." In: *The Oxford Handbook of the History of Physics*. Oxford University Press, 2013.

[4] A. Einstein. "Zur Quantentheorie der Strahlung." In: *Physikalische Zeitschrift* 18 (1917), pp. 121–128.

[5] A. Einstein. "Über einen die Erzeugung und Verwandlung des Lichtes betreffenden heuristischen Gesichtspunkt." In: *Annalen der Physik* 322 (1905), pp. 132–148.

[6] M. Planck. "Ueber das Gesetz der Energieverteilung im Normalspectrum." In: *Annalen der Physik* 309 (1901), pp. 553–563.

[7] A. L. Schawlow and C. H. Townes. "Infrared and optical masers." In: *Physical Review* 112 (1958), pp. 1940–1949.

[8] T. H. Maiman. "Stimulated optical radiation in ruby." In: *Nature* 187 (1960), pp. 493–494.

[9] A. Perot and C. Fabry. "On the application of interference phenomena to the solution of various problems of spectroscopy and metrology." In: *The Astrophysical Journal* 9 (1899), p. 87.

[10] J. Hecht. "A short history of laser development." In: *Applied Optics* 49 (2010), pp. 99–122.

[11] I. P. Kaminow, T. Li and A. E. Willner. *Optical fiber telecommunications VB: systems and networks*. Elsevier, 2010.

[12] A. Baranov and E. Tournié. *Semiconductor lasers: Fundamentals and applications*. Woodhead Publishing, 2013.

[13] C. Wandera et al. "Performance of high power fibre laser cutting of thick-section steel and mediumsection aluminium." PhD thesis. Lappeenranta University of Technology, 2010.

[14] U. Keller. "Recent developments in compact ultrafast lasers." In: *Nature* 424 (2003), pp. 831–838.

[15] O. Traxer and E. X. Keller. "Thulium fiber laser: the new player for kidney stone treatment? A comparison with Holmium: YAG laser." In: *World journal of urology* 38 (2020), pp. 1883–1894.

[16] H.-P. Berlien. *Applied laser medicine*. Springer Science & Business Media, 2003.

[17] V. S. Letokhov. "Laser biology and medicine." In: *Nature* 316 (1985), pp. 325–330.

[18] J. A. Parrish and B. C. Wilson. "Current and future trends in laser medicine." In: *Photochemistry and Photobiology* 53 (1991), pp. 731–738.

[19] D. F. Nelson and W. S. Boyle. "A continuously operating ruby optical maser." In: *Applied Optics* 1 (1962), pp. 99–101.

[20] H. Haken. "Analogy between higher instabilities in fluids and lasers." In: *Physics Letters A* 53 (1975), pp. 77–78.

[21] E. N. Lorenz. "Deterministic nonperiodic flow." In: *Journal of atmospheric sciences* 20 (1963), pp. 130–141.

[22] H. A. Haus. "Modelocking of semiconductor laser diodes." In: *Japanese Journal of Applied Physics* 20 (1981), pp. 1007–1020.

[23] H. A. Haus. "Mode-locking of lasers." In: *IEEE Journal of Selected Topics in Quantum Electronics* 6 (2000), pp. 1173–1185.

[24] E. Avrutin and J. Javaloyes. *Mode-Locked Semiconductor Lasers, Book Chapter In: Handbook of Optoelectronic Device Modeling and Simulation*. CRC press, Taylor and Francis, 2017, pp. 183–233.

[25] H. W. Mocker and R. J. Collins. "Mode competition and self-locking effects in a *Q*-switched Ruby laser." In: *Applied Physics Letters* 7 (1965), pp. 270–273.

[26] D. Lorenser, H. J. Unold, D. J. H. C. Maas, A. Aschwanden, R. Grange, R. Paschotta, D. Ebling, E. Gini and U. Keller. "Towards wafer-scale integration of high repetition rate passively mode-locked surface-emitting semiconductor lasers." In: *Appl. Phys. B* 79 (2004), pp. 927–932.

[27] U. Keller, K. J. Weingarten, F. X. Kärtner, D. Kopf, B. Braun, I. D. Jung, R. Fluck, C. Hönninger, N. Matuschek and J. Aus der Au. "Semiconductor saturable absorber mirrors (SESAM's) for femtosecond to nanosecond pulse generation in solid-state lasers." In: *IEEE Journal of Selected Topics in Quantum Electronics* 2 (1996), pp. 435–453.

[28] S. M. Link, D. J. H. C. Maas, D. Waldburger and U. Keller. "Dual-comb spectroscopy of water vapor with a free-running semiconductor disk laser." In: *Science* 356 (2017), pp. 1164–1168.

[29] T. Udem, R. Holzwarth and T. W. Hänsch. "Optical frequency metrology." In: *Nature* 416 (2002), pp. 233–237.

[30] H. A. Haus. "Theory of mode locking with a fast saturable absorber." In: *Journal of Applied Physics* 46 (1975), pp. 3049–3058.

[31] H. A. Haus. "Theory of mode locking with a slow saturable absorber." In: *IEEE Journal of Quantum Electronics* 11 (1975), pp. 736–746.

[32] C. Schelte. "Dynamics of Optical Localized Structures in Passively Mode-Locked Lasers." PhD thesis. Westfälische Wilhelms-Universität Münster and Universitat de les Illes Balears, 2021.

[33] C. Schelte, D. Hessel, J. Javaloyes and S. V. Gurevich. "Dispersive Instabilities in Passively Mode-Locked Integrated External-Cavity Surface-Emitting Lasers." In: *Physical Review Applied* 13 (2020), p. 054050.

[34] D. Hessel, S. V. Gurevich and J. Javaloyes. "Wiggling instabilities of temporal localized states in passively mode-locked vertical external-cavity surface-emitting lasers." In: *Optics Letters* 46 (2021), pp. 2557–2560.

[35] C. Schelte, P. Camelin, M. Marconi, A. Garnache, G. Huyet, G. Beaudoin, I. Sagnes, M. Giudici, J. Javaloyes and S. V. Gurevich. "Third Order Dispersion in Time-Delayed Systems." In: *Physical Review Letters* 123 (2019), p. 043902.

[36] D. J. H. C. Maas, A.-R. Bellancourt, B. Rudin, M. Golling, H. J. Unold, T. Südmeyer and U. Keller. "Vertical integration of ultrafast semiconductor lasers." In: *Applied Physics B* 88 (2007), pp. 493–497.

[37] B. Rudin, V. J. Wittwer, D. J. H. C. Maas, M. Hoffmann, O. D. Sieber, Y. Barbarin, M. Golling, T. Südmeyer and U. Keller. "High-power MIXSEL: an integrated ultrafast semiconductor laser with 6.4 W average power." In: *Optics Express* 18 (2010), pp. 27582–27588.

[38] A. Garnache, V. Lecocq, L. Ferrières, A. Benselama, M. Myara, L. Cerutti, I. Sagnes and S. Denet. "Industrial integration of high coherence tunable VECSEL in the NIR and MIR." In: *Proceedings of SPIE* 8966 (2014), pp. 163–172.

[39] M. Devautour, A. Michon, G. Beaudoin, I. Sagnes, L. Cerutti and A. Garnache. "Thermal Management for High-Power Single-Frequency Tunable Diode-Pumped VECSEL Emitting in the Near- and Mid-IR." In: *IEEE Journal of Selected Topics in Quantum Electronics* 19 (2013), p. 1701108.

[40] N. Takeuchi, N. Sugimoto, H. Baba and K. Sakurai. "Random modulation cw lidar." In: *Applied Optics* 22 (1983), pp. 1382–1386.

[41] N. Takeuchi, H. Baba, K. Sakurai and T. Ueno. "Diode-laser random-modulation cw lidar." In: *Applied Optics* 25 (1985), pp. 63–67.

[42] S. Hoogland, S. Dhanjal, A. C. Tropper, J. S. Roberts, R. Häring, R. Paschotta, F. Morier-Genoud and U. Keller. "Passively mode-locked diode-pumped surface-emitting semiconductor lasers." In: *IEEE Photonics Technology Letters* 12 (2000), pp. 1135–1137.

[43] R. Haring, R. Paschotta, E. Gini, F. Morier-Genoud, D. Martin, H. Melchior and U. Keller. "Picosecond surface-emitting semiconductor laser with > 200 mW average power." In: *Electronics Letters* 37 (2001), pp. 766–767.

[44] R. Häring, R. Paschotta, A. Aschwanden, E. Gini, F. Morier-Genoud and U. Keller. "High-power passively mode-locked semiconductor lasers." In: *IEEE Journal of Quantum Electronics* 38 (2002), pp. 1268–1275.

[45] B. Rudin, A. Rutz, M. Hoffmann, D. J. H. C. Maas, A.-R. Bellancourt, E. Gini, T. Südmeyer and U. Keller. "Highly efficient optically pumped vertical-emitting semiconductor laser with more than 20 W average output power in a fundamental transverse mode." In: *Optics Letters* 33 (2008), pp. 2719–2721.

[46] D. Waldburger, S. M. Link, M. Mangold, C. G. E. Alfieri, E. Gini, M. Golling, B. W. Tilma and U. Keller. "High-power 100 fs semiconductor disk lasers." In: *Optica* 3 (2016), pp. 844–852.

[47] J. M. Cushing. *Integrodifferential equations and delay models in population dynamics*. Springer Science & Business Media, 2013.

[48] G. Stoica. "A stochastic delay financial model." In: *Proceedings of the American Mathematical Society* 133 (2005), pp. 1837–1841.

[49] D. Hessel, S. V. Gurevich and O. Kamps. *Delaystabilisierung von Synchronisation mit Anwendung auf Stromnetzwerke*. Bachelor thesis. Westfälische Wilhelms-Universität Münster, 2017.

[50] K. Watanabe and M. Ito. "A process-model control for linear systems with delay." In: *IEEE Transactions on Automatic control* 26 (1981), pp. 1261–1269.

[51] D. Li and W. Ma. "Asymptotic properties of a HIV-1 infection model with time delay." In: *Journal of Mathematical Analysis and Applications* 335 (2007), pp. 683–691.

[52] R. Riaza. "DAEs in circuit modelling: a survey." In: *Surveys in Differential-Algebraic Equations I*. Springer, 2013, pp. 97–136.

[53] R. E. O'malley. *Singular perturbation methods for ordinary differential equations*. Vol. 89. Springer, 1991.

[54] D. J. Hill and I. M. Y. Mareels. "Stability theory for differential/algebraic systems with application to power systems." In: *IEEE transactions on circuits and systems* 37 (1990), pp. 1416–1423.

[55] A. Kumar and P. Daoutidis. *Control of nonlinear differential algebraic equation systems with applications to chemical processes*. Vol. 397. CRC Press, 1999.

[56] S. L. Campbell. "Nonregular 2D descriptor delay systems." In: *IMA Journal of Mathematical Control and Information* 12 (1995), pp. 57–67.

[57] N. H. Du, V. H. Linh, V. Mehrmann and D. D. Thuan. "Stability and robust stability of linear time-invariant delay differential-algebraic equations." In: *SIAM Journal on Matrix Analysis and Applications* 34 (2013), pp. 1631–1654.

[58] A. V. Egorov and W. Michiels. "A Connection Between Strangeness-Free Delay Differential-Algebraic and Neutral Type Systems." In: *IFAC-PapersOnLine* 50 (2017), pp. 1286–1291.

[59] P. Ha and V. Mehrmann. "Analysis and numerical solution of linear delay differential-algebraic equations." In: *BIT Numerical Mathematics* 56 (2016), pp. 633–657.

[60] U. M. Ascher and L. R. Petzold. "The numerical solution of delay-differential-algebraic equations of retarded and neutral type." In: *SIAM Journal on Numerical Analysis* 32 (1995), pp. 1635–1657.

[61] C. T. H. Baker, C. A. H. Paul and H. Tian. "Differential algebraic equations with after-effect." In: *Journal of computational and applied mathematics* 140 (2002), pp. 63–80.

[62] S. L. Campbell. "Singular linear systems of differential equations with delays." In: *Applicable analysis* 11 (1980), pp. 129–136.

[63] P. Ha. "On the Stability Analysis of Delay Differential-Algebraic Equations." In: *VNU Journal of Science: Mathematics - Physics* 34 (2018), pp. 52–64.

[64] W. Zhu and L. R. Petzold. "Asymptotic stability of linear delay differential-algebraic equations and numerical methods." In: *Applied Numerical Mathematics* 24 (1997), pp. 247–264.

[65] G. Giacomelli and A. Politi. "Relationship between Delayed and Spatially Extended Dynamical Systems." In: *Physical Review Letters* 76 (1996), pp. 2686–2689.

[66] S. A. Kashchenko. "The Ginzburg-Landau equation as a normal form for a second-order difference-differential equation with a large delay." English. In: *Computational Mathematics and Mathematical Physics* 38 (1998), pp. 443–451.

[67] G. Giacomelli, F. Marino, M. A. Zaks and S. Yanchuk. "Nucleation in bistable dynamical systems with long delay." In: *Physical Review E* 88 (2013), p. 062920.

[68] L. Larger, B. Penkovsky and Y. Maistrenko. "Virtual Chimera States for Delayed-Feedback Systems." In: *Physical Review Letters* 111 (2013), p. 054103.

[69] F. Marino, G. Giacomelli and S. Barland. "Front Pinning and Localized States Analogues in Long-Delayed Bistable Systems." In: *Physical Review Letters* 112 (2014), p. 103901.

[70] S. Yanchuk and G. Giacomelli. "Pattern Formation in Systems with Multiple Delayed Feedbacks." In: *Physical Review Letters* 112 (2014), p. 174103.

[71] T. Erneux, J. Javaloyes, M. Wolfrum and S. Yanchuk. "Introduction to Focus Issue: Time-delay dynamics." In: *Chaos: An Interdisciplinary Journal of Nonlinear Science* 27 (2017), p. 114201.

[72] S. Yanchuk and G. Giacomelli. "Spatio-temporal phenomena in complex systems with time delays." In: *Journal of Physics A: Mathematical and Theoretical* 50 (2017), p. 103001.

[73] J. Mulet and S. Balle. "Mode locking dynamics in electrically-driven vertical-external-cavity surface-emitting lasers." In: *IEEE Journal of Quantum Electronics* 41 (2005), pp. 1148–1156.

[74] D. A. W. Barton, S. Terrien, D. Hessel, S. V. Gurevich and J. Javaloyes. *DDE-BIFTOOL – Methods and parts of implementation for neutral DDEs and demo*. URL: `https://sourceforge.net/projects/ddebiftool/`. 2019.

[75] F. Gires and P. Tournois. "Interferometre utilisable pour la compression d'impulsions lumineuses modulees en frequence." In: *Comptes Rendus de l'Académie des Sciences Paris* (1964), pp. 6112–6115.

[76] W.-T. Zhu, H. Cui, A.-P. Luo, Z.-C. Luo and W.-C. Xu. "Wiggling and bending-free spatial solitons at the interface between photovoltaic photorefractive crystals with opposite diffusion effects." In: *Journal of the Optical Society of America B* 33 (2016), pp. 2209–2216.

[77] A. Suryanto and E. van Groesen. "On the swing effect of spatial inhomogeneous NLS solitons." In: *Journal of Nonlinear Optical Physics & Materials* 10 (2001), pp. 143–152.

[78] L. W. Dong and H. Wang. "Oscillatory behavior of spatial soliton in a gradient refractive index waveguide with nonlocal nonlinearity." In: *Applied Physics B* 84 (2006), pp. 465–469.

[79] D. Puzyrev, A. G. Vladimirov, S. V. Gurevich and S. Yanchuk. "Modulational instability and zigzagging of dissipative solitons induced by delayed feedback." In: *Physical Review A* 93 (2016), p. 041801.

[80] Y. V. Kartashov, L.-C. Crasovan, A. S. Zelenina, V. A. Vysloukh, A. Sanpera, M. Lewenstein and L. Torner. "Soliton eigenvalue control in optical lattices." In: *Physical Review Letters* 93 (2004), p. 143902.

[81] J. M. Soto-Crespo, N. Akhmediev and A. Ankiewicz. "Pulsating, Creeping, and Erupting Solitons in Dissipative Systems." In: *Physical Review Letters* 85 (2000), pp. 2937–2940.

[82] N. Akhmediev, J. M. Soto-Crespo and G. Town. "Pulsating solitons, chaotic solitons, period doubling, and pulse coexistence in mode-locked lasers: Complex Ginzburg-Landau equation approach." In: *Physical Review E* 63 (2001), p. 056602.

[83] W. Chang, A. Ankiewicz, N. Akhmediev and J. M. Soto-Crespo. "Creeping solitons in dissipative systems and their bifurcations." In: *Physical Review E* 76 (2007), p. 016607.

[84] K. Krupa, K. Nithyanandan, U. Andral, P. Tchofo-Dinda and P. Grelu. "Real-Time Observation of Internal Motion within Ultrafast Dissipative Optical Soliton Molecules." In: *Physical Review Letters* 118 (2017), p. 243901.

[85] F. Dohmen, J. Javaloyes and S. V. Gurevich. "Bound states of light bullets in passively mode-locked semiconductor lasers." In: *Chaos: An Interdisciplinary Journal of Nonlinear Science* 30 (2020), p. 063120.

[86] Y. Zhang, Y. Cui, L. Huang, L. Tong and X. Liu. "Full-field real-time characterization of creeping solitons dynamics in a mode-locked fiber laser." In: *Optics Letters* 45 (2020), pp. 6246–6249.

[87] M. Suzuki, T. Ohta, M. Mimura and H. Sakaguchi. "Breathing and wiggling motions in three-species laterally inhibitory systems." In: *Physical Review E* 52 (1995), pp. 3645–3655.

[88] L. Ophaus, J. Kirchner, S. V. Gurevich and U. Thiele. "Phase-field-crystal description of active crystallites: Elastic and inelastic collisions." In: *Chaos: An Interdisciplinary Journal of Nonlinear Science* 30 (2020), p. 123149.

[89] J. Guckenheimer and P. Holmes. *Nonlinear Oscillations, Dynamical Systems, and Bifurcations of Vector Fields*. Springer, 1983.

[90] G. Teschl. *Ordinary differential equations and dynamical systems*. Vol. 140. American Mathematical Society, 2012.

[91] A. Brown and C. Pearcy. *An introduction to analysis*. Vol. 154. Springer Science & Business Media, 1994.

[92] S. H. Strogatz. *Nonlinear Dynamics and Chaos: With Applications to Physics, Biology, Chemistry and Engineering*. Westview Press, 2000.

[93] G. Birkhoff and G.-C. Rota. *Ordinary differential equations*. John Wiley & Sons, 1978.

[94] J. C. Robinson. *An introduction to ordinary differential equations*. Cambridge University Press, 2004.

[95] G. Strang. *Introduction to linear algebra*. Vol. 3. Wellesley-Cambridge Press, 1993.

[96] J. H. Argyris, G. Faust, M. Haase and R. Friedrich. *An exploration of dynamical systems and chaos: completely revised and enlarged second edition*. Springer, 2015.

[97] F. Takens. "Detecting strange attractors in turbulence." In: *Dynamical systems and turbulence*. Springer, 1980, pp. 366–381.

[98] G. Sugihara and R. M. May. "Nonlinear forecasting as a way of distinguishing chaos from measurement error in time series." In: *Nature* 344 (1990), pp. 734–741.

[99] G. Sugihara, R. May, H. Ye, C.-h. Hsieh, E. Deyle, M. Fogarty and S. Munch. "Detecting causality in complex ecosystems." In: *Science* 338 (2012), pp. 496–500.

[100] C. Grebogi, E. Ott and J. A. Yorke. "Crises, sudden changes in chaotic attractors, and transient chaos." In: *Physica D: Nonlinear Phenomena* 7 (1983), pp. 181–200.

[101] M. Giglio, S. Musazzi and U. Perini. "Transition to chaotic behavior via a reproducible sequence of period-doubling bifurcations." In: *Physical Review Letters* 47 (1981), pp. 243–246.

[102] Y. Pomeau and P. Manneville. "Intermittent transition to turbulence in dissipative dynamical systems." In: *Communications in Mathematical Physics* (1980), pp. 189–197.

[103] J. A. Murdock. *Normal forms and unfoldings for local dynamical systems*. Springer, 2003.

[104] Y. A. Kuznetsov. *Elements of Applied Bifurcation Theory*. 2nd ed. Springer, 1998.

[105] R. Bellman. "On the computational solution of differential-difference equations." In: *Journal of Mathematical Analysis and Applications* 2 (1961), pp. 108–110.

[106] K. L. Cooke. "Differential—difference equations." In: *International symposium on nonlinear differential equations and nonlinear mechanics*. Elsevier. 1963, pp. 155–171.

[107] A. M. Krall. "On the real parts of zeros of exponential polynomials." In: *Bulletin of the American Mathematical Society* 70 (1964), pp. 291–292.

[108] C. E. Avellar and J. K. Hale. "On the zeros of exponential polynomials." In: *Journal of Mathematical Analysis and Applications* 73 (1980), pp. 434–452.

[109] S. Guo and J. Wu. *Bifurcation theory of functional differential equations*. Vol. 10. Springer, 2013.

[110] R. Bellman and K. L. Cooke. *Differential-Difference Equations*. Academic Press, 1963.

[111] M. Lichtner, M. Wolfrum and S. Yanchuk. “The spectrum of delay differential equations with large delay.” In: *SIAM Journal on Mathematical Analysis* 43 (2011), pp. 788–802.

[112] K. Shimoda. *Introduction to laser physics*. Vol. 44. Springer, 2013.

[113] C. B. Hitz, J. J. Ewing and J. Hecht. *Introduction to laser technology*. John Wiley & Sons, 2012.

[114] F. T. Arecchi and R. G. Harrison. *Instabilities and Chaos in Quantum Optics*. Vol. 34. Springer, 1987.

[115] R. P. Feynman, R. B. Leighton and M. Sands. *The Feynman Lectures on Physics, Vol. II: The New Millennium Edition: Mainly Electromagnetism and Matter*. Basic Books, 2011.

[116] A. E. Siegman. “Laser beams and resonators: The 1960s.” In: *IEEE Journal of Selected Topics in Quantum Electronics* 6 (2000), pp. 1380–1388.

[117] W. W. Chow, S. W. Koch and M. Sargent. *Semiconductor Laser Physics*. Springer, 1994.

[118] C. Henry. “Theory of the Linewidth of Semiconductor Lasers.” In: *IEEE Journal of Quantum Electronics* 18 (1982), pp. 259–264.

[119] C. Henry. “Theory of spontaneous emission noise in open resonators and its application to lasers and optical amplifiers.” In: *Journal of Lightwave Technology* 4 (1986), pp. 288–297.

[120] R. Lang and K. Kobayashi. “External optical feedback effects on semiconductor injection laser properties.” In: *IEEE Journal of Quantum Electronics* 16 (1980), pp. 347–355.

[121] J. Fontaine, W. Dietel and J.-C. Diels. “Chirp in a mode-locked ring dye laser.” In: *IEEE Journal of Quantum Electronics* 19 (1983), pp. 1467–1469.

[122] E. P. Ippen. “Principles of passive mode locking.” In: *Applied Physics B* 58 (1994), pp. 159–170.

[123] G. New. “Pulse evolution in mode-locked quasi-continuous lasers.” In: *IEEE Journal of Quantum Electronics* 10 (1974), pp. 115–124.

[124] A. G. Vladimirov, D. Rachinskii and M. Wolfrum. “Modeling of Passively Mode-Locked Semiconductor Lasers.” In: *Nonlinear Laser Dynamics: From Quantum Dots to Cryptography*. John Wiley & Sons, 2011, pp. 183–216.

[125] M. Marconi, J. Javaloyes, S. Balle and M. Giudici. “Hfow Lasing Localized Structures Evolve out of Passive Mode Locking.” In: *Physical Review Letters* 112 (2014), p. 223901.

[126] P. Camelin, C. Schelte, A. Verschelde, A. Garnache, G. Beaudoin, I. Sagnes, G. Huyet, J. Javaloyes, S. V. Gurevich and M. Giudici. "Temporal Localized Structures in mode-locked Vertical External-Cavity Surface-Emitting Lasers." In: *Optics Letters* 43 (2018), pp. 5367–5370.

[127] B. J. Leimkuhler, S. Reich and R. D. Skeel. "Integration methods for molecular dynamics." In: *Mathematical Approaches to biomolecular structure and dynamics*. Springer, 1996, pp. 161–185.

[128] G. M. Muslu and H. A. Erbay. "Higher-order split-step Fourier schemes for the generalized nonlinear Schrödinger equation." en. In: *Mathematics and Computers in Simulation* 67 (2005), pp. 581–595.

[129] J. A. C. Weideman and B. M. Herbst. "Split-Step Methods for the Solution of the Nonlinear Schrödinger Equation." In: *SIAM Journal on Numerical Analysis* 23 (1986), pp. 485–507.

[130] J.-M. Sanz-Serna and M.-P. Calvo. *Numerical Hamiltonian Problems*. CRC Press, 1994.

[131] J. C. Butcher. *Numerical methods for ordinary differential equations*. John Wiley & Sons, 2016.

[132] J. S. Hesthaven, S. Gottlieb and D. Gottlieb. *Spectral methods for time-dependent problems*. Vol. 21. Cambridge University Press, 2007.

[133] C. Schelte, J. Javaloyes and S. V. Gurevich. "Functional mapping for passively mode-locked semiconductor lasers." In: *Optics Letters* 43 (2018), pp. 2535–2538.

[134] The MathWorks Inc. *MATLAB, Version 9.12.0 (R2022a)*. 2022.

[135] K. Engelborghs, T. Luzyanina and D. Roose. "Numerical Bifurcation Analysis of Delay Differential Equations Using DDE-BIFTOOL." In: *ACM Transactions on Mathematical Software* 28 (2002), pp. 1–21.

[136] J. Sieber, K. Engelborghs, T. Luzyanina, G. Samaey and D. Roose. *DDE-BIFTOOL Manual - Bifurcation analysis of delay differential equations*. arXiv. 2014.

[137] E. Süli and D. F. Mayers. *An Introduction to Numerical Analysis*. Cambridge University Press, 2003.

[138] C. T. Kelley. *Solving nonlinear equations with Newton's method*. Society for Industrial and Applied Mathematics, 1987.

[139] T. J. Ypma. "Historical Development of the Newton–Raphson Method." In: *SIAM Review* 37 (1995), pp. 531–551.

[140] D. Breda, S. Maset and R. Vermiglio. "Pseudospectral approximation of eigenvalues of derivative operators with non-local boundary conditions." In: *Applied Numerical Mathematics* 56 (2006), pp. 318–331.

[141] W. Michiels. "Spectrum-based stability analysis and stabilisation of systems described by delay differential algebraic equations." In: *IET Control Theory & Applications* 5 (2011), pp. 1829–1842.

[142] U. Thiele. *Lecture "Introduction to Numerical Continuation"*. Zenodo. 2021.

[143] D. A. W. Barton, B. Krauskopf and R. E. Wilson. "Collocation schemes for periodic solutions of neutral delay differential equations." In: *Journal of Difference Equations and Applications* 12 (2006), pp. 1087–1101.

[144] J. Sieber. *Extended Systems for bifurcations of periodic orbits in delay differential equations*. Figshare. 2013.

[145] A. H. Nayfeh. *The method of normal forms*. Wiley-VCH, 2011.

[146] I. Fredholm. "Sur une classe d'équations fonctionnelles." In: *Acta Mathematica* 27 (1903), pp. 365–390.

[147] A. G. Ramm. "A simple proof of the Fredholm alternative and a characterization of the Fredholm operators." In: *The American Mathematical Monthly* 108 (2001), pp. 855–860.

[148] A. G. Vladimirov and D. Turaev. "Model for passive mode locking in semiconductor lasers." In: *Physical Review A* 72 (2005), p. 033808.

[149] C. Schelte, J. Javaloyes and S. V. Gurevich. "Dynamics of temporally localized states in passively mode-locked semiconductor lasers." In: *Physical Review A* 97 (2018), p. 053820.

[150] T. Kolokolnikov, M. Nizette, T. Erneux, N. Joly and S. Bielawski. "The *Q*-switching instability in passively mode-locked lasers." In: *Physica D: Nonlinear Phenomena* 219 (2006), pp. 13–21.

[151] H. Uecker, D. Wetzel and J. D. M. Rademacher. "pde2path - A Matlab Package for Continuation and Bifurcation in 2D Elliptic Systems." In: *Numerical Mathematics: Theory, Methods and Applications* 7 (2014), pp. 58–106.

[152] D. Hessel, S. V. Gurevich and J. Javaloyes. "Super mode-locking in passively mode-locked vertical external-cavity surface-emitting lasers." *(in preparation)*.

[153] M. Marconi, J. Javaloyes, S. Balle and M. Giudici. "Passive Mode-Locking and Tilted Waves in Broad-Area Vertical-Cavity Surface-Emitting Lasers." In: *IEEE Journal of Selected Topics in Quantum Electronics* 21 (2015), pp. 85–93.

[154] P. M. Stolarz, J. Javaloyes, G. Mezosi, L. Hou, C. N. Ironside, M. Sorel, A. C. Bryce and S. Balle. "Spectral dynamical behavior in passively mode-locked semiconductor lasers." In: *IEEE Photonics Journal* 3 (2011), pp. 1067–1082.

[155] M. J. Ablowitz. *Nonlinear Dispersive Waves: Asymptotic Analysis and Solitons*. Cambridge University Press, 2011.

[156] T. G. Seidel, J. Javaloyes and S. V. Gurevich. "Influence of time-delayed feedback on the dynamics of temporal localized structures in passively mode-locked semiconductor lasers." In: *Chaos: An Interdisciplinary Journal of Nonlinear Science* 32 (2022), p. 033102.

[157] A. Bartolo, T. G. Seidel, N. Vigne, A. Garnache, G. Beaudoin, I. Sagnes, M. Giudici, J. Javaloyes, S. V. Gurevich and M. Marconi. "Manipulation of temporal localized structures in a vertical external-cavity surface-emitting laser with optical feedback." In: *Optics Letters* 46 (2021), pp. 1109–1112.

[158] J. Sieber. Personal communication. 2019.

[159] S. Yanchuk, S. Ruschel, J. Sieber and M. Wolfrum. "Temporal Dissipative Solitons in Time-Delay Feedback Systems." In: *Physical Review Letters* 123 (2019), p. 053901.

[160] T. Malica et al. "Mapping the dynamical regimes of a SESAM mode-locked VECSEL with a long cavity using time series analysis." In: *Optics Express* 26 (2018), pp. 16624–16638.

[161] J. P. Hausen, S. Meinecke, B. Lingnau and K. Lüdge. "Pulse Cluster Dynamics in Passively Mode-Locked Semiconductor Vertical-External-Cavity Surface-Emitting Lasers." In: *Physical Review Applied* 11 (2019), p. 044055.

[162] J. P. Hausen. "Pulse pattern formation in V-shaped external cavity mode-locked lasers: Modelling strategies and bifurcation analysis." PhD thesis. Technische Universität Berlin, 2021.

[163] T. G. Seidel, J. Javaloyes and S. V. Gurevich. "Normal form for frequency comb and localized states in time-delayed Kerr–Gires–Tournois interferometers." In: *Optics Letters* 47 (2022), pp. 2979–2982.

[164] A. Bartolo et al. "Temporal localized Turing patterns in mode-locked semiconductor lasers." In: *Optica* 9 (2022), pp. 1386–1393.

[165] Wolfram Research Inc. *Mathematica, Version 13.1*. 2022.

Success is not how far you got
but the distance you traveled
from where you started.